



UNIVERSITÀ
degli STUDI
di CATANIA

Department of Chemical Sciences
International PhD in Chemical Sciences
XXXII Cycle

Massimiliano Gaeta

**Porphyrin-based nanostructures via self-
assembly: non-covalent and covalent approach**

PhD Thesis

Tutor: Prof. Roberto Purrello

PhD Coordinator: Prof. Salvatore Sortino

academic cycle 2016-2019

Doctor of Philosophy Thesis
International PhD in Chemical Sciences, XXXII Cycle, 2016-2019
Porphyrin-based nanostructures via self-assembly: non-covalent and covalent approach
MASSIMILIANO GAETA

© MASSIMILIANO GAETA, 2019
UNIVERSITY OF CATANIA, ITALY, 2019

Department of Chemical Sciences,
Viale Andrea Doria, 6,
95125, Catania (CT) - Italy
Tel. +39 095 7385125
www.dsc.unict.it

Archived on Open Access Institutional Archive of University of Catania using
DSpace open source repository application <http://dspace.unict.it/>

Reviewed and approved by:

Prof. Örjan Hansson (mid-term thesis review)
University of Gothenburg (Sweden), Department of Chemistry and Molecular
Biology
orjan.hansson@chem.gu.se

Prof. Luigi Monsù Scolaro
University of Messina (Italy), Department of Chemical, Biological,
Pharmaceutical and Environmental Sciences
luigi.monsuscolaro@unime.it

Prof. Roberto Paolesse
University of Rome Tor Vergata (Italy), Department of Chemical Science and
Technologies
roberto.paolesse@uniroma2.it

page left blank intentionally

*“Theory is when you know everything but nothing works.
Practice is when everything works but no one knows why.
In our lab, theory and practice are combined:
nothing works and no one knows why”*

Albert Einstein

Table of Contents

Abstract	iv
1. Introduction.....	1
1.1 Aim of this thesis.....	5
2. SECTION I: non-covalent approach	
2.1 Supramolecular chemistry	8
2.2 Porphyrins.....	13
2.3 Porphyrin self-assembly	20
3. Porphyrin aggregation modulated by polypeptides	
3.1 State-of-the-art.....	29
3.2 Results and Discussions	39
3.3 Final remarks.....	56
4. Supramolecular porphyrin-calix[4]arene complexes	
4.1 State-of-the-art.....	57
4.2 Results and Discussions	71
4.2.1 Towards porphyrin/calix 1D assemblies:	
H ₂ DPPS3/BC ₄ and CuDPPS3/chiral-BC ₄ -NH ₂ complexes	71
H ₂ DPPS2/BC ₄ complexes	86

4.2.2 Towards porphyrin/calix 2D assemblies:	
CuTPPS4/bis-calix[4]tube complexes	92
4.2.3 Towards long distance chiral transfer in	
porphyrin/calix[4]arene 2D assemblies	102
4.2.4 Towards porphyrin/calix 2D-3D assemblies:	
CuTPPS4/tris-calix[4]arene complexes	108
4.3 Final remarks.....	118
5. SECTION II: covalent approach	
5.1 Covalent organic framework, Metal-organic framework	
and Supramolecular framework.....	122
5.2 State-of-the-art.....	124
5.3 Results and Discussions	136
5.4 Final remarks.....	148
6. Conclusions and Perspectives	149
References	151
Appendix	166
Instrumental techniques' overview	
Uv-Vis spectroscopy	166
Fluorescence spectroscopy.....	170
Resonance light scattering spectroscopy.....	174
Circular dichroism spectroscopy.....	176
Infrared spectroscopy	179

Nuclear magnetic resonance spectroscopy	182
Mass spectrometry	184
BET surface analysis.....	185
X-ray diffraction	189
Scanning electron microscopy	192
Curriculum Vitae.....	194
List of Publications and Proceedings.....	196
Acknowledgments.....	202

Abstract

The possibility to manipulate matter at the nanometric scale has been shaping our life thanks to increasing level of nanotechnological devices.

In perspective to overcome the physical limitations correlated to top-down nanofabrication methods, self-assembly appears as powerful and attractive strategy for constructing complex nanostructures by spontaneous organization of appropriate building blocks. Self-assembly implies the existence of a molecular recognition which, in principle, allows a structure to build itself from small disorder units in a more ordered pattern.

Although self-assembly typically suggests the use of non-covalent forces, it is worth considering that two or more monomers can also self-assemble through covalent linkage. This is the case of polymerization process, in which a covalent self-assembly arises from reactive monomers in order to create extensive framework. Herein, the studies discussed attempt to exploit this two-fold approach, non-covalent/covalent self-assembly, to realize intriguing nanostructures.

To self-organize molecular building blocks into well-organized structures is strictly needed to control their size, dimensionality and properties. Therefore, a first step is to choose building blocks useful to our goals. In this respect, porphyrins and related derivatives represent ideal macrocycles to construct functional materials. In fact, non-covalent porphyrin self-assembly permits to obtain large aggregates in aqueous media. However, the phenomenon is often ungovernable for practical applications.

Several strategies have been implemented to this aim, among them, the template-assisted self-assembly. As such, this latter strategy has been successfully employed in the present thesis work.

Firstly, in chapter 3 we have demonstrated the possibility of controlling in water the H₂TPPS₄ J-aggregation, after demetallation/protonation of its zinc(II) derivative, ZnTPPS₄, at acidic conditions and in presence of poly-L-lysine, PLL, as template. By varying the polylysine degree of polymerization, we can modulate the final aggregation. Complete spectroscopic studies confirm as follows: *i*) if short PLLs are used, the fast demetallation/protonation of ZnTPPS₄ drives the rapid formation of several families of less organized J-agg, made up of few monomers; *ii*) longer PLLs promote structural reorganizations of the protonated porphyrins leading to the formation of long ordered J-agg, resulting as well, in a chirality enhancement.

Furthermore, a template strategy based on host-guest chemistry is also reported. In particular, calixarenes have been employed in interactions with porphyrin to achieve supramolecular complexes.

In chapter 4, spectroscopic measurements prove that calixarenes are able to control the stoichiometry of the self-assembly process hierarchically. Moreover, we can modulate the dimensionality of the supramolecular porphyrin-calixarene complexes (1D, 2D or 3D) depending on geometric parameters. For instance, di-topic calixarenes drive towards the building of 1D and 2D structures, also conveying chirality if an asymmetric calixarene is used. On the contrary, tri-topic calixarenes leads to 3D complexes.

As above-mentioned, covalent self-assembly is another strategy explored in this dissertation. In order to acquire some skills in covalent approach, I focused on synthesis and characterization of Covalent Organic Frameworks, COFs.

COFs are an emerging class of porous material, based on covalent self-assembly. A particular solid COF, namely RT-COF-1 was synthesized,

characterized ads also tested in terms of adsorption of dye pollutants from water. Nevertheless, the study has provided the basic concepts about covalent synthesis in order to increase the knowledge in that matter.

A deep comprehension of the phenomena underlying the non-covalent and covalent approach paves the way to develop a combined strategy. In perspective, this mixed-approach may lead to generate complex nanostructures both in liquid and solid state, with control of dimensionality, crystallinity and features for technological applications.

1.

Introduction

The astonishing recent progress in nanotechnology is due largely to the capability to explore, synthesize, and exploit materials at nanometer level. However, although the terms “*nanotechnology*” and “*nanomaterials*” may seem to be common sense and diffusely used in our modern society, a clear interpretation is not yet given. The most appropriate definition affirms that *nanotechnology* refers to structures roughly in the 1–100 nm size regime, in at least one dimension.^[1] Nevertheless, from a fundamental point of view, the nanostructures are fascinating because their optical and optoelectronic properties, are often quite different from those of single molecules or bulk materials.^[1,2] On the other hand, the strict size control in *nanotechnology* is a fundamental step towards the building of nanomaterials with defined features. In fact, modern electronic devices have been made available thanks to the striking development about the size reduction of their components.

Generally, the methods for realizing a *nanostructure* are divided into two major categories: i) “*top–down*” and ii) “*bottom–up*” strategies, depending on the processes involved in creating nanodevices.^[3] A *top–down* approach corresponds to create functional nanoscaled materials from larger dimensions and reducing them to the required values. On the contrary, *bottom–up* approaches seek to have molecular or atomic components built up into more complex nanoscale assemblies or directed self-assemblies. This area uses atoms or small molecules as *building blocks* of multi-level structures and is extremely promising since it could lead to no waste or unused materials.^[3]

In this respect, over the last decades an intriguing aspect in *Material Science* is the construction of nanostructures from small building blocks by means of self-assembly process.^[4,5] As such, the synthesis of *molecular building block* is well-developed and the preparation of nanostructures could derive from multiple *weak-non-covalent* interactions (*i.e.* electrostatic and van der Waals forces, solvophobic effects, hydrogen bonding, π - π stacking and metal coordination). Moreover, the use of above-mentioned interactions and of their opportune reversibility allows for a “*self-error-correcting*” process leading to the formation of the thermodynamically stable species.^[6] This strategy, commonly known as **non-covalent synthesis**, sinks its roots into the chemistry beyond the molecules, so-called *Supramolecular Chemistry*.^[7,8]

On this point, porphyrins represent ideal molecular building blocks for the formulation of functional supramolecular materials. They have topological diversity, minimal conformational flexibility, and can be readily functionalized at different sites. Even, they are stable under a variety of conditions, exhibit robust optical and redox properties, and can be readily fine-tuned to self-assemble and self-organize in predefined architectures.^[9,10] The programmed porphyrin self-assembly into 2D networks and 3D frameworks leads to obtain nanoporous solids with pore sizes between 0.2 nm and 2 nm.^[11,12] As a consequence, porphyrin-based nanostructures may be employed in a variety of emerging areas, such molecular sorption, sensing, photonics, catalysis, and nanoscale reaction chambers.^[11–13]

Nevertheless, the variation in the size and the morphologies significantly influences the porphyrin-based assemblies’ properties, hence the *non-covalent template approach* (e.g. by means of polymeric matrices or calixarene) is a valid method to govern the spontaneous assembly.^[14–20] Unfortunately, the weak and reversible nature of interactions utilized to hold the building blocks in

nanostructures, are often not robust enough to be useful for industrial applications.^[21]

Alternatively, another strategy for the self-assembly process is the employment of irreversible covalent bonds in order to generate arrays of covalently linked atoms with well-defined composition, connectivity and shape. This latter approach, namely here **covalent synthesis**, sets the stage in a typical molecular recognition, in which appropriate monomers' organic moieties react together to produce a final nanostructure. For sake of simplicity, the covalent polymerization is the most important example for preparing molecules with high molecular weights. In detail, a relatively simple, reactive low molecular weight substances (monomers) is caused to react with themselves in a process that produces a molecule (a polymer) comprising many covalently connected monomers.^[22]

Covalent Organic Frameworks (COFs), Metal-Organic Frameworks (MOFs) and Supramolecular Organic Frameworks (SOFs), based on porphyrin or not, fall within that field. They are an emerging class of porous polymers based on condensation reactions of organic and metal-organic monomers which have been receiving a great attention in the international scientific community.^[23] The connection through strong covalent bonds permits an ordered two- or three-dimensional porous nanostructure.^[24] As such, their high surface area allows for adsorption properties and also storage, catalysis and sensing applications. Furthermore, the choice of appropriate monomers paves the way towards new advanced materials.^[24–27] However, this covalent approach often requires a laborious multistep process, as well as enormous efforts when applied to large and complex nanomaterials.^[1,6]

For this reason, a *mixed*-approach, in which the concept of Supramolecular Chemistry meets the “covalent approach”, is highly desirable (**Fig.1**). In fact, in order to realize complex porphyrin-based nanostructures, full understanding of

both strategies is essential to minimize the covalent disadvantages, increasing the non-covalent advantages. In **Fig.1** is reported a schematic comparison between the three different approaches:

Route A- the starting molecular building blocks are able to interact with a template by means of supramolecular forces to originate a non-covalent nanostructure. However, this structure owns low complexity and may collapse under different experimental conditions;

Route B- the building blocks react covalently with each other to form a covalent structure via external input (e.g. temperature). Here, although the complexity and stability are enhanced remarkably, the degree of structural organization may not be satisfying;

Route C- finally, the combined approach. Firstly, the molecular building blocks interact with the supramolecular template to generate a precursor-structure. Afterwards, the covalent reactions take part in the precursor-system in order to realize the final nanostructure. Compared to other ones, this structure might own a large stability and an extraordinary internal order, resulting in a more structural organization.

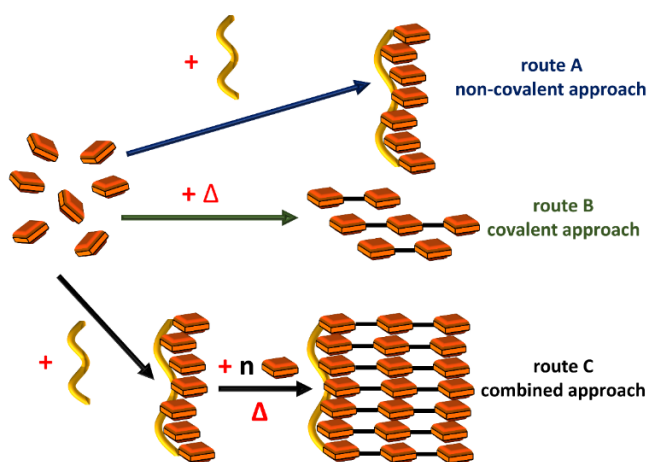


Fig.1 Illustration of the three different strategy: non-covalent, covalent and combined approach. The details are discussed in the text.

1.1

Aim of this thesis

A *mixed*-approach to realize porphyrin-based nanostructures requires a deep comprehension regarding the covalent and non-covalent aspects underlying the nanostructures' synthesis. As a consequence, the aim of this thesis is to investigate and explain the combined strategy through the following two-fold strategy, highlighting strengths and limits: *i*) supramolecular synthesis based on porphyrin nanostructures, and *ii*) covalent synthesis based on polymerization of covalent frameworks.

For the first strategy, I performed most of my doctoral work at Università degli Studi di Catania (Italy), in the laboratory “*Laboratorio di Spettroscopia dei Sistemi Complessi*” (LSSC) under the supervision of Professor Roberto Purrello, specialised in supramolecular aggregation of porphyrin systems. Here, my doctoral research was addressed to achieve some one-, two- and three-dimensional porphyrin-based nanostructures by using a supramolecular template to control the final aggregation. The entire *Section I*, including *Chapters 3* and *4* of this thesis concern such arguments.

In particular, I explored the role played by polyelectrolytes (e.g. polylysine) to promote the aggregation of porphyrins through electrostatic self-assembly, assisted by dispersive forces, in aqueous solution (*Chapter 3*). We succeeded in understanding how the polylysine chain length affects the formation, kinetics, and chirality of J-aggregates formed after ZnTPPS4 demetallation at $\text{pH} < 1.5$.^[28,29]

In another step, I examined the importance of calix[4]arene templates to govern the porphyrin self-aggregation (*Chapter 4*). We achieved novel one-, two-

and three-dimensional complexes by using the host-guest interactions between cationic bis-calix[4]arenes and synthetic anionic sulfonate-porphyrins. Furthermore, we demonstrate the possibility to control another significant property, the *Chirality*. These findings support our hypothesis about the presence of an *electronic communication* between the porphyrin building blocks into the supramolecular complexes.

For the second strategy, I moved to Universidad Autónoma de Madrid as visiting PhD student under the supervision of Prof. Félix Zamora - expert in covalent self-assembly – for a one-semester research period. The *Section II* and *Chapter 5* treat this subject.

In the Zamora's research group, I acquired skills about synthesis and characterization of Covalent Organic Frameworks (COFs). There, I learned the needed steps to synthesize the covalent *RT-COF-1* starting from suitable monomers.^[30,31] Then, we characterized the polymer and we also tested its performance in terms of adsorption of dye pollutants from water. Nevertheless, in Madrid, I examined in depth the basic concepts of the covalent synthesis in order to increase my knowledge in that matter.

For the sake of readability and clarity, I have preferred to organize this thesis in two sections, one for each strategy. In the following *Section I*, I will discuss about Supramolecular Chemistry, molecular building blocks, their non-covalent self-assembly and my research activity at Università degli Studi di Catania. Instead in the *Section II*, I will illustrate the covalent approach based on COFs and the research work conducted at Universidad Autónoma de Madrid.

2. SECTION I: non-covalent approach

2.1

Supramolecular Chemistry

The term *supramolecular* is a widespread word employed since late 1960s to describe complex biological structures, although early examples of supramolecular systems were illustrated at the beginning of 19th century by Sir Humphry Davy owing to the discovery of chlorine clathrate hydrate, that is the inclusion of chlorine within a solid water lattice.^[32-34] The modern point of view of *Supramolecular Chemistry* dates back to Lehn's Nobel Prize lecture in 1987 where it was defined as "chemistry beyond the molecule".^[8] Since then the keyword "Supramolecular Chemistry" has grown exponentially in literature including, as well, *host-guest chemistry* or *molecular recognition*. The latter two put their roots down in the "lock and key" mechanism of biological catalysis proposed by Emil Fischer in 1894.^[35-37]

However, the description given by J.M. Lehn during his Nobel Prize Lecture is relatively incomplete; in fact, many reactions as polypropylene synthesis or solidification of cement can be defined as "chemistry beyond the molecule". Likely, a more accurate definition was due to J.M. Lehn himself in 1990, describing the Supramolecular Chemistry as "*the designed chemistry of intermolecular bond*".^[38] This has involved a change in the mindset of chemists, from single molecules often constructed step-by-step via direct covalent linkages, towards large molecular assemblies with their usual non-covalent weak intermolecular bonds (**Fig.2**). These intermolecular bonds include electrostatic interactions, hydrogen bonding, π - π interactions, Van der Waals forces and hydrophobic or solvophobic effects.^[7,39,40]

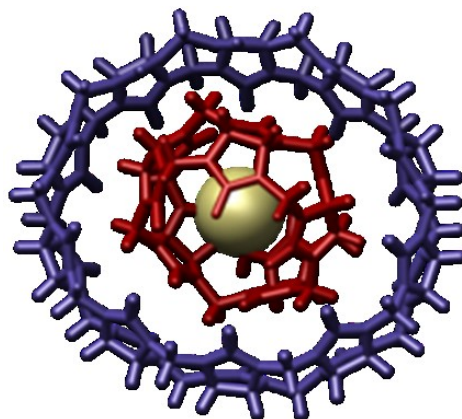


Fig.2 Example of a supramolecular assembly. Reproduced from ref. ^[41]

Nowadays, we consider the Supramolecular Chemistry as interdisciplinary field of research. Supramolecular chemistry is a multidisciplinary field which engages different areas, from the traditional organic and inorganic chemistry, essential to synthesise the precursors for a supermolecule, to physical chemistry and computational chemistry, needed to understand the properties and the behaviour of complex supramolecular systems.^[42] The basis of Supramolecular Chemistry start from the observation of *Nature* and related phenomena, such as protein folding processes or molecular recognition between enzyme and substrate are relevant examples. In addition, an high degree of technical knowledge is required in order to apply supramolecular systems to the real world, such as the development of nanotechnological devices.^[40,43–46] The promise of useful molecular devices remains a motivation for the continuing widespread interest in this field.

In principle, the *Supramolecular Chemistry* refers to two wide groups: i) *host-guest chemistry* and ii) *self-assembly*. The main difference between these two categories can be described in terms of size and shape.^[39,40]

If one molecule is expected larger than another and can enclose around it then it is labelled as “*host*” and the smaller molecule is its “*guest*”. which becomes entrapped by the host (**Fig.3**).^[40]

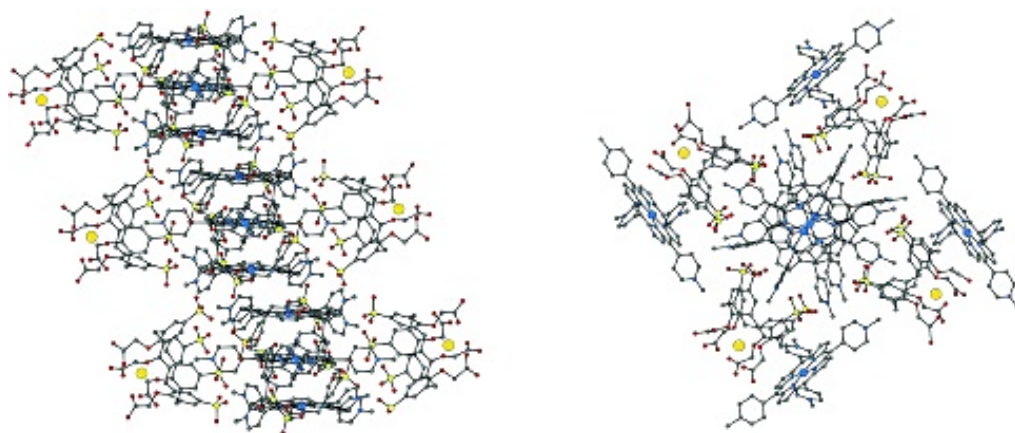


Fig.3 Some examples of supramolecular host-guest complexes between calix[4]arenes (hosts) and porphyrins (guests). Reproduced from ref.^[47]

On the contrary, whether there are no species is acting as a host for another, more species may form supramolecular assemblies spontaneously, in a process termed *self-assembly*.^[40] Strictly, self-assembly is an equilibrium between two or more molecular components to produce an aggregate with a structure that is dependent only on the information contained within the chemical building blocks.^[43] Noteworthy, self-assembly is usually a spontaneous process but could be influenced by solvents or the presence of template (e.g. small molecules, aminoacids, polymers, polyelectrolytes, polypeptides, DNA, etc.).^[40] In both cases, host-guest interactions and template self-assembly, some concepts such as *complementarity*,^[39,40,42,48] *pre-organization*^[38,40,48] and *co-operativity*^[40,49–51] of the binding sites play a key role in the deep comprehension of the supramolecular phenomena.

In other words, when an host (or a template) discloses a preference for a particular guest (or family of guests), is said to show *selectivity* towards its

guest.^[40] As such, the selectivity depends on several factors, first of all, the complementary. *Complementarity* plays an important role in biological and supramolecular systems, for example, in the function of enzymes, described for the first time by above-mentioned Emil Fisher in 1984 through the “key and lock” model.^[36] A supramolecular interaction shows *complementary* when both the host and guest own mutual spatially and electronically complementary binding sites to form a supermolecule.^[39]

The idea of *pre-organisation*, first proposed by Cram,^[52] implies that if the binding sites of a host molecule are arranged more similar for binding to a guest, minimal changes in the degrees of conformational freedom of the host are expected. As a consequence, the entropic costs - in terms a loss of degrees of freedom – are minimized, thus, making favourable the overall free energy of the host-guest complex formation.^[39,40,52]

Moreover, another remarkable aspect which can reduce the entropic costs is the *co-operativity*. Indeed, if two or more binding sites - acting in a concerted fashion - produce an interaction stronger than when the binding sites act independently, we refer to co-operativity effects.^[40,50,53,54] For example, we observe a *positive co-operativity*^[40,54] when the presence of the first species increases the receptor’s affinity for the second species and arises in various biological processes and contributes to explain the allosteric effect in enzymes.^[50] Instead, *negative co-operativity* is the reverse of positive co-operativity and there are only few examples in Nature.^[40]

Furthermore, a supramolecular synthesis follows rigid hierarchical rules. Hierarchy is a kinetic time-dependent process in which the self-organization of simple elements, following a *specific sequence* of complexation events, leads to multi-part supramolecular architectures.^[55–57] This phenomenon is also called *sergeant-soldier principle*,^[56,58–62] in other words: the sequence of the individual

molecular components in the final product derives from the sequence of chemical events (e.g. addition order of each molecular species).

The non-covalent synthesis contrasts with the covalent approach, in which covalent bonds play a key role in the creation of new molecular structures. Although in some cases the covalent approach allows to reach an high degree of complexity in the formation of organized structures compared to the non-covalent one, the non-covalent approach takes advantages of green reagents, minimal energy costs and reduce waste. The principles and phenomena described within this chapter are the basic concepts upon which supramolecular chemistry is based; a union of these phenomena can lead to intricate and complex systems.

As a consequence, the choice of suitable molecular building blocks is an essential part to obtain predefined self-assembled supramolecular architectures.^[5,40,63] As illustrated, the supramolecular synthons should be as complementary as possible - in terms of size, shape and chemical properties (charge, hardness, acidity, etc.) - to maximize the interactions in order to facilitate the building of the desired supramolecular complexes.

Due to different degree of pre-organization and synthetic versatility, large cyclic molecules or macrocycles represent important groups of compounds employed in supramolecular chemistry.^[39,43,64] Porphyrins, phthalocyanines and calix[n]arenes are just some examples of molecular building blocks. In the next chapters, porphyrins as molecular building blocks in self-assembled systems will be discussed.

2.2

Porphyrins

The term *Porphyrin* derives from Greek word *πορφύρα* (porphura, meaning purple) and comprises an interesting class of macrocycle rings involved in a wide variety of biological processes ranging from oxygen transport to photosynthesis and catalysis.^[65,66] In Nature, *chlorophylls* and *hemes* constitute important examples.^[65,67] The former play pivotal roles in photosynthesis as both light harvesting antennae and charge separation reaction systems.^[68] The latter are one of the key components for biocatalysts and oxygen carriers in the blood.^[68] It is not an hyperbole to assert that no life can exists on Earth without porphyrins.

In chemical terms, porphyrins consists of four pyrrole subunits linked via methine bridges at the pyrroles' α carbon atoms, as illustrated in **Fig.4**. According to *Huckel's rule*,^[69] this macrocycle is a planar and aromatic ring containing 22- π electrons of which only 18 of them are delocalized ($4n + 2$ delocalized π -electrons, where $n = 4$). As result of this extensive conjugation, porphyrins are intensely coloured and strong absorption in visible zone of the Uv-Vis spectrum are expected. The porphyrin *core* (i.e. nucleus) is a tetradentate ligand with a diameter of 3.7 angstrom approximately, suitable for binding most of transition metals (e.g. Fe, Cu, Zn, Sn, Ni, Mn etc.).^[67,70] The coordination causes the removal of two protons from the pyrrole nitrogen atoms, leaving two negative charges. The porphyrin complexes with transition metal ions are very stable, for instance the stability constant for ZnTPP ,Zinc(II) mesotetraphenyl porphyrin, is 10^{29} .^[67]

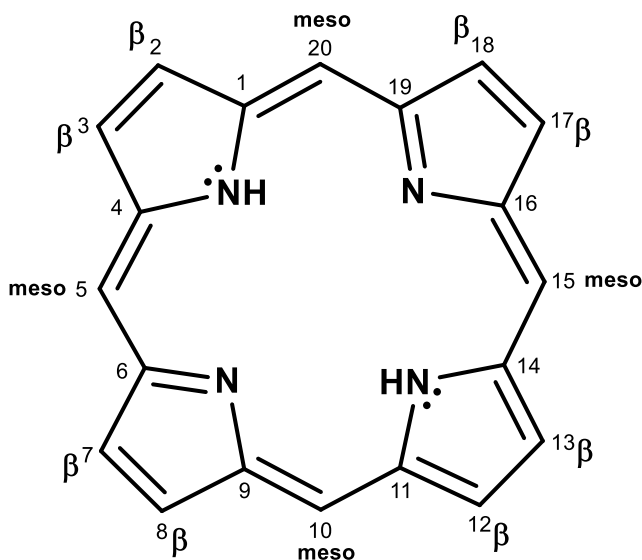


Fig.4 Free base porphyrin structure.

Porphyrins have been studied and employed in a wide variety of research and disciplines comprising photosynthesis,^[71,72] photovoltaic cells,^[73–75] photodynamic therapy,^[76–78] sensing,^[13,79–82] conductive organic materials,^[83,84] information storage,^[85,86] NLO materials,^[87–89] molecular wires,^[90,91] metal-ligands supramolecules,^[92–94] self-organized nanomaterials^[95–97] and so forth. However, the design the tailored porphyrin is essential in order to achieve these fascinating features. For instance, *i*) hydrophilic or charged substituents can be inserted to increase solubility in water; *ii*) porphyrins for photovoltaic applications require donor and acceptor moieties at exact positions; *iii*) in electron transfer based on porphyrin aggregates appropriate redox potential is necessary.^[68,98]

In addition, such complex and elaborate structures are difficult to prepare using only conventional covalent approach and related porphyrin synthesis. For this reason, an accurate functionalization is a fundamental step towards the

design of tailored *porphyrin building blocks* useful in functional supramolecular materials.^[98]

Post-functionalization of porphyrins can be classified into two large categories: one is the *skeleton-functionalization* and the latter is the *porphyrin core-functionalization*.^[98] In the case of skeleton-functionalization, the porphyrin ring is directly functionalized at the *meso*- and/or *β*- positions (see **Fig.4**). In particular, the *meso-functionalization* is easy, and the corresponding derivatives give rise to the *meso-porphyrin* group. On the other hand, meso-substituents can be further functionalised with specific groups or charged moieties in order to confer unique features in the whole macrocycle. Moreover, as above-mentioned, metals can be inserted into the porphyrin core leading to the formation of the metallo-porphyrins; in this latter case we refer to the porphyrin core-functionalization.^[98]

It is undeniable that the spectroscopic behaviours are highly depending on the presence of substituents and/or metals in the porphyrin ring.^[68,98,99] The large aromatic nature of porphyrins and their derivatives is responsive for the intense absorption properties in the UV/Vis region, mainly owing to $\pi - \pi^*$ (HOMO – LUMO) electronic transitions.^[99,100]

A typical UV/Vis spectra of porphyrins exhibit absorptions in two regions termed *Soret* or *B-band* (~380–450 nm) and *Q-bands* (~500–800 nm).^[99–101] The strong *Soret*-band is due to the second excited transition state ($S_0 \rightarrow S_2$), whilst the weak *Q*-(*quasi*-allowed) bands are ascribable to the first excited state ($S_0 \rightarrow S_1$).[†] ^[99,100] Theoretical analysis of the *Soret* band and *Q*- bands have been developed by Martin Gouterman in the 1960s who proposed his semi-quantitative *Four Orbital Model* to explain the spectra of porphyrins,^[102,103] a mixture of *Hückel* and *Configuration Interaction (CI) theory*.

[†] Internal conversion from S_2 to S_1 is rapid so fluorescence is only detected from S_1 .

According to his theory, the main frontier molecular orbitals are four molecular orbitals, two highest energy occupied (HOMOs) and two lowest energy unoccupied molecular orbitals (LUMOs), respectively. In a metalloporphyrin, with symmetry group D_{4h} , the two HOMOs transform[‡] as a_{1u} and a_{2u} , instead, the two LUMOs transform both as e_g (Fig.5).

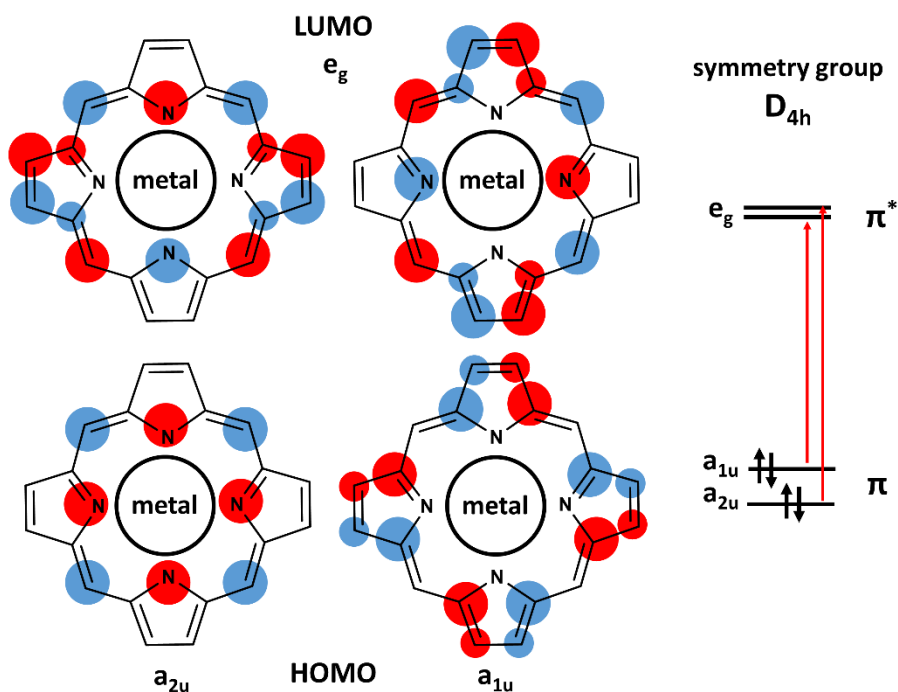


Fig.5 Gouterman's Four Orbital Model for a generic metallo-porphyrin with symmetry D_{4h} . The scheme is described in the text.

In accordance with the Gouterman's model: *i*) the e_g molecular orbitals are strictly degenerate (see Fig.5-right); *ii*) the a_{1u} and a_{2u} molecular orbitals are quasi-degenerate (defined by Gouterman as "accidentally degenerate", see Fig.5-right); *iii*) the electronic configuration of the ground state is $a_{1u}^2 a_{2u}^2$ (with

[‡] according to the *irreducible representations* of the symmetry group

character ${}^1A_{1g}$). Accordingly, the lowest singlet excited states show configurations $\mathbf{a}_{2u}{}^1e_g{}^1$ and $\mathbf{a}_{1u}{}^1e_g{}^1$, both of 1E_u character.

One may envision that this would lead to two absorption bands of very similar energy due to the $\mathbf{a}_{1u} \rightarrow e_g$ and $\mathbf{a}_{2u} \rightarrow e_g$ electronic transitions (**Fig.5-right**). However, by analyzing the UV/Vis spectrum of a hypothetical metallo-porphyrin (**Fig.6**) we observe an intense band about 400 nm (that is the *Soret* or *B*-band) and two weak bands above 500 nm (i.e. Q_0 and Q_1 -bands).

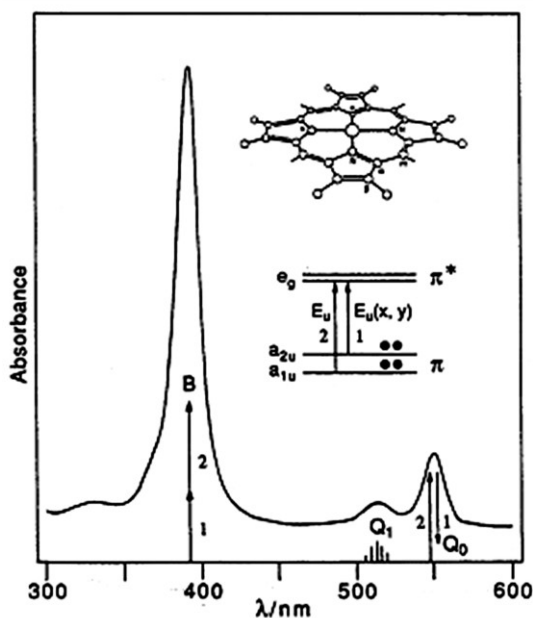


Fig.6 Spectra of a generic metallo-porphyrin.

Martin Gouterman explains these spectroscopic evidences in terms of *configuration interaction (CI)* between the two near-degenerate singlet excited states $\mathbf{a}_{2u}{}^1e_g{}^1$ and $\mathbf{a}_{1u}{}^1e_g{}^1$. In particular when the transition dipoles of the two configurations are constructive, the resulting resonance yields the intense Soret or $B(0,0)$ band. On the contrary, if the transition dipoles of the two configurations interacts destructively, the corresponding resonance leads to the weak $Q(0,0)$

band – namely Q_0 in spectrum shown in **Fig.6**. Noteworthy, the Q_0 band is actually forbidden, however it can “borrow” intensity by the *Soret* band through a *vibronic coupling*, decreasing the *Soret* band’s intensity about 10%. In addition, the higher-energy Q band – namely Q_1 - at relatively constant energy separation from Q_0 is its vibrational overtone (higher of one vibrational mode, ca. 1250 cm^{-1}) and is denoted as $Q(1,0)$.

The difference in the positions and the intensities of the bands observed in the various porphyrin and porphyrin-like derivatives, including the metal-complexes, are explained by the perturbation induced in the relative energies of the four orbitals by the substituent on the porphyrin macrocycle and/or by the interaction with the metal orbitals.^[104] Because of their nodal properties, the d orbitals of a transition metal are not suited to direct interactions with the π frontier orbitals, as can be verified from **Fig.5**. According to Gouterman,^[102] the main effect of the metal on the spectrum results from conjugation of its empty p_z orbital with the π electrons of the rings, which involves the occupied frontier orbital with a_{2u} symmetry. In spite of this modest influence on the spectrum, the inclusion of a metal atom in the porphyrin macrocycle can generate strong electrostatic and *charge transfer* (*CT*) interactions.^[104] For this reason, the metallo-porphyrins can be divided into two groups based on their UV/Vis and fluorescence properties.^[105] *Regular* metallo-porphyrins contain closed-shell metal ions (i.e. transition metals d^0 or d^{10} such as Zn^{II}); in this case the $d\pi$ metal-based orbitals are fully-filled and relatively low in energy. As a consequence, they have very little effect on the porphyrin spectra, making the electronic transitions confined within delocalized π -system of the porphyrin ring. Conversely, in porphyrins containing open-shell metal ions (that is, transition metal with partially-filled d orbitals - d^m $m= 6-9$) can occur MLCT (Metal-Ligand Charge Transfer) transitions between the highest occupied metal $d\pi$ orbital and the empty π^* (e_g) orbital on the porphyrin. This *Metal-to- ligand π backbonding* accounts for the

increasing of the porphyrin $\pi - \pi^*$ gap energy and a blue shift (i.e., *hypsochromic* effect) in the Soret band is revealed.^{[106]†}

A key-difference between the spectra of metallo-porphyrins and their free-base counterparts is the number of *Q*-bands: a free-porphyrin owns the typical *B*-band and further *four Q*-bands. This results from the reduced symmetry of the free-base (D_{2h}) so that the two axes defined by opposite pyrrole nitrogen atoms are no longer equivalent affecting further splitting of the electron transitions.^{[99,100]‡}

The intriguing electronic and spectroscopic features discussed so far make porphyrins appealing molecular synthons for building functional multi-porphyrin assembly. In the next chapter, porphyrin self-assembly and related topics will be treated.

† *Non-Regular* porphyrin are also labelled as *Hypsoporphyrins*

‡ As a result of the reduced symmetry in free-base porphyrin, also the e_g orbitals are *quasi*-degenerate and more electronic transitions are expected. Consequently, the *configuration interaction* between the new transition dipoles generates four *Q*-bands.

2.3

Porphyrin self-assembly

The importance of multiporphyrin assemblies is observed in Nature, where most of systems are based on several porphyrins -or their derivatives- and arranged in a well-organized in order to define electronic or catalytic properties.^[107] Without doubt, the most important chromophoric array that is found in nature is the light-harvesting complex employed for photosynthesis by green plants and purple bacteria.^[108-111] Another interesting example of a multiporphyrin assemblies is that of *cytochrome c₃*, a hemoprotein isolated from the sulphate-reducing bacteria of the genus *Desulfovibrio*.^[112] The X-ray structure shows that the four hemes of the system are arranged in a non-parallel fashion.^[113]

Noteworthy, the conventional synthetic strategies to build porphyrin arrays have generally provided quite limits; numerous steps followed by laborious separation of reaction mixture, resulting in a low product yield.^[114,115] Conversely, self-assembly has emerged as a viable alternative to covalent synthesis in the construction of large multi-component porphyrin architectures.^[114,116] Nevertheless, the common characteristic of all biological self-assembly processes is the ability to take advantage of various weak noncovalent interactions between preformed building block to guide the formation of a superstructure.^[117] In fact, noncovalent interactions are responsible for the stability of the final structure as a result of the reached thermodynamic minimum.^[114,117] Non covalent self-assembly is an approach that offers several advantages, that is *i)* easy synthesis of monomers, *ii)* thermodynamically stable final structures, and *iii)* the possibility of self-repair, due to intrinsic nature of non-covalent bonds.^[116]

The structure and spectroscopy of the porphyrin aggregates are of much interest because of the special properties and possible technological applications of the mesoscopic materials which are intermediate between molecules and solids.^[118] Although an aggregation process may lead to various types of assemblies, in a more wide-ranging view, of particular interest are those aggregates in which the molecular arrangement is highly ordered, and unique electronic properties are expected. In this sense, pure *H*- or *J*- aggregates appear as striking models for understanding molecular interactions in aggregation processes and for technological applications in molecular devices.^[95,118]

In *J*- aggregates, monomers are organized in such a way as to ensure an edge-to-edge (or side-by-side) arrangement in one dimension (**Fig.7-right**). As such, electric dipole moments of the monomers are parallel and the angle between the transition moment and the line joining the molecular centres is zero (ideal case).^[95,118–120] The first independent observation of *J*- aggregates is due to *E.E. Jelley* (from which the initial “*J*-“), who discovered the phenomenon first, in 1936.^[121] Contrarily, *H*- aggregates (*H*- for hypsochromic, see below) are a one-dimensional *face-to-face* arrangement of strongly coupled monomers (**Fig.7-left**). Here, the electric dipole moments of the monomers are perpendicular (ideal case) and the angle between the transition moment and the line of molecular centres is 90° .^[95,118–120]

These aggregates exhibit remarkable spectroscopic differences in the absorption band compared to the monomeric species.^[118,122] Perhaps, the first significant explanation concerning their photophysical properties dates back to 5 decades ago, thanks to was A.S. Davydov -in molecular crystals-,^[123] and resumed by M. Kasha in non-crystal molecular aggregate.^[124]

generating allowed and forbidden electron transitions which depends on geometric arrangements, *J*- or *H*- stacking (Fig.8).^[124]

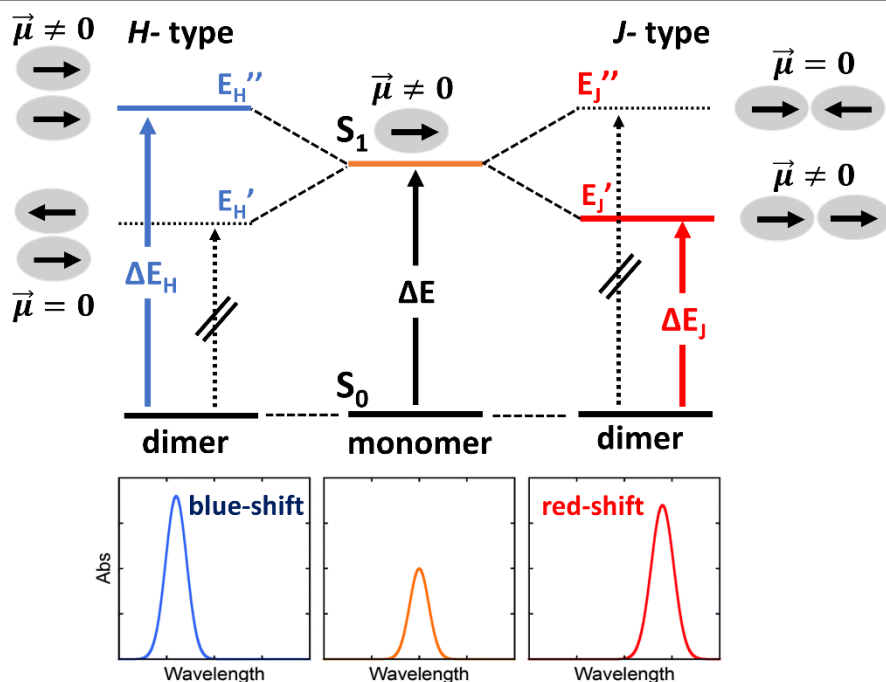


Fig.8 Schematic illustration of the “Exciton splitting model”. Detailed description in the text.

Fig.8 shows the energy level diagrams of the *exciton splitting* as a result of the interactions of two identical monomers, in two boundary geometries: i) parallel arrangement, namely *H*-type (Fig.8-left) and ii) in-line arrangement, that is *J*-type (Fig.8-right).

In the case of *H*-type (Fig.8-left), when the electric dipoles interact out-of-phase the coupling is electrostatically favoured and a lower energy level E_H' is obtained. Otherwise, in-phase coupling gives repulsion so that the energy level E_H'' is displaced upwards from the origin. The transition dipole moment $\vec{\mu}$ is given by the vector sum of the individual transition dipole moments in the assembly. Thus, transitions from the ground state to exciton state E_H' are forbidden ($\vec{\mu} = 0$), while transitions from the ground state to higher exciton state

E_H'' are allowed ($\vec{\mu} \neq 0$). Consequently, the ΔE_H transition in H -dimer is more energetic and a blue-shifted absorption is expected.[†]

Regarding the J -type (**Fig.8-right**), from the diagram it is readily seen that the in-phase arrangement of transition dipoles leads to an electrostatic attraction, producing the lower excited state E_J' , whereas the out-of-phase arrangement of transition dipoles causes repulsion, producing the higher state E_J'' . On the other hand, the transition moments are finite for electric dipole transitions from the ground state to E_J' ($\vec{\mu} \neq 0$), and 0 to the state E_J'' from the ground state ($\vec{\mu} = 0$). Thus, it will be apparent that the in-line transition dipole case will lead to the observation of a strong spectral red shift for the transition in the dimer compared with that for a monomer.

The exciton splitting energy (often called *Davydov splitting*), corresponding to the separation

$$\Delta\xi = E'' - E' \tag{eq.1}$$

is given by the equation:^[122,124]

$$\Delta\xi = \frac{2 |\vec{\mu}|^2}{r^3} (\cos \alpha + 3 \cos^2 \theta) \tag{eq.2}$$

where $\vec{\mu}$ is the transition moment for the singlet-singlet transition in the monomer, r is the center to center distance between the monomers in the dimer, α is the angle between-polarization axes of the two monomer absorbing units and θ is the angle made by the polarization axes of the monomers with the line of molecular centers. A characteristic feature of exciton theory is illustrated by

[†] Compared to the electronic transition ΔE of the single monomer.

equation 2. It is seen that the exciton splitting energy is directly related to the square of the transition moment for the monomers. Thus, greater the intensity of light absorption in the single monomer, greater is the exciton band splitting. Another characteristic feature of exciton theory is the dependence of the exciton splitting on the inverse cube of the intermolecular distance. Finally, the geometrical parameters enter in the manner characteristic of the structure of the composite molecule.

If a chromophore is chiral[†], its interaction with polarized light is very specific and can provide important methods for characterizing both small molecule and supramolecular structures. Essentially, one type of measurements commonly made to determine the effects of polarized light on asymmetric molecules is *Circular Dichroism* (CD), which is defined as the difference in absorption of left-hand and right-hand circularly polarized light with optically active compounds.[‡]^[126,127] Furthermore, when two (or more) asymmetric chromophores are located near in space and have a proper (chiral) mutual orientation, the electronic coupling occurs (see the Kasha's model above), causing, in turn, a strong magnetic coupling.^[127] As above-reported, the splitting of excited states reflects in a split or broadened absorption band, centered around the wavelength transition λ_0 of the isolated chromophore. If the two transition moments are not coplanar, the magnetic moment generated by the oscillating *dipole 1* at the end of the *vector* \vec{r}_{12} will be nonorthogonal to *dipole 2*, and vice-versa. As a consequence, a *bisignate* CD couplet is generated around λ_0 as illustrated in **Fig.9**.^[127]

[†] A molecule is considered to be chiral (or asymmetric) when its mirror image is not superimposable.

[‡] In other terms, CD can be measured *only* in correspondence to chromophores' absorption bands. See *Appendix* of this thesis for a detailed description about Circular Dichroism.

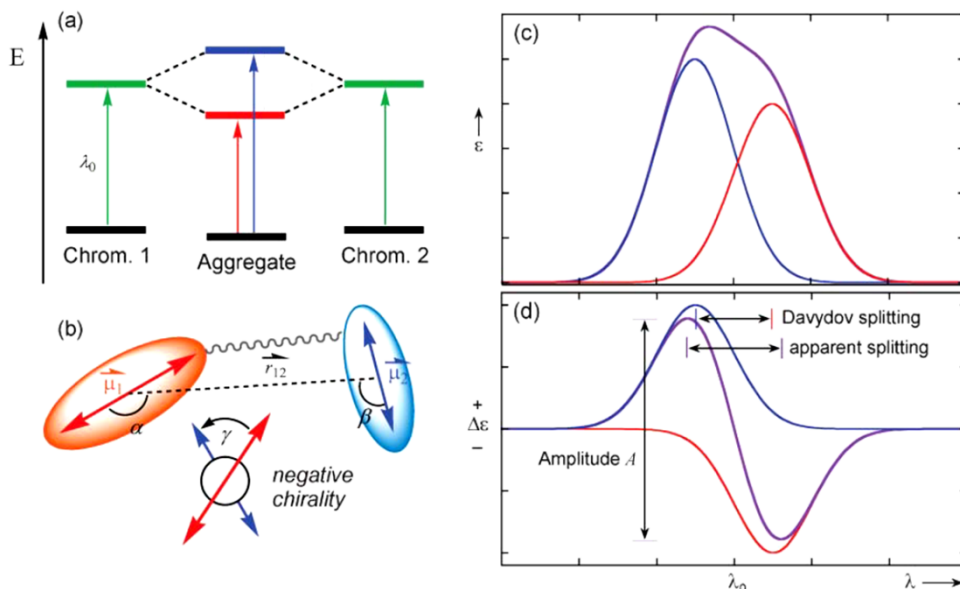


Fig.9 (a) Splitting of the excited states of two degenerate exciton-coupled asymmetric; (b) definition of geometrical parameters necessary for predicting CD sign; expected absorption (c) and CD spectra (d) in case of exciton splitting as shown in (a): component spectra thin lines in blue/red, resultant spectra thick lines in violet. The distance between the peak and the trough of the split CD curve is called amplitude or A . All figures are reported from ref.^[127]

The sign of exciton chirality can be evaluated in the following way: upon looking through the centers of the two dipoles, a negative sign is defined when an anticlockwise rotation by an acute angle brings the dipole in the front onto that in the back (see **Fig.9-b**). The exciton chirality rule states that a positive chirality corresponds to a positive CD couplet and vice-versa.^[127]

The simplest examples of self-assembly processes are those concerning homo self-aggregation of the diacid (zwitterionic) forms of the anionic porphyrins.^[128] Among them, a special place is occupied by the processes involving the protonated form of meso-tetrakis(4-sulfonatophenyl)porphyrin, H_4TPPS4 ($pK_a \approx 4.8$, see **Fig.10**). Indeed, under acidic conditions ($pH < 2.5$), H_2TPPS4 is converted to the protonated species and forms both J- (edge-by-edge assemblies) and H-aggregates (face-to-face stacking).^[120] This spontaneous self-assembly through non-covalent events is strongly dependent, in aqueous solution,

on many chemical–physical parameters, i.e. pH, concentration, time, ionic strength, and the history of solution preparation.^[57,129–131]

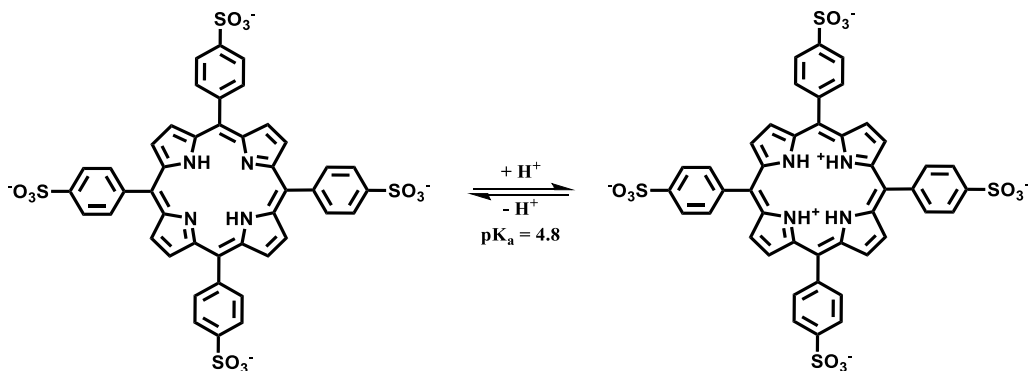


Fig.10 Acid-base equilibrium between free-base H_2TPPS4 and its protonated form, H_4TPPS4 .

If a chiral (non-racemic) *guest* and an achiral chromophoric molecules as *host* (e.g. crown ethers or calixarenes) form a chiral *host–guest complex*, a CD signal is induced (*Induced Circular Dichroism* - ICD) within the absorption bands of the host.^[127,132] Inversely, a small guest molecule which is achiral and hence its chromophores are optically inactive, upon binding to a biopolymer host, such as proteins, polypeptides, oligonucleotides, oligosaccharides may produce an induced CD due the chiral perturbation by the biopolymer host.^[126,127,132–134] Nevertheless, the coupling between several guest molecules bound to different sites of a macromolecular host may result in a significant induced CD spectrum.^[135] In several cases, CD lends itself not only to a detection of host–guest interactions, but also to the analysis of binding modes, association–dissociation kinetics and thermodynamics.^[127]

In this regard, supramolecular arrangements of achiral molecules, such as porphyrins, can result in chiral supramolecular structures as a consequence of energy minimization of the final aggregate structure. The first evidence that it is possible to exert a fine control on chirality of supramolecular J-aggregates

through chiral agents and stirring forces is due to the Kobayashi's group in 1993.^[120] In addition, Barcelona's group led by Ribò, demonstrated that clockwise or counter-clockwise rotation of a vessel, during the slow evaporation of a solution containing the protonation form of meso-tri-sulfonatephenyl porphyrin (H₄TPPS₃), induces the two enantiomeric forms of the J-aggregates.^[136]

However in the absence of chiral perturbation, chirality can also be induced using chiral templates such as polymers, aminoacids or chiral metal-complexes.^[16] In this respect, aggregation of water-soluble porphyrins onto oppositely charged polymeric chiral templates constitutes not only a quite simple strategy that allows for building tailored supramolecular species, but it is also a direct way to rule chirality of porphyrins at a supramolecular level.

For this reason, in the next chapters I will illustrate, first, the principles of the state-of-the-art concerning the porphyrin self-assembly modulated by polypeptides and afterwards, the experimental evidences discovered at Università degli Studi di Catania in this field.

3.1

Porphyrin aggregation modulated by polypeptides : State-of-the-art

In *Green Plants*, the photophysical properties of the supramolecular systems, chlorophyll pigment-protein matrix, are supposed to be responsible for the process of photosynthesis.^[137] For this reason, since the early 1980s numerous investigations were performed about hypothetical pigment-matrix models. Nevertheless, in 1972 *Pasternack et al.* published an extensive work regarding the self-aggregation of water soluble meso-functionalized porphyrin.^[138] This latter study paved the way to the large employment of porphyrins, and related derivatives, as artificial pigment to investigate and reproduce the natural photophysical process.

In this context, *Pancoska et al.* demonstrated that the meso-tetrakis(4-carboxyphenyl) porphyrin, H₂TCPP (**Fig.11**), is able to interact with poly(L-lysyl-L-leucyl-L-alanine)_n, LLA, and poly(L-lysyl-L-alanyl-L-alanine)_n, LAA. In fact, the coulombic interactions between the anionic H₂TCPP and protonated ϵ -amino groups in the side chain of the amino acid L-lysine incorporated regularly into the polypeptide primary, simulates the pigment-protein complex in vivo accurately.^[139,140] They observed that the maximum absorbance of a pure buffer solution (pH=7.2, [H₂TCPP]= 10⁻⁵M) of H₂TCPP (λ_{max} = 413nm) differs than H₂TCPP-LAA, λ_{max} = 405nm, and H₂TCPP-LLA, λ_{max} = 421nm. In particular, both overall intensity and band intensity depend on the concentration of added polypeptide (**Fig.12**).

3.1 Porphyrin aggregation modulated by polypeptides:
State-of-the-art

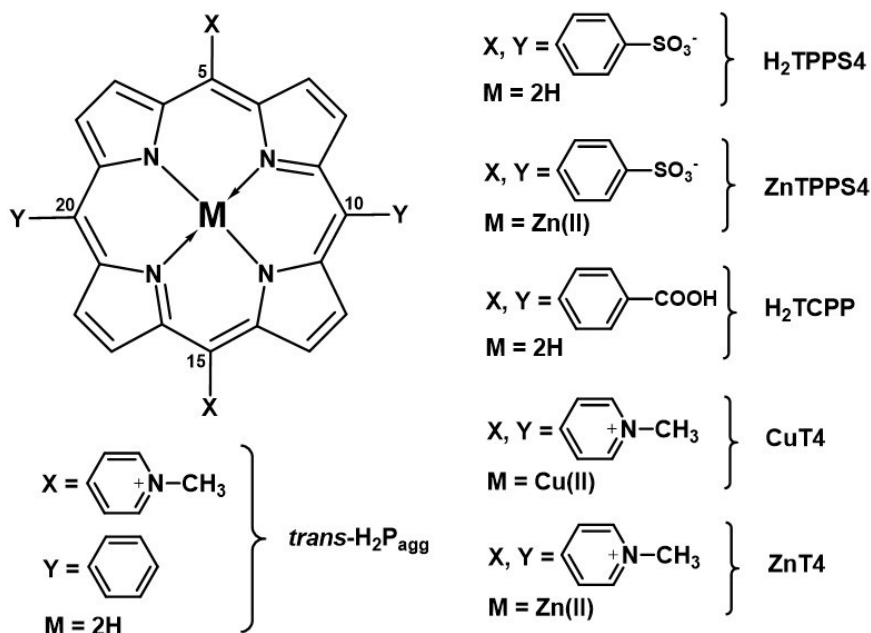


Fig.11 Molecular structure of the main porphyrin discussed in this section.

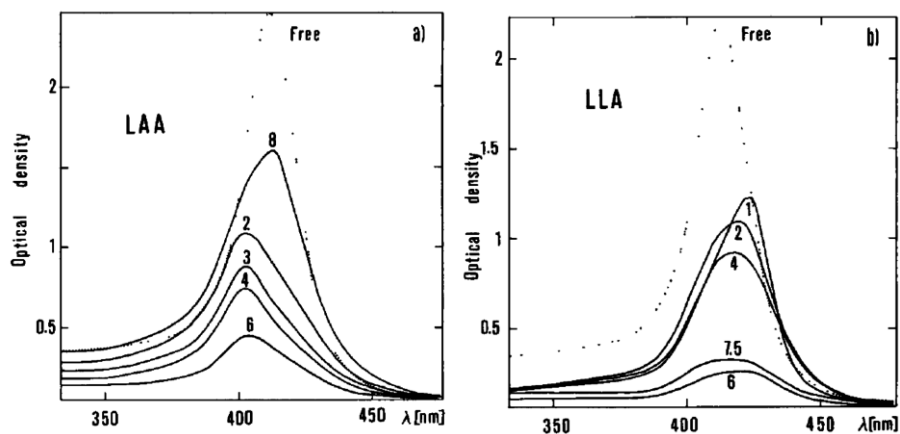


Fig.12 (a) Soret region of the absorption spectra of free $\text{H}_2\text{T CPP}$ and $\text{H}_2\text{T CPP-LAA}$ complexes. The curves for the complexes are identified by increasing the polypeptides/porphyrin ratio. Blue-shifted maxima characterizes the complexed pigment. **(b)** Soret region of the absorption spectra of $\text{H}_2\text{T CPP}$ and $\text{H}_2\text{T CPP-LLA}$ complexes. The curves are identified as above. Maxima for the complexed pigment are red-shifted compared with those of the free pigment.

Furthermore, a circular dichroism signal is induced in the Soret region by the interaction of the rigidly fixed H₂TPPC with the chiral LLA and LAA polypeptide molecules (both in α -helix at this experimental conditions) as reported below in **Fig.13**.

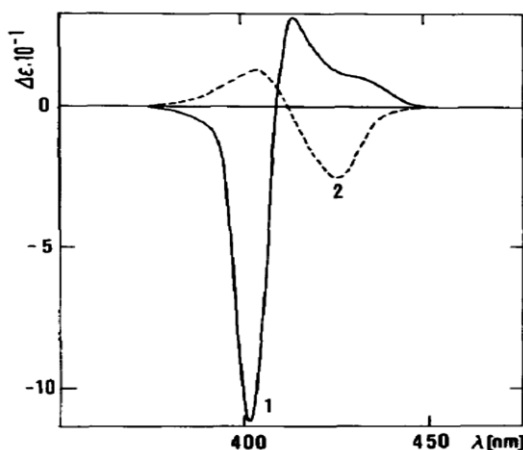


Fig.13 Induced circular dichroism spectra of porphyrin complexed with LAA (solid line) and LLA (dashed line). Porphyrin/polypeptide ratio is 2:1 in both samples.

The author explained of these changes in terms of the appearance of new absorption bands and induced CD as a result of the (chiral) peptide field which removes the porphyrin's symmetry-forbidden character.^[139,140]

Afterwards, *Pasternack* and *Gibbs* demonstrated an extensive interaction between the di-cationic trans-bis(N-methylpyridinium-4-yl) diphenyl porphyrin, *trans-H₂P_{agg}* and anionic polyglutamate at pH 4.5 (α -helix) and 7 (random coil) by means of the appearance of an intense induced CD in the Soret region (**Fig.14**).^[141,142]

3.1 Porphyrin aggregation modulated by polypeptides: State-of-the-art

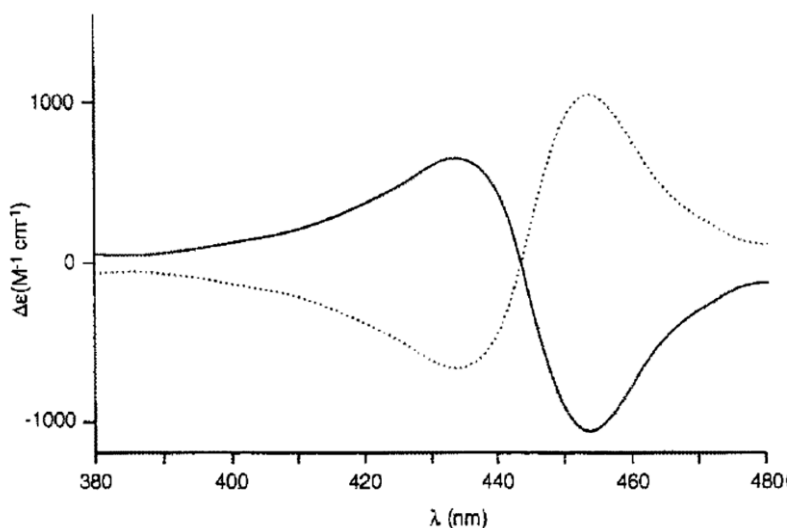


Fig.14 Induced CD spectrum of *trans*- H_2P_{agg} with polyglutamate at pH 4.5 and $[NaCl] = 100$ mM; L-Polyglutamate (dotted plot); D-polyglutamate (solid plot).

Authors conclude that porphyrins are able to form long-range assemblies on a polymer template (both in helix-conformation and random coil) depending on the tendency of the porphyrin to aggregate in the absence of the polymer . Nevertheless, such arrays should be possible on any helical polymer to which the porphyrins will bind.^[141,142]

Bellacchio et al. in 1998 illustrated that the aggregation processes for *i*) tetra-anionic meso-tetrakis-(4-sulfonatophenyl) porphyrin, H_2TPPS4 (**Fig.11**), in presence of protonated polylysine^[19] and for *ii*) tetra-cationic copper(II) meso-tetrakis(4-N-methylpyridyl)porphyrin, $CuT4$ (**Fig.11**), with negatively charged polyglutamate^[143] lead to formation of chiral binary species, kinetically labile by pH tuning in a reversible fashion (see below).

In the first case, the evidence of an extensive H_2TPPS4 self-assembly onto the polylysine is confirmed by *i*) remarkable hypochromicity and blue-shift in the Soret band (**Fig.15-left**) and *ii*) an induced CD signal in the same Uv-Vis region, demonstrating the chirality transfer from chiral mould to the porphyrin

arrangement (**Fig.15-right**). Notably, if the pH value is increased up to 10 (from pH=7), the ICD signal is observed to be amplified. This latter effect may be explained in a major spatial organization of the chromophore when an α -helix conformation of the polylysine is reached (at pH = 7 the polylysine is mostly in random coil conformation).

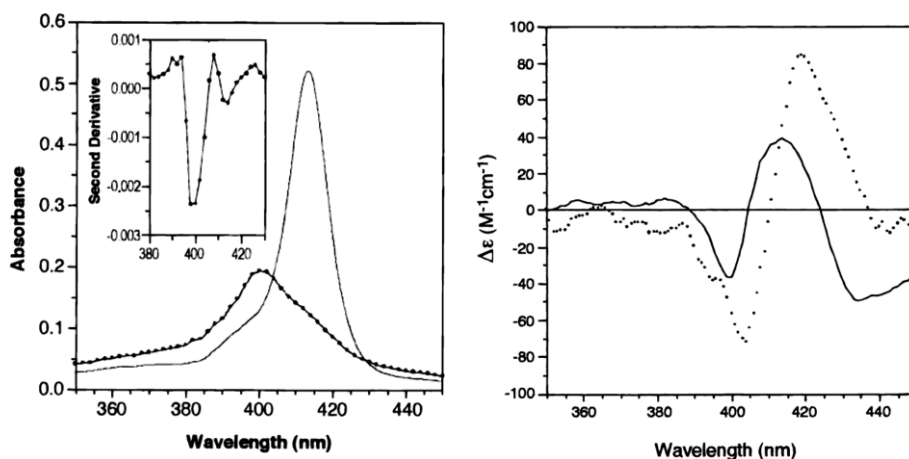


Fig.15 Left-Absorption spectra of H_2TPPS4 ($1 \mu M$) in the absence (continuous line) and in the presence (dotted line) of polylysine ($100 \mu M$). The inset shows the second derivative of the spectrum obtained in the presence of polylysine. Right- CD spectra of H_2TPPS4 ($1 \mu M$) in the presence of polylysine ($100 \mu M$), at pH 7 (solid line) and pH 10 (dotted line).

Moreover, the electrostatic interaction between cationic CuT4 and anionic poly-L-glutamate is shown thanks to the appearance of optical activity in porphyrin's *B*-band (curve *a* in **Fig.16**). The labile nature of such binary aggregates is also illustrated by the ICD inversion when a strong excess of the *D*-enantiomer is added to the same system (curve *b* in **Fig.16**).

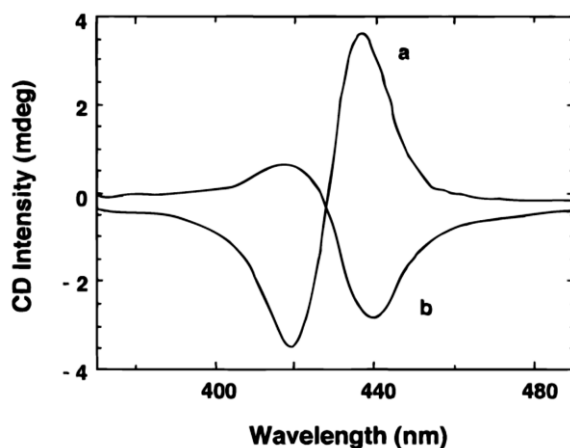


Fig.16 CD spectra of: (a) a solution of CuT4 (4 μ M) in the presence of poly-L-glutamate (200 μ M) at pH 3.6 and (b) the same solution, after the addition of a 4-fold excess of poly-D-glutamate.

To date, the experimental evidences of the interaction between ionic porphyrins and oppositely charged polypeptides have been well-discussed. It is worth to consider that anionic porphyrins, such as H₂TPPS4, are not able to bind anionic matrices directly, e.g. poly-glutamate, as a result of electrostatic repulsions. However, the presence of a cationic constituent pre-organised onto anionic polypeptide may lead to ternary supramolecular assemblies, promoting as well, the aggregation of the anionic dye. This hypothesis was confirmed, by adding the H₂TPPS4 (at strong acid condition) in the system containing the binary assembly ZnT4-poly-glutamate (see **Fig.11** for the structure of ZnT4).^[119] As previously reported, H₂TPPS4 can form *J*-aggregate as a consequence of the protonation and subsequent self-assembly, at acid pH values. Nevertheless, the appearance of an induced chiral signal in *J*-agg's absorption band ($\lambda \approx 490$ nm) in **Fig.17**, as a result of the H₂TPPS4 addition to preformed ZnT4-polyglutamate system, proves the formation of a ternary assembly. A reasonable explanation takes into account the fact that cationic metallo-porphyrin, ZnT4, acts as *spacer* minimizing the repulsion between two negative components (porphyrin and

polymeric template), by inducing as well, the lateral J-aggregation of anionic porphyrins H₂TPPS4 because of stacks being prevented for steric or charge repulsion reasons.^[119]

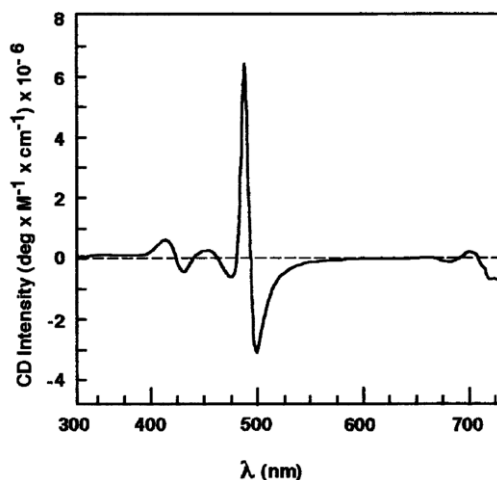


Fig.17 ICD spectrum of H₂TPPS4 (5 μM) in the presence of ZnT4 (5 μM) and poly-L-glutamate (50 μM). pH 2.9, citrate buffer 5 mM.

The first evidence of directly templated J-aggregates onto polypeptide matrix was due to *Periasamy* in 2003.^[95] His research group observed that poly-(L or D)-lysine induces J-aggregation of H₂TPPS4 more efficiently than monomeric lysine, see the black thin line in **Fig.18**. Only micromolar concentration of polylysine was required for complete conversion of the porphyrin monomer to its J-aggregate. Noteworthy, J-aggregates of H₂TPPS4 are chiral and the chirality is induced by the optically active lysine in the template (data not shown).^[95]

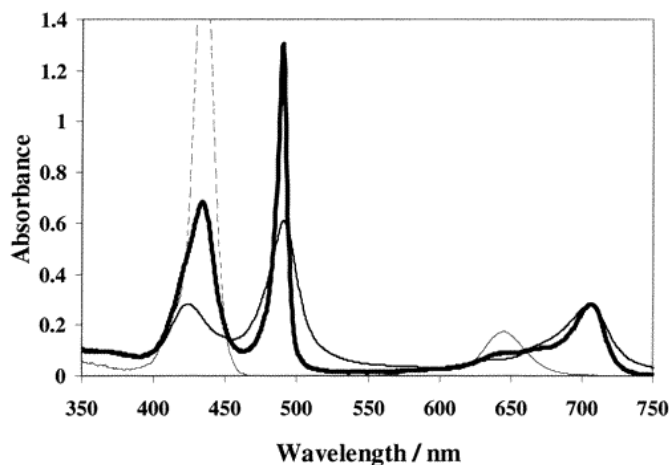


Fig.18 Absorption spectra of the monomer (dashed line) and J-aggregate of H₂TPPS4 with l-lysine (thick line) and poly-DL-lysine (thin line) in pH 3.0 buffer. Concentration of H₂TPPS4 is 9 μ M in all cases. J-aggregate spectra were obtained using l-lysine (100 mM) and poly-DL-lysine (\sim 5 μ M of polymer or 100 μ M of lysine residues).

Other very interesting examples concerning aggregation of the tetra-anionic H₂TPPS4 onto suitable templates were published from the groups of professors M. Liu^[15] and E. Yashima.^[144] The first group investigated the interaction of the protonated, zwitterionic form of H₂TPPS4 (H₄TPPS4) with L- and D-poly-lysine, observing the formation of chiral H- and J-aggregates. Interestingly, they reported that the exciton couplet of the J- and H-assemblies can have the same or opposite signs, thus suggesting different chirality. This difference was attributed to the hierarchical phenomenon (the different mixing sequence) and observed for poly-lysine to H₂TPPS4 ratios higher than 4.^[15]

Yashima and co-workers have reported a very intriguing work in which an induced helix of poly(phenylacetylene) is, in turn, able to induce chirality to aggregates of H₄TPPS4, which show *memory* of the induced chirality.^[144]

Of course, self-aggregation is mainly driven by protonation of the porphyrin core, but also or the presence of a metal in the porphyrin core strongly influences their aggregation pathway.^[131] Moreover, metalloporphyrins can lose

their central metal ions in different experimental conditions depending on several factors, such as metal size and coordination, degree of covalent bonding, and oxidation state.^[145]

In this respect, tetra-anionic Zinc(II) meso-tetrakis-(4-sulfonatophenyl)porphyrin (ZnTPPS4, see **Fig.11**) is a metallo-porphyrins widely studied for research field in photocatalysis and solar cells,^[146,147] biochemistry and sensing.^[148,149] It has been reported that ZnTPPS4 aggregates in the presence of polylysine, confirming the porphyrin aggregation onto oppositely charged matrices.^[19,150] However, the self-assembly on PLL at neutral pH is limited to the formation of face-to-face dimers (with a characteristic absorption band at 414 nm, see dotted line in **Fig.19**-left), owing to the presence of one water molecule as an axial-ligand of central the metal Zn(II), see below **Fig.19**-right.^[19,150] Nonetheless, water solutions of ZnTPPS4 are not steady under acidic conditions (pH < 4.5) leading to related demetalated/protonated forms (H₂TPPS4, H₄TPPS4).

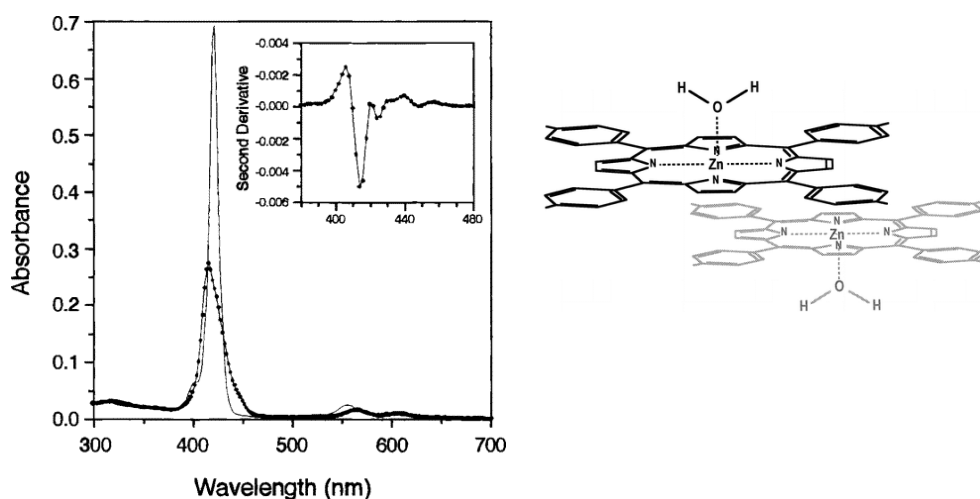


Fig.19 Left- Absorption spectra of ZnTPPS4 (1 μ M) in the absence (continuous line) and in the presence (dotted line) of polylysine (25 μ M). The inset shows the second derivative of the spectrum obtained in the presence of polylysine. **Right-** Schematic representation of a possible ZnTPPS4 dimeric form.

Recently, we have reported the behaviour of ZnTPPS4 solutions at different pH values, highlighting the role played by polyelectrolytes on the aggregation step after protonation in acid.^[28]

In particular, we observed that the poly-L-lysine (PLL) affects the overall demetallation/protonation process catalyzing at the same time the formation of J-aggregates.^[28] Probably, the PLL chain length may affects the formation, kinetics, and chirality of J-aggregates formed after ZnTPPS4 demetallation at acid pH values. These observations will be subject of the following chapter, describing as well, the first part of my experimental data.

3.2

Results and Discussions

The addition of HCl to a aqueous solution (2 μM) of ZnTPPS4 (**Fig.11**) (purchased from Sigma-Aldrich and used without further purifications, $\epsilon_{421\text{nm}/\text{H}_2\text{O}} = 6.83 \times 10^5 \text{ M}^{-1}\text{cm}^{-1}$) triggers an vigorous demetallation followed by formation/protonation of H_2TPPS_4 visible by the shift of the Soret band maximum from $\lambda = 421$ to $\lambda = 434 \text{ nm}$.^[28,147,151] In particular, the demetallation of bare ZnTPPS4 has been studied at different pH. **Fig.20** reports the decrease of Soret band at 421 nm (**Fig.20**-panel A) of ZnTPPS4 and the related increase of the band at 434 nm (**Fig.20**-panel B) attributed to H_4TPPS_4 (see **Fig.10**) formation upon varying time and solution acidity.

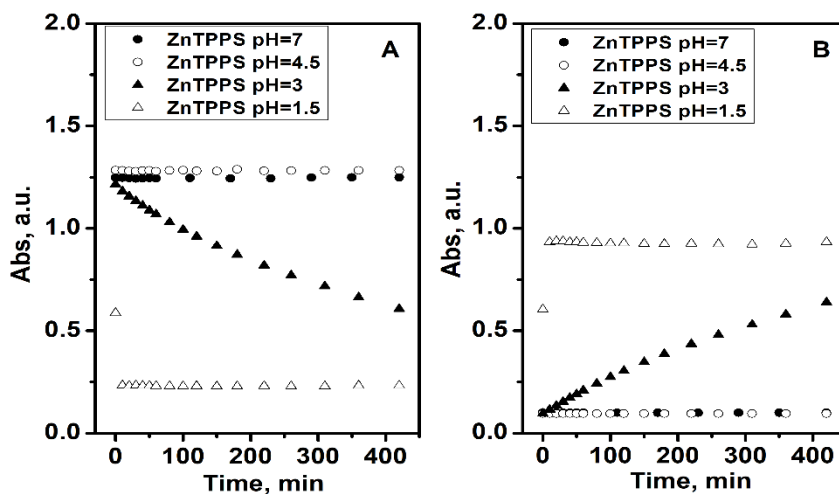


Fig.20 Panel A: absorption variation at 421 nm vs. time of ZnTPPS4 solution (2 μM) at pH 7 (black full circles), pH 4.5 (empty circles), pH 3 (black full triangles) and pH 1.5 (empty triangles). **Panel B:** absorption variation at 434 nm vs. time of ZnTPPS4 solution at pH 7 (black full circles), pH 4.5 (empty circles), pH 3 (black full triangles) and pH 1.5 (empty triangles).

As expected, protonation starts at $\text{pH} < 4.5$ and proceeds fastly upon further decreasing pH . Noteworthy, at $\text{pH} = 1.5$ an instantaneous protonation occurs: in fact, the initial absorbance value at 421 nm is significantly lower (about half) than that observed at higher pH , while a component at 434 nm is immediately observed in these conditions (**Fig.20**).

Although $\text{H}_4\text{TPPS4}$ owns a zwitterionic nature, the formation of J-aggregates ($\lambda_{\text{max}} = 490 \text{ nm}$) is not observed in a diluted solution ($2 \mu\text{M}$) of ZnTPPS4 at $\text{pH} 1.5$, except when ionic strength is increased up to $[\text{NaCl}] = 0.3 \text{ M}$ after 60 min. (see below blue continuous line in **Fig.21**).

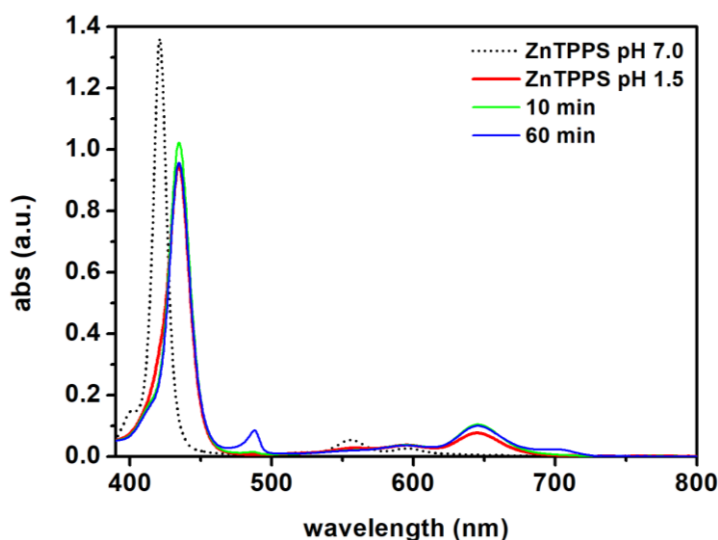


Fig.21 UV/Vis of $2 \mu\text{M}$ ZnTPPS4 solutions at $\text{pH} 7$ (black dotted curve) and $\text{pH} 1.5$ ($t = 0$ -red curve, 10 min -green curve, 60 min -blue curve) in presence of $\text{NaCl} 0.3\text{M}$ at 25°C .

The intrinsic solvophobic nature of tetra-anionic porphyrins (well soluble in water) make them able to interact with polycationic templates by triggering system electrostatics as well as dispersive forces. Accordingly, demetallation/core protonation of ZnTPPS4 at pH values ranging from 7 to 1.5 has been investigated by using cationic poly-L-lysine, PLL ($[\text{PLL}] = 50 \mu\text{M}$, degree

of polymerization (dp) = 68). Cationic polylysine (PLL), able to electrostatically interact with anionic ZnTPPS4, reduces its demetallation rate as reported in **Fig.22** by monitoring the absorption at 421nm vs. time.

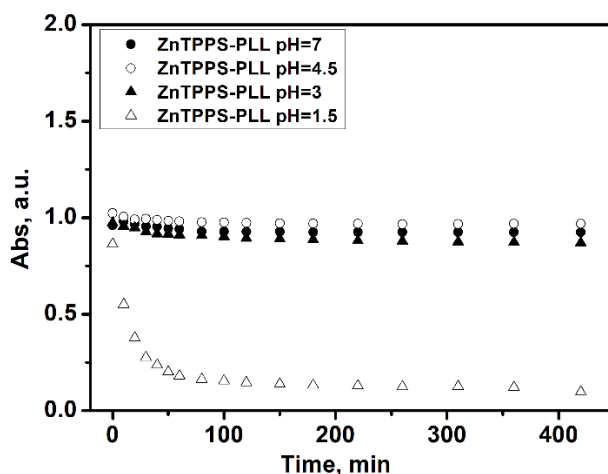


Fig.22 Absorption variation at 421 nm vs. time of ZnTPPS4-PLL solution at pH 7 (black full circles), pH 4.5 (empty circles), pH 3 (black full triangles) and pH 1.5 (empty triangles).

The **Fig.23** shows the Soret band evolution of the investigated solutions recorded 4 hours later the addition of ZnTPPS4 to acidic solution (at pH = 1.5). The protonation is complete for ZnTPPS4, as indicated from the peak at 434 nm associated to protonated H₄TPPS4: noteworthy, no aggregation is observed. On the contrary, for ZnTPPS4-PLL the presence of the peak about at 490 nm indicate the formation of *J*-type aggregates.

To discuss this experimental evidence we invoke the role of PLL to act as aggregation agent for protonated H₄TPPS4 that can bind to polymer chain according to the length of the chain and the availability of the binding sites.^[19] At pH = 3 we can assume that PLL acts as proton sink, thus competing with protonation of ZnTPPS4 that binds to polymeric chain as a pending molecule, thus maintaining its monomeric form. By lowering pH, protonation occurs and, as discussed by other authors,^[15] protonated porphyrins in proximity of PLL

chains rearranged along the groove of polyelectrolyte in a head-to-tail conformation, thus forming J-aggregates. PLL, in fact, is positively charged at $\text{pH} = 1.5$ and strongly attracts anionic porphyrins. The immobilization of $\text{H}_4\text{TPPS4}$ molecules through negatively charged SO_3^- groups catalyzes the attachment of other porphyrin molecules since their negative charge is partially diluted by the cationic nature of template.

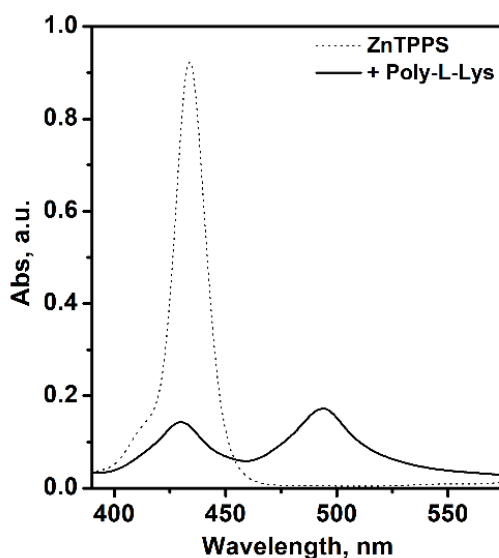


Fig.23 Absorption spectra of ZnTPPS4 ($2\mu\text{M}$, dotted curve) and ZnTPPS4-PLL solution ($[\text{PLL}] = 50\mu\text{M}$ dp 68, solid black curve) at $\text{pH} 1.5$ after 4h.

The effect of polylysine on the ZnTPPS4 opens some questions and perspectives. First of all, what is the role of PLL chain length on the entire process? And more, what about the transfer of chirality from PLL to porphyrin aggregates?

For this reason, we carried out several experiments using PLLs with different degrees of polymerization, from dp 36 to 2060 (commercially available and used without further purifications).

In detail, ZnTPPS4 2 μM was added to each water solutions of PLL (50 μM) with different polymerization degree. Then, solutions were incubated for 15 minutes at neutral pH to favor a system rearrangement. Afterwards, absorbance and fluorescence variations were monitored to confirm the occurrence of aggregative process, see below in **Fig.24**.

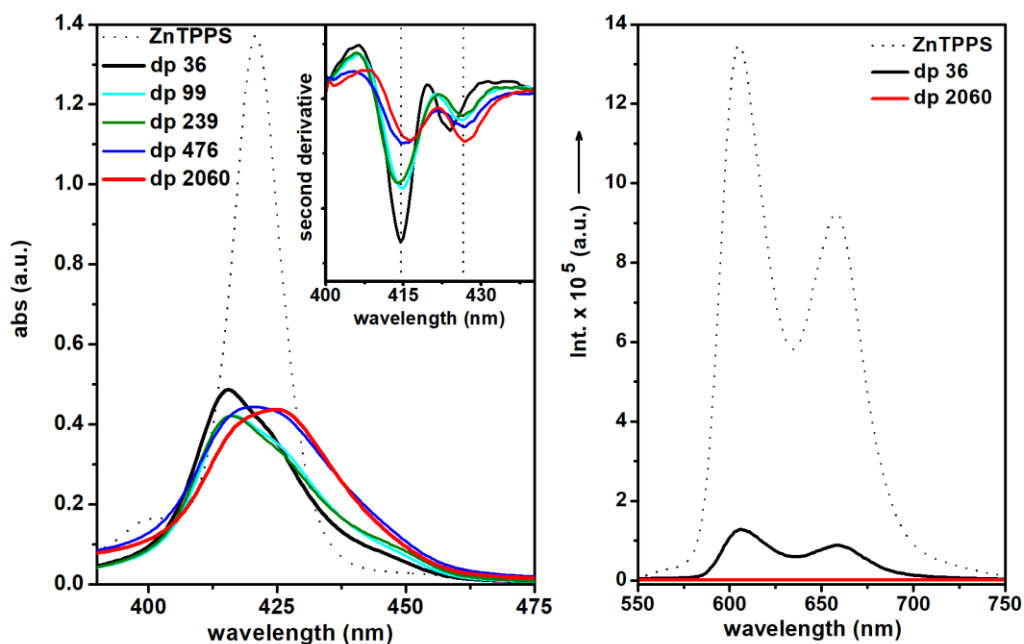


Fig.24 UV/Vis (inset: second derivative) and fluorescence ($\lambda_{ex} = 421$ nm) spectra at neutral pH of bare ZnTPPS4 (2 μM , black dotted curves) and in the presence of various PLL (50 μM , dp 36-black, dp 99-cyan, dp 239-green, dp 476-blue, and dp-2060 red).

As expected, due to the electrostatic attraction, a strong interaction causes a hypochromic effect and a broadening of the porphyrin Soret band at 421 nm. Moreover, from the second derivative of the Soret band, we can identify two components, at $\lambda \approx 414$ and $\lambda \approx 425$ nm (**Fig. 24**-inset).

Accordingly with the literature,^[19,150] the former is associated with formation of ZnTPPS4 dimers and the latter with hybrid ZnTPPS4-PLL aggregates.

These evidences provide us a better idea about the nature of the PLL/ZnTPPS4 aggregates; in the presence of short PLLs, the prevalence of the component at $\lambda = 414$ nm indicates a higher concentration of ZnTPPS4 dimers (**Fig.24-inset**).^[19,150] On the contrary, porphyrin molecules originate a close contact with longer PLLs as reported by the higher intensity of the component at $\lambda = 426$ nm and the stronger quenching in the fluorescence spectrum than that observed in presence of short PLLs (**Fig.24-right**).

In order to get insight into possible binding mechanisms between the porphyrins and the polypeptides, spectrophotometric titrations of ZnTPPS4 with PLLs (dp 36 and 2060) were carried out.

Absorption spectra throughout the titration of a solution containing a constant concentration of ZnTPPS4 (2 μ M) by adding increasing amounts of PLL are shown in **Fig.25** (ZnTPPS4/PLLdp36-left, ZnTPPS4/PLLdp2060-right), which illustrates the progressive Soret band broadening in the ZnTPPS4 spectrum toward a limit represented by the spectra of the fully bound dye. As reported in **Fig.25**, the interaction of ZnTPPS4 with PLL dp 36 and 2060 produces an isosbestic point at 430 nm.

This progressive change is also represented by plotting the maximum of the Soret band at $\lambda=421$ nm vs. added PLL molar concentration as graphed in **Fig.26**. Since the interaction of ZnTPPS4 with PLL produces absorption variations in the Soret region, the values of ν , defined as *binding density*, and L (free porphyrin at equilibrium) necessary for the Scatchard plot were calculated with the method suggested by Peacocke and Sherrett.^[53]

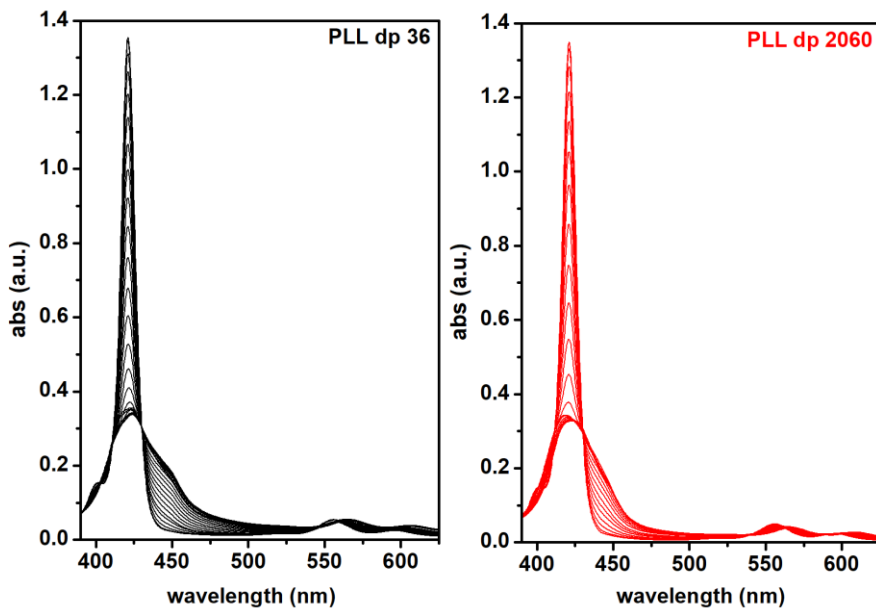


Fig.25 Absorption spectra of the titration of ZnTPPS4 ($2\mu\text{M}$) with PLL dp 36-left and PLL dp 2060-right; $0\mu\text{M} \leq [\text{PLL}] \leq 60\mu\text{M}$, $\text{pH}=7.0$, 25°C .

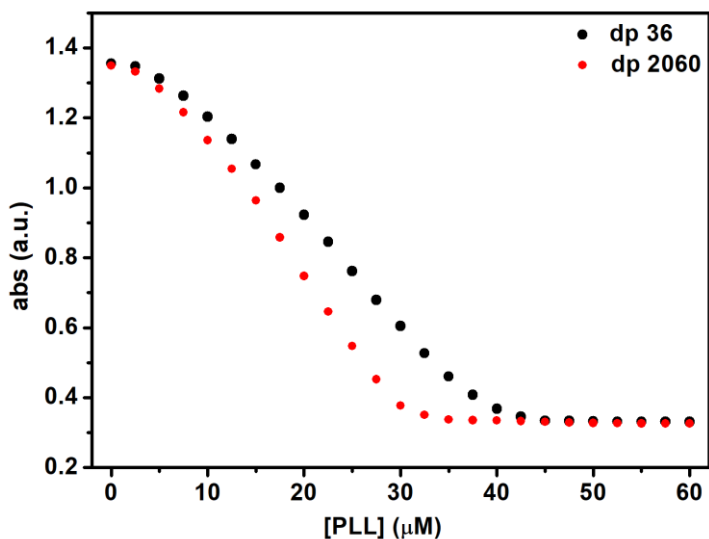


Fig.26 Spectrophotometric titration curves for the system ZnTPPS4/PLLdp36 (black dots) and ZnTPPS4/PLLdp2060 (red dots); $\lambda=421\text{nm}$, $[\text{ZnTPPS4}]=2\mu\text{M}$, $0\mu\text{M} \leq [\text{PLL}] \leq 60\mu\text{M}$, $\text{pH}=7$, 25°C .

This method requires an experimental value for the absorption of the fully bound porphyrin, Abs_b , determined by measuring the absorption at 421 nm of a solution in which the PLL concentration was 30 times greater than the initial concentration of ZnTPPS4 (i.e conditions for which complete binding may be assumed), and an experimental value for the absorption of the initial free porphyrin, Abs_f . A value of $Abs_f = 1.355$ and $Abs_b = 0.331$ for the ZnTPPS4/PLLdp36 and a value of $Abs_f = 1.349$ and $Abs_b = 0.327$ for the ZnTPPS4/PLLdp2060 (see above the first point in **Fig.26**).

The values of ν and L , calculated in accordance with ref.^[53], were employed to construct the experimental Scatchard plots reported in **Fig.27**. These plots were interpreted by using the McGhee-von Hippel approach.^[54] binding model of drugs to homogeneous one-dimensional matrix which takes into account the neighbour exclusion effects.

McGhee-von Hippel demonstrated that for the non-cooperative binding (i.e. non-interacting ligands), the Scatchard equation is of the form:

$$\frac{\nu}{L} = K_{app} (1-n\nu) \left(\frac{1-n\nu}{1-(n-1)\nu} \right)^{n-1}$$

where ν is defined in units of moles of bound porphyrin per mole of total PLL residues, L is the molar concentration of free porphyrin at equilibrium, n is the number of consecutive PLL residues covered by the binding of a single porphyrin (i.e. inaccessible to another ligand) and K_{app} is the intrinsic association constant for the porphyrin binding to a site on PLL.

Instead, when the ligands interact cooperatively, the Scatchard equation becomes more complex because it is needed to consider the co-operativity parameter ω .^[54] Noteworthy, McGhee-von Hippel attributed the Scatchard plot curvature as a consequence of cooperativity and neighbor exclusion effects.

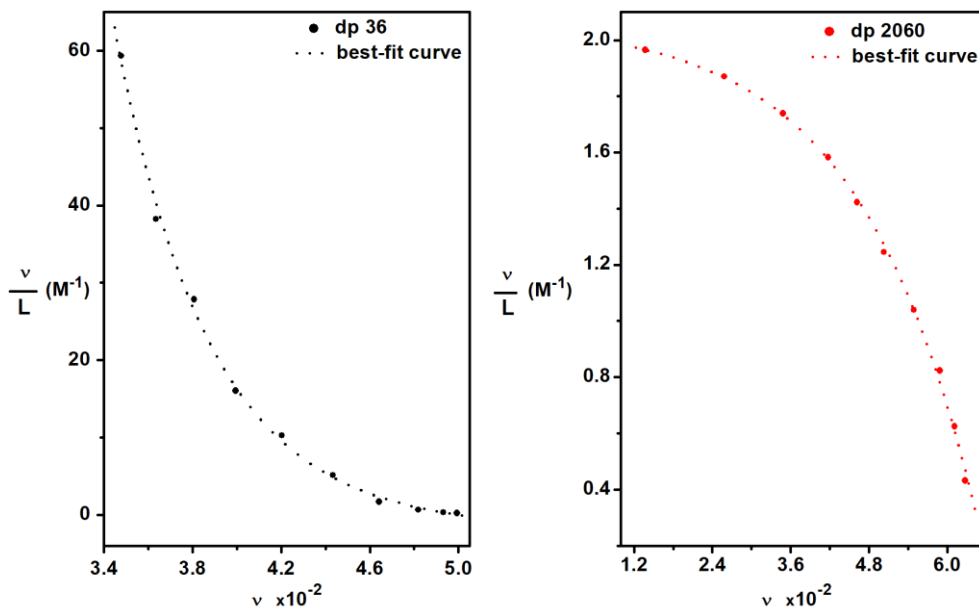


Fig.27 Scatchard plot for PLL/ZnTPPS4, dp36 (left) and dp2060 (right); $[ZnTPPS4] = 2\mu M$, $7.5\mu M < [PLL] < 30\mu M$, $25^\circ C$, $pH 7.0$.

Accordingly, the binding of ZnTPPS4 with PLL dp 36 (**Fig.27**-left) is non-cooperative. On the contrary, in the presence of a longer chain (PLL dp 2060), ZnTPPS4 is able to interact cooperatively with PLL (**Fig.27**-right). These findings may explain the different preorganization of ZnTPPS4 depending on the PLL chain length. Indeed, as shown in **Fig.24**, the presence of short PLLs promotes ZnTPPS4 dimers: the minor number of available sites mainly involves the formation of dimeric species.

Conversely, in the presence of long PLLs the combination of electrostatic and solvophobic interactions (see again **Fig.24**) suggests that once a single porphyrin binds to PLL the affinity of other sites becomes higher as in positive cooperative binding.^[152]

In addition, from the Scatchard plots reported in **Fig.27**, we were able to calculate the *apparent binding constant*, K_{app} (see below). Indeed, in a classic linear Scatchard plot the intercept on the v/L axis represents the value of the

intrinsic association constant, K_{app} . However, when the plot deviates from linearity with significant positive or negative curvatures (as in **Fig.27**), the determination of K_{app} from the intercept by extrapolation of the data is subject to large uncertainties.^[54]

Nevertheless, throughout the course of the titration, the PLL concentration (up to maximum of $60\mu\text{M}$) is greater than porphyrin concentration (fixed at $2\mu\text{M}$) thus, we can suppose that the free PLL concentration is almost equal to the total PLL concentration. Moreover, assuming that the number of consecutive PLL residues covered by a single porphyrin, n , is relatively small (i.e. reported values of 2 or 3 are most common^[153]), it may employ the equation suggested by Pasternack et al:^[153]

$$\varepsilon_p - \varepsilon_{app} = \frac{\varepsilon_{app} - \varepsilon_p}{[PLL]_{total}} \frac{1}{K_{app}} + \Delta\varepsilon$$

where ε_p is the molar extinction coefficient of the free porphyrin, ε_{app} is the absorbance of a given solution divided by the total porphyrin concentration, and $\Delta\varepsilon = \varepsilon_p - \varepsilon_b$ (in which ε_b is the molar absorptivity of the fully bound porphyrin). Thus, a plot of $\varepsilon_p - \varepsilon_{app}$ against $(\varepsilon_{app} - \varepsilon_p)/[PLL]_{total}$ leads to a linear graph of slope $1/K_{app}$ and intercept of $\Delta\varepsilon$.^[153] Such behaviour for both system, ZnTPPS4/PLLdp36 and ZnTPPS4/PLLdp2060, is shown in **Fig.28**.

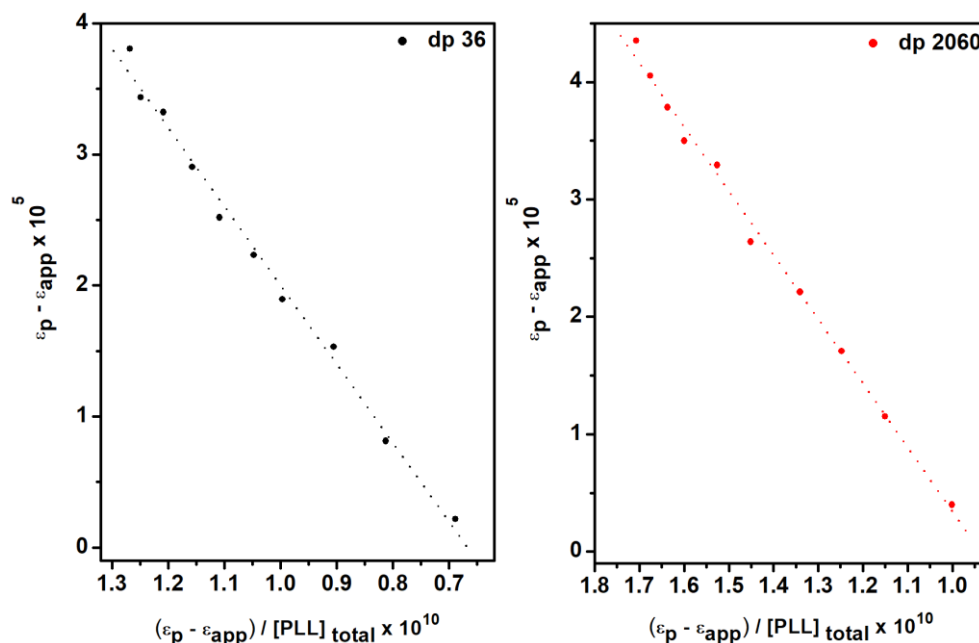
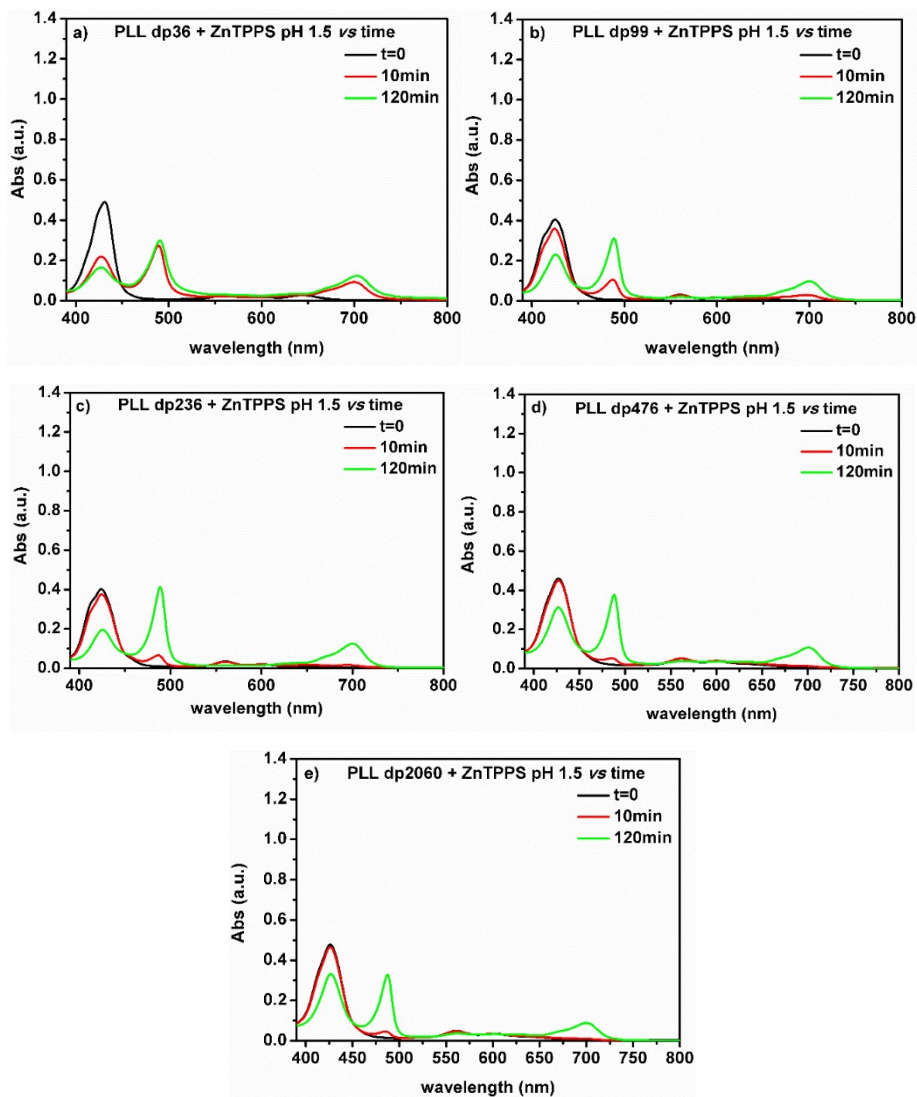


Fig.28 Binding isotherm for titration of ZnTPPS4 with poly-L-lysine dp36 (left) and dp2060 (right); $[ZnTPPS4] = 2\mu M$, $7.5\mu M < [PLL] < 30\mu M$, $pH=7.0$, $25^\circ C$.

Therefore, we have been able to obtain an estimate K_{app} for $ZnTPPS4/PLLdp36 = 1.66 \cdot 10^4 M^{-1}$ and for $ZnTPPS4/PLLdp2060 = 1.83 \cdot 10^4 M^{-1}$. These similar values are coherent with the fact that identical binding site (lysine residues) are available for ZnTPPS4 despite the different PLL chain length.

Concluded the study at neutral conditions, we wonder what happens when the HCl (up to pH 1.5) is added to the PLL/ZnTPPS4 systems.

The Uv-Vis spectra in **Figs.29** evidence a large band shape modification due to the formation of the protonated form, H_4TPPS4 ($\lambda_{max} = 434$ nm). Moreover, it is clearly evident another band at $\lambda = 490$ nm, indicating the formation of J-aggregates (see **Figs.29**).



Figs.29 Absorbance variations of $2\mu\text{M}$ ZnTPPS4 solutions at pH 1.5 ($t = 0 - 10$ min - 120 min) in presence of PLL a) dp 36 b) dp 99 c) dp 239 d) 476 e) dp 2060; $[\text{PLL}] = 50\mu\text{M}$, 25°C .

At first glance, it seems that the band intensity of the J-aggregates raises not only with the increasing time, but also with the PLL polymerization degree. This behavior is better shown in **Fig.30**, by plotting the abs at 490 nm vs time.

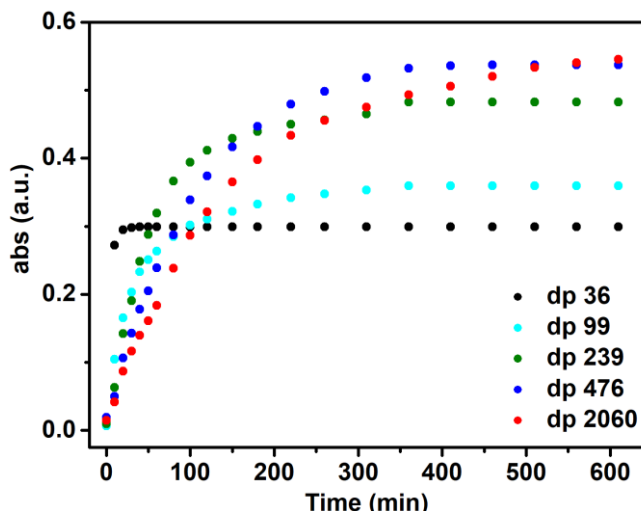


Fig.30 Absorption values of band at $\lambda = 490$ nm of ZnTPPS4/PLL solutions at pH 1.5 (PLL dp 36 black, dp 99 cyan, dp 239 green, dp 476 blue, and dp 2060 red).

The **Fig.30** displays that the kinetics of the aggregation process depend on the chain length of PLL. To make a better comparison, we calculated the rate constants by plotting the band's natural logarithm at $\lambda = 490$ nm vs. increasing time with a stopped-flow experiment (**Fig.31**).

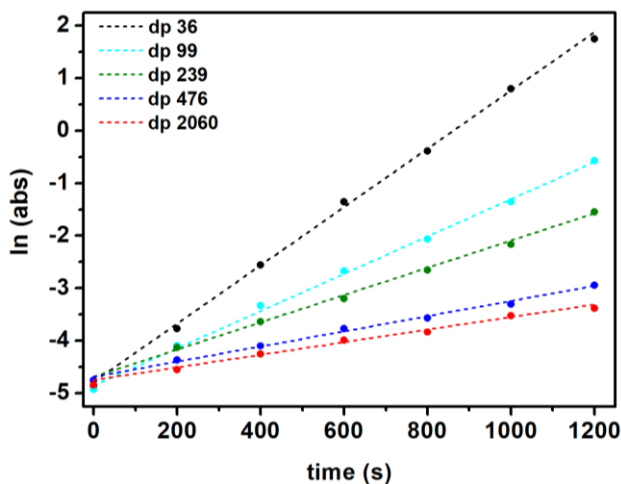


Fig.31 $\ln \text{abs}$ ($\lambda = 490\text{nm}$) vs. time of ZnTPPS4/PLL solutions at pH = 1.5 in a stopped-flow kinetic experiment (PLL dp 36 black dots, dp 99 cyan dots, dp 239 green dots, dp 476 blue dots, dp 2060 red dots); $[\text{ZnTPPS4}] = 2\mu\text{M}$, $[\text{PLL}] = 50\mu\text{M}$, 25°C .

Noteworthy, the slope of the best linear fit of each curve in **Fig.31** (multicolored dashed lines) defines a first-order rate constant.

An instantaneous formation of J-aggregates ($K_{dp36} = 5.55 \cdot 10^{-3} \text{ s}^{-1}$) is spectroscopically revealed with the shortest PLL (dp 36). On the contrary, the presence of longer PLLs (from dp=99 (cyan) to dp=2060 (red)) leads to a slower formation of J-aggregates ($K_{dp99} = 3.55 \cdot 10^{-3} \text{ s}^{-1}$; $K_{dp239} = 2.59 \cdot 10^{-3} \text{ s}^{-1}$; $K_{dp476} = 1.44 \cdot 10^{-3} \text{ s}^{-1}$; $K_{dp2060} = 1.20 \cdot 10^{-3} \text{ s}^{-1}$) resulting in a more intense band at $\lambda = 490 \text{ nm}$ whose intensity reaches a maximum value over a longer time frame. Such behaviour with long polypeptides confirms a superior degree of organization of J-aggregates formed on the longest PLL. This is also validated by the presence of a narrower (FWHM of 27 nm and 15.5 nm for ZnTPPS4/PLLdp36 and ZnTPPS4/ PLLdp2060 respectively), and intense UV-Vis absorption band at $\lambda = 490 \text{ nm}$, than that recorded for short PLL (**Fig.32**).

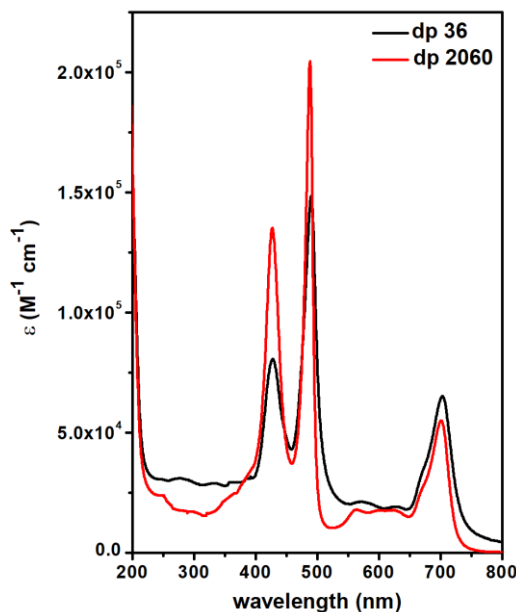


Fig.32 UV-Vis spectra of ZnTPPS4/PLL solutions (dp=36 black and dp=2060 red) at pH 1.5 after 3 h.

Furthermore, we performed resonance light scattering (RLS) measurements in order to speculate on the nature of these porphyrin aggregates (**Fig.33**).

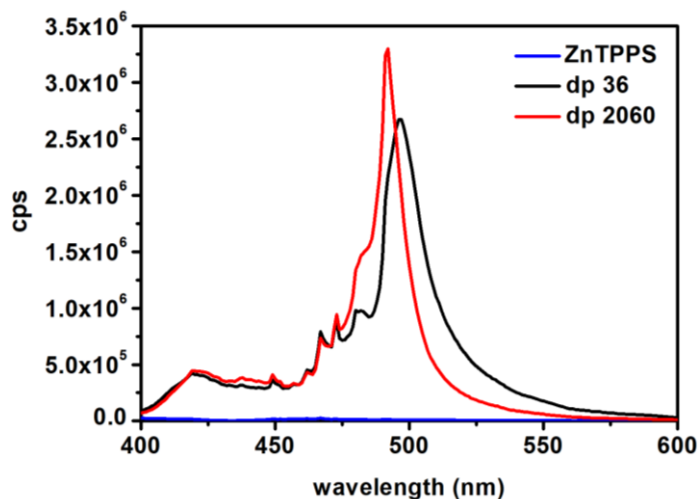


Fig.33 RLS spectra of bare ZnTPPS4 (blue curve) and in presence of PLL dp 36 (black curve) or PLL dp 2060 (red curve) at pH 1.5 after 3h; [ZnTPPS4] = 2 μ M, [PLL] = 50 μ M, 25°C.

The RLS amplitude is associated with excitonic coupling between monomeric species assembled on the template and, hence, it is related to the size and organization of the aggregates (see also *Appendix - Resonance light scattering spectroscopy*). At neutral pH, the different preorganization modes of ZnTPPS4 along the entire PLL length sets up the subsequent self-aggregation, which occurs as soon as demetallation of core is initiated. At pH 1.5 a negligible RLS signal, related to bare ZnTPPS4 (in the spectral region from $\lambda = 475$ nm to $\lambda = 500$ nm), is observed because of the absence of J-aggregates (see above **Fig.33** blue solid line).

Conversely, the RLS signal of J-aggregates templated onto the longest PLL (dp 2060) is more intense than those aggregated onto the shortest PLL. Notably,

these data agree with UV-Vis spectral evolution of porphyrin solutions in the presence of PLL.

Finally, Circular Dichroism (CD) allows specific study on the effect of PLL length on the degree of organization of the J-aggregates. Although at pH 7 the appearance of an induced CD band in the porphyrin Soret region is observed, for either short or long PLL, its intensity reveals a lower dimeric species concentration, as shown in **Fig.34**.^[19,150]

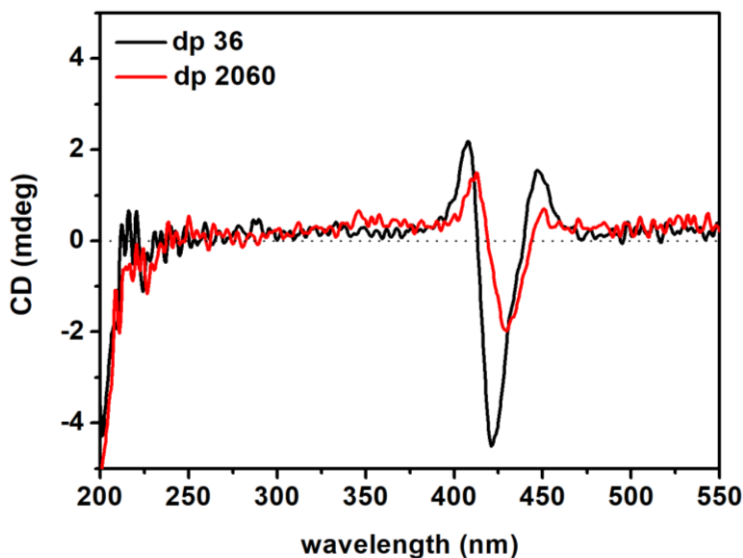


Fig.34 CD spectra of ZnTPPS4/PLL solutions ($dp = 36$ black curves and $dp = 2060$ red curves) at pH 7; $[ZnTPPS4] = 2\mu M$, $[PLL] = 50\mu M$, $25^\circ C$.

At pH 1.5, the induced CD signal drastically changes, independent of PLL chain length, and it is replaced with the CD signal of J-aggregates, as shown in **Fig.35**.

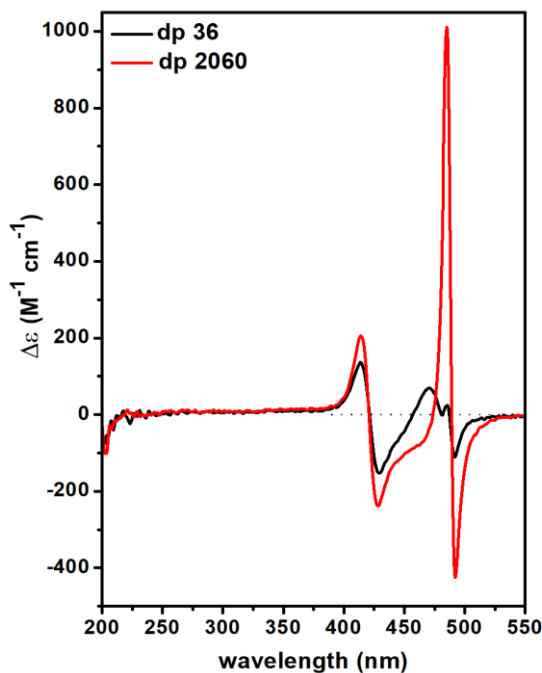


Fig.35 CD spectra of ZnTPPS4/PLL solutions (*dp*=36 black and *dp*=2060 red) at pH 1.5 after 3 h.

After 3 hours, the CD signal related to J-aggregated templated on the longest PLL is remarkably more intense than the one observed in presence of the shorter PLL. This evidence further confirms the structural evolution of the supramolecular J-aggregates into ordered structures when a long polypeptide is employed.

3.3

Final Remarks

In conclusion, the demetallation of ZnTPPS4 can be observed at $\text{pH} < 4.5$, becoming more remarkable at $\text{pH} = 1.5$. Nevertheless, at acid pH elimination of central zinc from macrocycle core results in the formation of the protonated form H_4TPPS_4 . However, the presence of poly-L-lysine in the same solution makes less accessible the metal core of the porphyrin, causing a slower demetallation process. Moreover, the templating action of PLL leads to porphyrins immobilization and screening effect towards reciprocal repulsion of the negative tails, thus catalyzing formation of J-aggregates.

In addition, we have demonstrated the possibility of controlling the demetallation/protonation process and the following *J*-aggregation process by varying degree of polymerization of PLL: *a*) if short PLLs are used, the fast demetallation/protonation of ZnTPPS4 drives the rapid formation of several families of less organized *J*-agg, made up of few monomers; *b*) longer PLLs promote structural reorganizations of the protonated porphyrins leading to the formation of long ordered *J*-agg, resulting as well, in a chirality enhancement.

4.1

Supramolecular porphyrin-calix[4]arene complexes : State-of-the-art

The non-covalent syntheses of porphyrin arrays based on polypeptide templates lacks in a significant limitation concerning the undefined stoichiometry and sequence of porphyrin assemblies – that is, the strict control of the self-assembly remains unresolved.

Hence, in 1994 *M. C. Drain* and *J.-M. Lehn* published an innovative work by presenting a quick, one-pot non-covalent synthesis (*in organic solvent*) of various porphyrin arrays, from dimers to tetramers, with controlled stoichiometry and geometry.^[154] The control over the geometry of the arrays was achieved by exploiting the kinetically inert complexation of platinum and palladium with the pyridyl moieties of the meso-substituted phenyl–pyridyl porphyrins. Noteworthy, the relevant achievement of this approach is that the yield of these syntheses is very close to 100%. This paper paved the way to the syntheses of porphyrin arrays mediated by the metal ions coordination.

Nowadays, another intriguing approach, typical of the supramolecular chemistry vision, is the host-guest chemistry.^[39,40,42,64] Here, the host molecule takes the place of the metal ion and contributes, as well, to the structural and electronic features of the resulting complexes. A good example of binary host–guest species is given by *porphyrin–cyclodextrin* (guest and host, respectively) complexes. Originally these “*simple*” porphyrin complexes were synthesized to mimic the enzyme in Nature, such as to reproduce the activity of the heme-protein of myoglobin in aqueous environment.^[155]

The feasibility of synthesizing stable complexes in aqueous solution -in terms of thermodynamic and kinetic points of view- is an intrinsic property of the host-guest chemistry which can also employ water-soluble and solvophobic molecular components at the same time. In fact, following a careful molecular and supramolecular design, the dichotomic nature of the components drives spontaneous self-assembly mainly leading from hydrophobic interactions.^[155] Therefore, the synthesis of discrete large supramolecular complex structure in water requires a strict control of the undesired (self-) aggregation phenomena governed by electrostatic interactions between net charges in combination with π - π and all the other weak interactions.

In this respect, a class of promising molecules able to template discrete porphyrin arrays in aqueous solution is undoubtedly represented by calixarenes. Calixarenes –defined by Cram and Steinberg^[156,157] as $[1_n]$ metacyclophanes, with $n \geq 4$ - are macrocyclic hosts synthesised by the condensation reaction between a *p*-substituted phenol and formaldehyde. The origin of calixarenes dates back to 1940s, when Zinke and Ziegler, as part of their study of the Bakelite process, decided to simplify the reaction by examination of the condensation of *p*-substituted phenols, particularly, *p*-*t*-butylphenol with formaldehyde (**Fig.36**).^[158] Unexpectedly, a crystalline product of empirical formula $C_{11}H_{14}O$ was isolated. Since the substituted phenol can only react at the ortho position (the hydroxyl group is ortho and para directing) and based on current literature, they hypothesized a cyclic tetrameric structure. Further evidence for a tetrameric structure came by Hayes, Hunter, and later by Cornforth in 1956.^[159] Since 1970s, Gutsche optimized conditions for their syntheses and coined the name “calixarene” in 1975.^[40,42,64] The name is derived from the Greek *calix* meaning “vase” or “chalice; instead *arene* indicates the presence of aryl residues in the macrocyclic array. The name, initially considered unacceptable by IUPAC and

4.1 Supramolecular porphyrin-calix[4]arene complexes: State-of-the-Art

Chemical Abstracts, gained official status and has now been expanded to include any number of other kinds of structures that bear a general resemblance to the phenol-derived calixarenes.^[64]

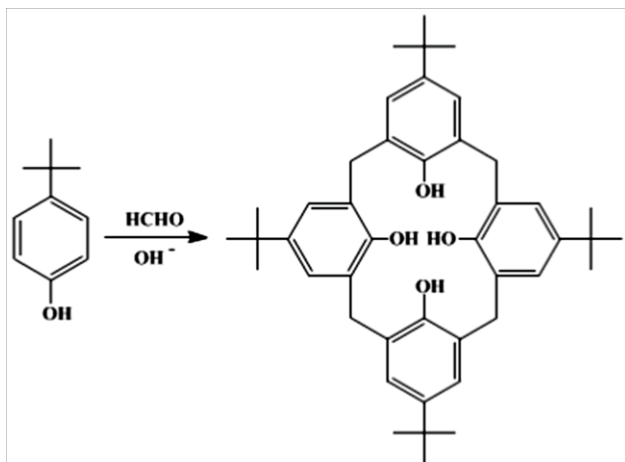


Fig.36 Conventional synthesis of *para*-*t*-butylcalix[4]arene.

The calixarene framework is very versatile and many derivatives have been prepared by functionalising the groups on the ‘*upper*’ rim -or *exo*-face- and ‘*lower*’ rim-or *endo*-face- (the upper rim is where the *t*-butyl substituents are located, while the hydroxyl groups are on the lower rim), **Fig.37**.

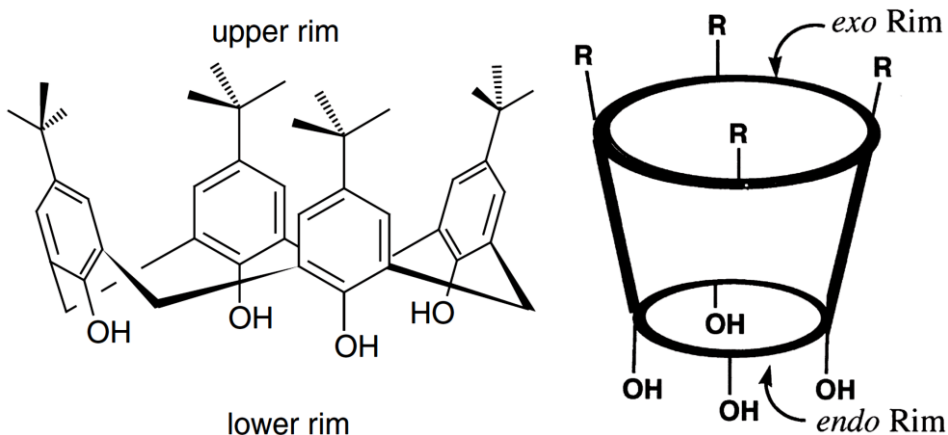


Fig.37 3D structure of *p-t-butylcalix[4]arene* with its upper and lower rim.

For most calixarenes the complete nomenclature comprises a prefix, denoting the upper rim substituents, followed by calix[*n*]arene where *n* is the number of aryl units in the cyclic compound. A suffix, describing the lower or up rim substituents, may also be given. Therefore, the correct nomenclature for para-*t*-butylcalax[4]arene (see above **Fig.37**-left) is 15,11,17,23-tetra-*tert*-butylcalix[4]arene-25,26,29,28-tetrol.

The calixarenes are flexible during their high temperature synthesis, because of rotation of their phenolic moieties through the bridging CH₂ groups. This is an important consideration when working with calix[4]arenes, in fact they can exist in four conformers that are hard to interconvert (also at high temperature) and become immobilized in a particular conformer if lower rim is functionalised by substituents.^[64,160] Four principal conformers are observed at room temperature. If all four upper rim substituents are in the same orientation, thus a *cone conformer* is expected. If one phenolic group is inverted with respect to the others, a *partial cone conformer* is found. Finally, two possibilities exist

when two phenol rings are inverted: 1,2 alternate and 1,3 alternate. All four conformers are illustrated in **Fig.38**.

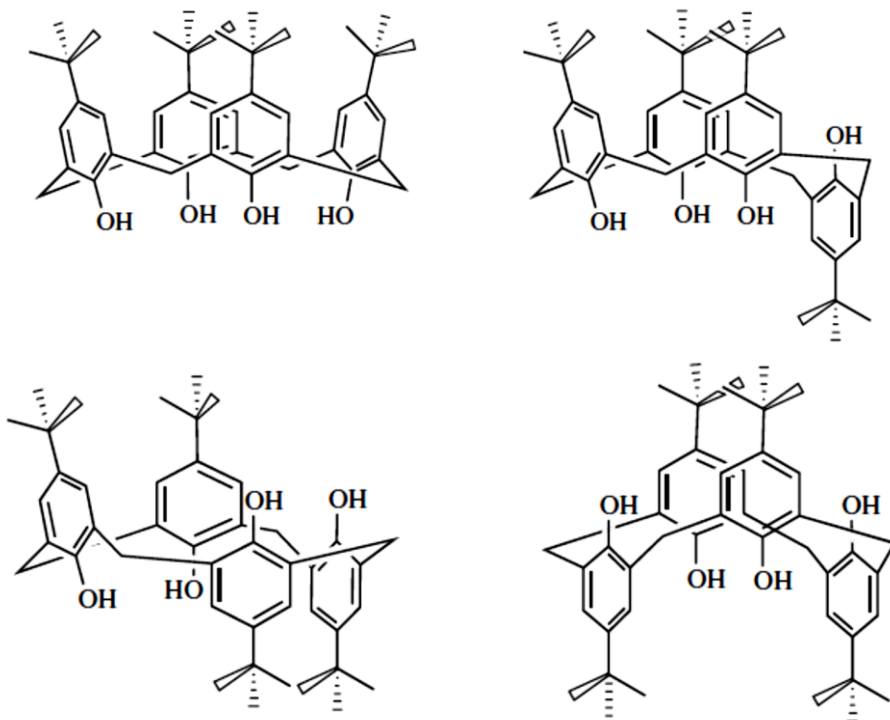


Fig.38 Calix[4]arene conformers: cone (top left), partial cone (top right), 1,2-alternate (bottom left), 1,3-alternate (bottom right).

Due to their structure characterized by the hydrophobic *chalice*, calix[n]arenes are able to host specifically functionalized molecules, belong to the class of cavitands known in host–guest chemistry. The possibility to design and tailor the hosts chemistry and structure in order to promote more efficient interactions (mainly CH– π , π – π and π –cation, hydrogen bonding) with the guest porphyrins makes these templates extremely versatile building blocks for supramolecular architectures. Among *water-soluble calixarenes*, *p-sulfonate-derivatives* have been widely studied because their host–guest complexes can

mimic biologically relevant molecules, but also because their potential applications span from pharmacology to crystal engineering.^[161–167]

Owing to their π cavities and the anionic sulfonate groups of the upper rim,[†] *p*-sulfonate-calixarenes are excellent hosts for cationic and neutral molecules.^[164] In this regard, cationic porphyrins can represent interesting counterparts, and as well, calixarene–porphyrin supramolecular complexes have indeed been studied for various purposes.^[16,162]

Hence, *Di Costanzo et al.*, in the early 2000s demonstrated that the *p*-sulfonate-calix[4]arene, bearing four carboxylic groups in the lower rim, *C₄TsTc* (see **Fig.39**), is able to complex the cationic meso-tetrakis(4-*N*-methylpyridyl)-porphyrin, *H₂T4*, resulting in a stable, tunable and stoichiometric complex.^[168]

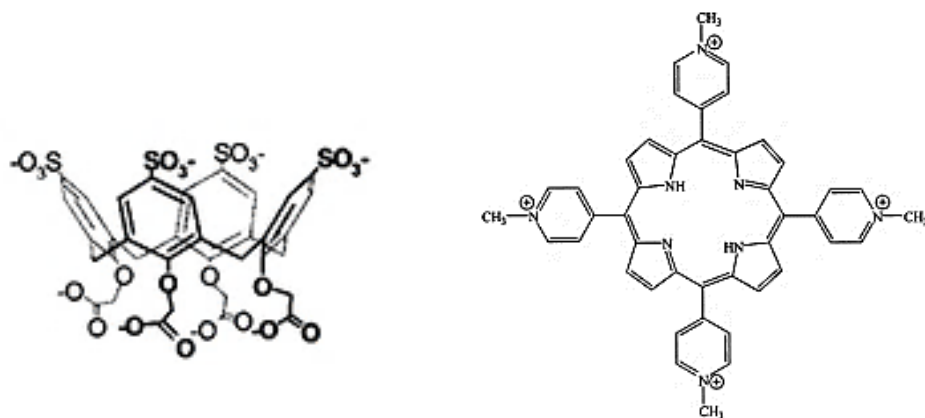


Fig.39 molecular structure of *C₄TsTc* (left) and *H₂T4*(right).

The interaction of *H₂T4* with *C₄TsTc* in aqueous solution (at pH 6 and 2.2) is accompanied by significant hypochromism and broadening of the Soret band (422 nm, see inset of **Fig.40**). The system was characterized in aqueous solution

[†] Other functionalities can also be introduced into the lower rim

by monitoring the absorbance at 422 nm at different ratio $C_4TsTc:H_2T4$ in order to trace the *Job plot* in **Fig.40**.

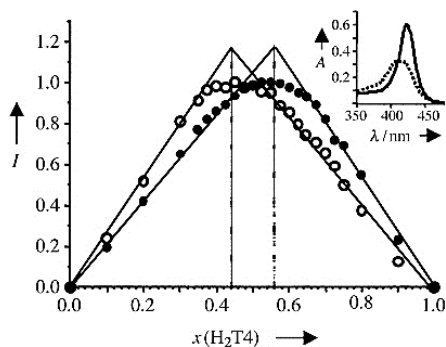


Fig.40 Normalized absorption Job plots at pH 2.2 and 6. The inset shows the absorption spectrum of H_2T4 ($2.8 \mu M$) before (continuous line) and after (dotted line) the addition of C_4TsTc ($2.2 \mu M$).

However, due to different protonation steps of the tetra carboxylic groups of the C_4TsTc , the Job plots performed at pH 2.2 and 6 show there is a large difference in the ratio of the complex formed (**Fig.40** above). The maximum value at a porphyrin molar fraction of 0.44 at pH 2.2 indicates the formation of species with a 4:3 ($C_4TsTc:H_2T4$) ratio, whereas the maximum value at a porphyrin molar fraction of 0.56 at pH 6 indicates the formation of species with a 4:5 ($C_4TsTc:H_2T4$) ratio. Moreover, X-ray analysis showed that two or four porphyrins (for the 4:3 and 4:5 species, respectively) pile up above and below the plane of a 1:4 ($H_2T4:C_4TsTc$) central core (**Fig.41**). Here, each of the four meso-cationic groups of H_2T4 interacts with the major rim (upper rim) of one calixarene.^[168] Despite its relevance as unit cell in crystalline structure, the first stoichiometric complex, 1:4 ($H_2T4:C_4TsTc$) is not clearly evidenced in the Job plot experiment.

4.1 Supramolecular porphyrin-calix[4]arene complexes: State-of-the-Art

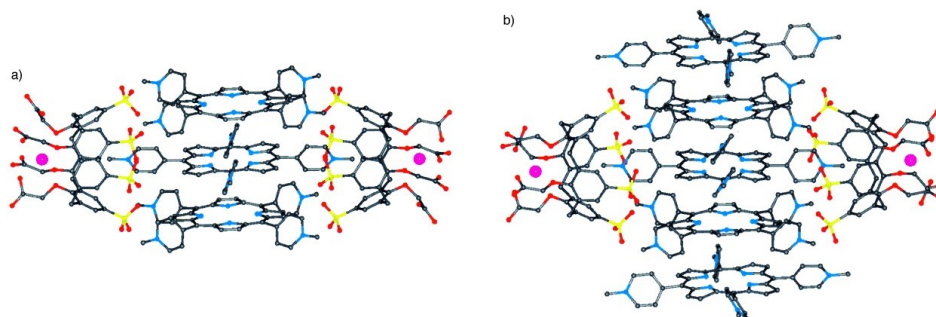


Fig.41 3D side views of the supramolecular complexes with ratio (a) 4:3 ($C_4TsTc:H_2T4$) and (b) 4:5 ($C_4TsTc:H_2T4$).

One possible explanation is that the Job plot method, by promoting the formation of complex thermodynamically more stable with higher stoichiometry, is not the best analytical approach to study and analyze this system. On the contrary, the stepwise titration of a solution containing C_4TsTc with H_2T4 lead to a titration curve characterized by the presence of various and distinct break-points, evidencing not only the formation of the expected 3:4 and 5:4 species, but also the 1:4, 6:4 and 7:4 complexes (**Fig.42**).^[169]

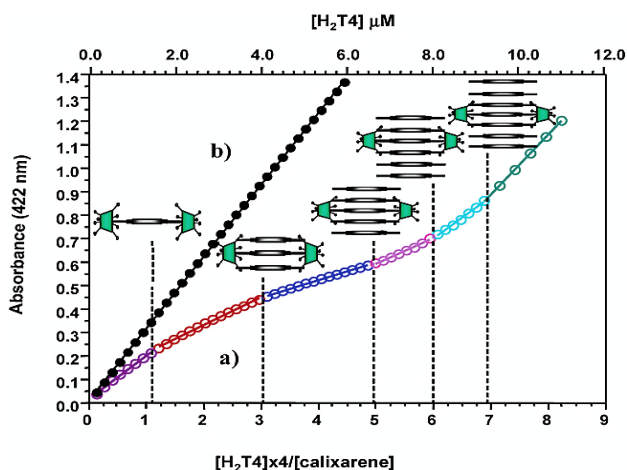


Fig.42 Soret band intensity following addition of increasing amounts of H_2T4 to a calixarene aqueous solution (curve a) and pure water (curve b). The different break-points (curve a) are evidenced by dotted lines, and the corresponding species. For the sake of clarity the two calixarenes above and below the reading plane have been omitted.

The presence of well-defined *break-points* and different slopes, at least 15% of variation, suggests the assembly of discrete species per step. Indeed, the slope in a titration plot as in **Fig.42** corresponds to a molar extinction coefficient, which in turn, depends on the chemical-physical properties of the compound. Therefore, any break-point in the titration represents the end-point for the formation of one complex and the starting point of the next one, not in equilibrium each other. Moreover, the stability and kinetic inertness of these supramolecular complex was further confirmed by diffusion NMR data^[47] and dynamic light-scattering experiments.^[170]

These aspects together with hierarchical rules are of fundamental relevance because they allow for designing and realizing mixed metallo-porphyrin hetero-aggregates having a pre-determined porphyrin sequence,^[169] as shown in spectrofluorimetric titrations[†] of **Fig.43**.

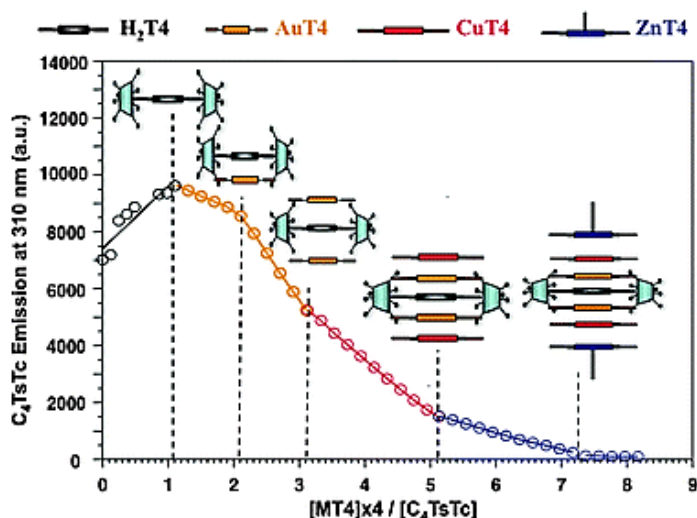


Fig.43 Fluorescence variation of C4TsTc following the titration of a calixarene solution (2.5 μ M) against increasing amounts of different porphyrins schematically presented at the top of the figure

[†] Here, the emission of calixarene was used in order to avoid the spectral interferences due to similar porphyrins' Soret bands

The degree of complexity was further reached by using the permanent cationic ditopic calixarene, 1,6-bis[5,11,17,23-tetrakis (trimethylammoniomethyl)-25,26,27-tripropoxy-28-(oxy) calix[4]arene] hexane octachloride, namely bis-calix[4]arene or **BC4** and the anionic porphyrin, Cu(II) meso-tetrakis(4-sulfonatephenyl)porphyrin tetrasodium salt, that is **CuTPPS4** (see **Fig.44** for their molecular structures).

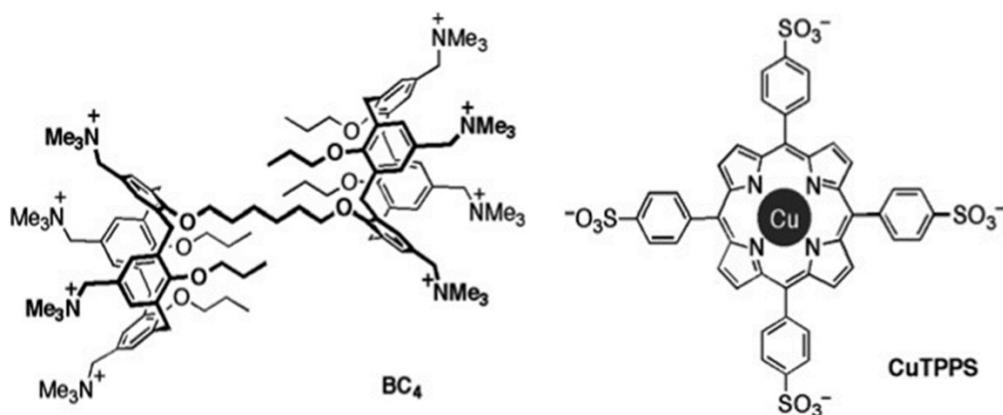


Fig.44 Molecular structure of *BC4* (on the left) and *CuTPPS4* (on the right)

The spectrophotometric titration (data not shown) of solutions containing **BC4** with **CuTPPS4** showed very clear breakpoints indicating the stepwise formation of discrete species, in which the complex with 1:4 (**CuTPPS4**:**BC4**) ratio is a founding element (see the 1:4 complex in **Fig.45** on the left).^[170] Notably, the formation of this complex is initially driven by electrostatic interactions but, once the 1:4 core is formed, hydrophobic interactions play a very important role in its stabilisation.

The careful comparison between the **Figs.41** and **45** elucidate the main difference in using mono-calixarenes, **C4TcTs**, or bis-calixarenes, **BC4**. The monotopic host allows for piling up to seven porphyrins above and below the plane of the central 1:4 unit, leading to porphyrin stacks with a controlled sequence and stoichiometry. The ditopic host provides an additional opportunity

of controlling the geometry. In particular, after the 5:4 species formation (see the 5:4 complex in **Fig.45** below), there is a fork-point which can lead to stacked or planar extended species depending on the addition of porphyrins or calixarenes, respectively (**Fig.45**).^[170]

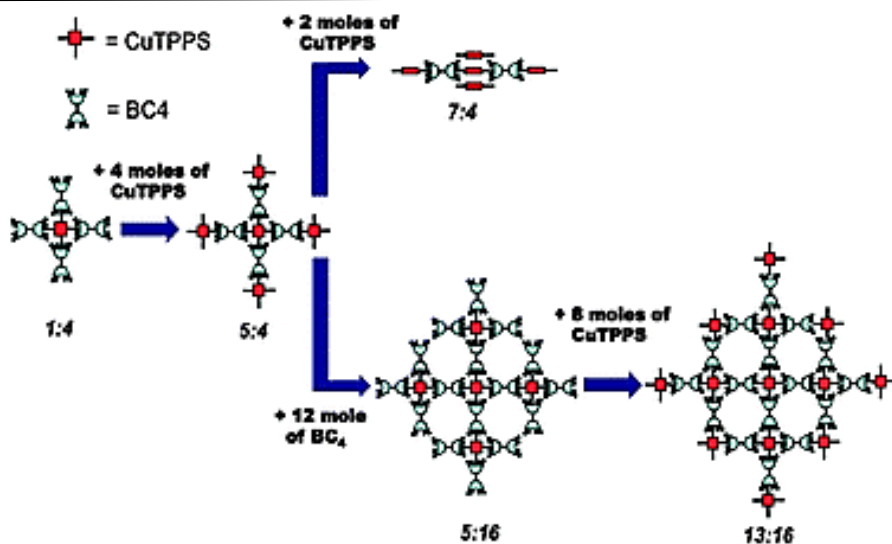


Fig.45 Schematic representation of the initial 1:4 (CuTPPS4:BC4) core (top view) and of the species subsequently formed from the 5:4 complex (top view) after addition of CuTPPS4 (7:4 species, side view) or BC4 (5:16 species, top view), respectively

To date, it has been demonstrated that the addition of porphyrins to the initial 1:4 complex perturbs the electronic properties of the central porphyrin unit. Therefore, other properties may be induced into the complexes, among them, the induction of chirality in the porphyrin–bis-calixarene systems is a fascinating perspectives. In order to achieve this purpose, a fully non-covalent approach was used as reported by Nicotra et al.^[171]

In this case, a cationic pH charge modulable bis-calixarenes, the 1,6-bis{5,11,17,23-tetra-amino-25,26,27-tripropoxy-28-[oxy]calix[4]arene}hexane, **BC4-NH2** (see **Fig.46**-top left), was used in host-guest interaction with the same anionic porphyrin, **CuTPPS4** (**Fig.44**-right).

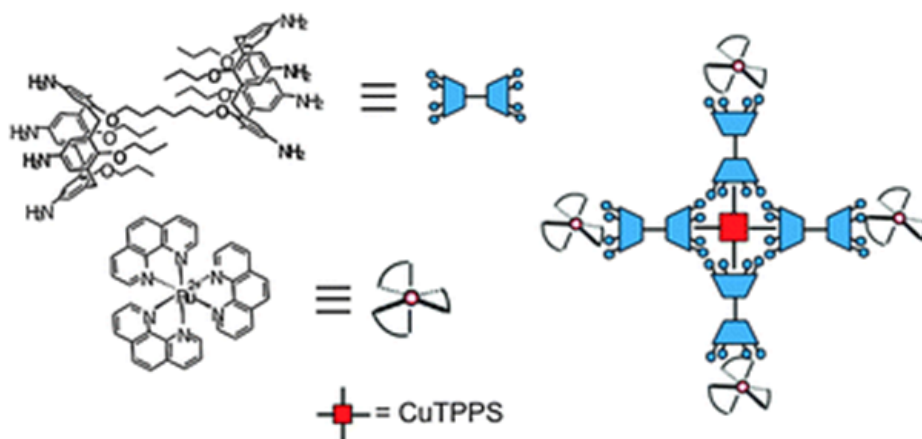


Fig.46 Structure of BC4-NH2 (top left) and asymmetric Λ - or Δ -[Ru(phen)3]²⁺ (down left). On the right is reported the schematic representation of chiral 1:4:4 (CuTPPS4:BC4-NH2:[Ru(phen)3]²⁺) complex

However, the presence of eight protonable amino-group in BC4-NH2 makes the choice of pH an essential aspect to guarantee the correct interaction with anionic CuTPPS4. According to a spectrophotometric pH titration (data not reported),^[171] BC4-NH2 undergoes protonation in two separate steps (pK_a values of 4.5 and 7.0, respectively), quite likely indicating the involvement of two amino groups for each calixarene subunit (i.e. a total of four protons per step). Reasonably, at pH 5.5 BC4-NH2 is tetracationic (two positive charges for each subunit) allowing for the complexation with CuTPPS4. In the light of these considerations, attention was taken in adding 1 μ M of CuTPPS to a 4 μ M aqueous solution of BC4-NH2 at pH 5.5. Formation of the 1:4 (CuTPPS4:BC4-NH2) species is indicated by a 40% hypochromism and a red-shift of the Soret band (compared the black trace with the blue trace in **Fig.47**).

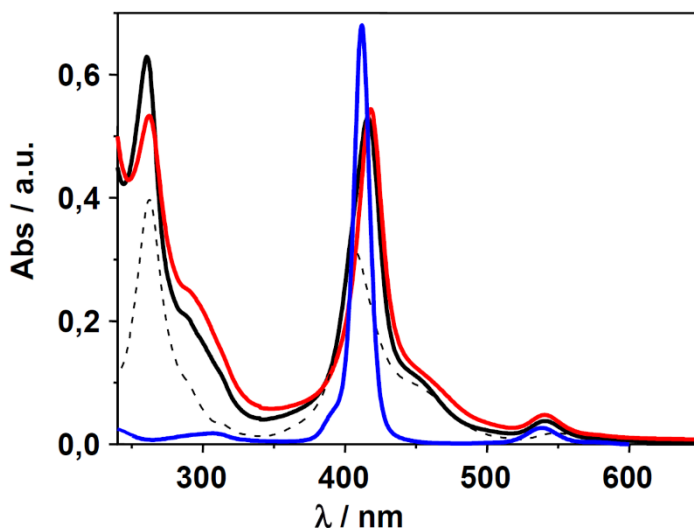


Fig.47 Absorption spectra of aqueous solutions of the ternary 1:4:4 assembly ($[CuTPPS]=1.5 \mu M$, $BC4-NH_2=6 \mu M$, $[\Delta-[Ru(phen)_3]^{2+}]=6 \mu M$) at pH 5.5 (black trace) and pH 9.0 (red trace). The dashed trace refers to an aqueous solution of the binary 1:4 complex $CuTPPS/\Delta-[Ru(phen)_3]^{2+}$ (1.5 and $6 \mu M$, respectively) at pH 9.0, while the blue one pertains to $CuTPPS$ (1.5 μM) at pH 9.0.

At this step, 4 moles of cationic Δ or Λ enantiomer of ruthenium phenanthroline, $[Ru(phen)_3]^{2+}$ (see above **Fig.46** down left) were added to preformed 1:4 ($CuTPPS_4:BC4-NH_2$) complex in order to induce chirality.

Despite of the positive charges in the $[Ru(phen)_3]^{2+}$, at pH 5.5 the $BC4-NH_2$ is not too cationic to prevent the formation of 1:4:4 ($CuTPPS_4:BC4-NH_2:[Ru(phen)_3]^{2+}$) species (see the structure in **Fig.46** on the right). In fact an induced CD signal appears in the $CuTPPS_4$'s Soret region as shown in inset of **Fig.48** below (see also the black trace in previous **Fig.47** for UV/Vis spectrum).

Quite surprisingly, this latter complex persists even after the pH of the solution is raised to 9.0: in other words, under experimental conditions where $BC4-NH_2$ was found to exist as the fully unprotonated octa-amino derivative (compare the black trace and red trace in **Fig.47** above).

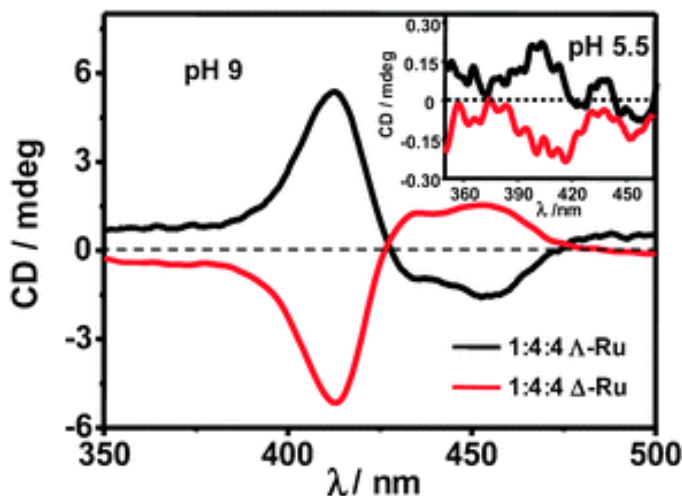


Fig.48 CD spectra of the ternary 1:4:4 (CuTPPS4:BC4-NH2:Λ-[Ru(phen)3]²⁺) at pH 9.0 in black trace, and 1:4:4 (CuTPPS4:BC4-NH2:Δ-[Ru(phen)3]²⁺) at pH 9.0 in red trace. in. The inset shows the CD spectra of the same solutions at pH 5.5.

Such evidence further highlights the role played by dispersive and hydrophobic forces to stabilize the complex. Nevertheless, the increase of pH from 5.5 to 9 provokes, as well, the many-fold higher intensity of the ICD (see **Fig.48** above) as a result of a stronger interaction between BC4-NH2 and [Ru(phen)₃]²⁺ (owing to reduction of cationic charges in BC4-NH2).^[171] Noteworthy, a mirror-image ICD signal of comparable intensity is conversely observed in the case of the opposite enantiomer.

4.2

Results and Discussions

4.2.1 Towards porphyrin/calix 1D assemblies:

- **H₂DPPS3/BC4 and CuDPPS3/*chiral*-BC4-NH₂ complexes**

A further step toward a more exhaustive comprehension about the abovementioned self-assembly processes involves the employment of new molecular building blocks. In this regard, a one-dimension (1D) porphyrin-calix[4]arene complexes, in which the electronic and optical properties may transfer along a continue line (1D), is an intriguing goal.

The use of a ditopic bis-calix[4]arene together a *trans*-bis-substituted porphyrin could offer an interesting approach to assemble one-dimension architectures. Our choice falls on: *i*) a novel anionic synthetic porphyrin, the *5,15-meso-bis(4-sulfonatophenyl)-2-sulfonato porphyrin*, **H₂DPPS3 (Fig.49a)**, and his copper (II) derivative, **CuDPPS3 (Fig.49a)** *ii*) the cationic, **BC4 (Fig.44-left)**, *iii*) chiral bis-calix[4]arenes, namely **(SS)-BC4-NH₂** and **(RR)-BC4-NH₂ (Fig.49b)**.

The H₂DPPS3, is a novel anionic porphyrin with two sulfonatophenyl substituent in *trans*-meso-positions and one sulfonate group directly bonded to the porphyrin ring.

4.2.1 Towards porphyrin/calix 1D assemblies:
H₂DPPS3/BC4 and CuDPPS3/chiral-BC4-NH₂ complexes

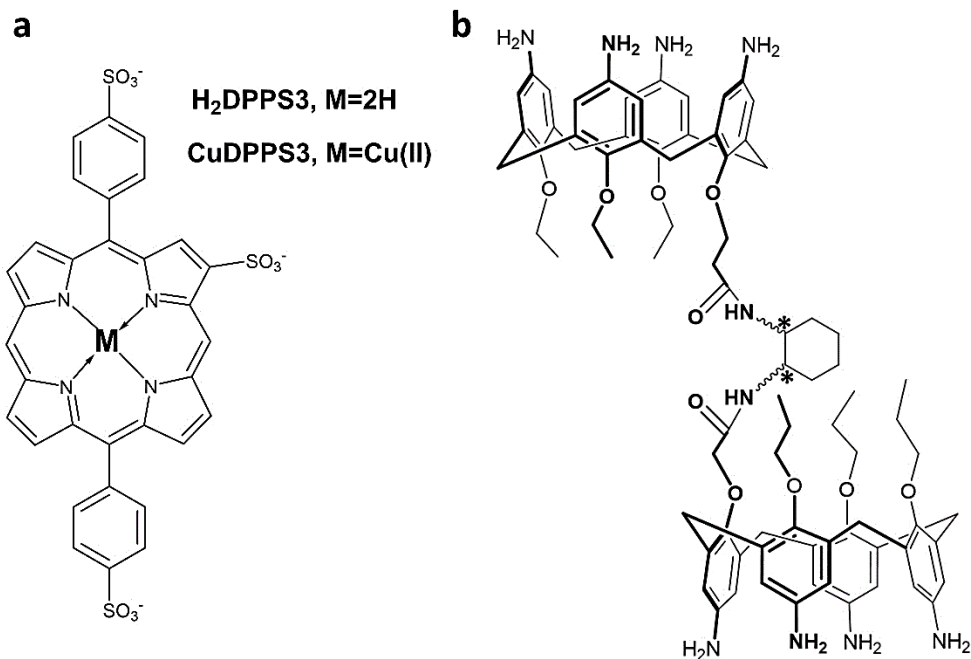


Fig.4.9 Molecular structure of a) H₂DPPS3 and CuDPPS3 b) SS- or RR- BC4-NH₂.

Aqueous solutions (pH = 10) of H₂DPPS3 ($\epsilon_{405,5}/\text{H}_2\text{O} = 1.136 \cdot 10^5 \text{ cm M}^{-1}$) display an intense *Soret* band at 405,5 nm and four *Q* band at 507 nm, 543 nm, 572 nm and 624 nm (**Fig.50**).

Nevertheless, in acid condition (pH = 1.5) the core protonation occurs, consequently a red-shift at is observed at 420 nm with only two *Q* band at 570 nm and 614 nm (**Fig.50**-inset).

4.2.1 Towards porphyrin/calix 1D assemblies:
H₂DPPS3/BC4 and CuDPPS3/chiral-BC4-NH₂ complexes

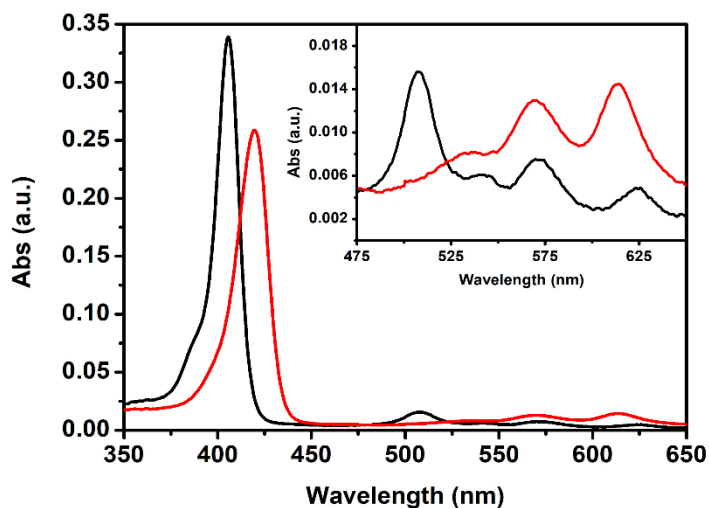


Fig 50 Absorbance of an aqueous solution of H₂DPPS3 (3 μM, pH 10.0 black line) and of H₂DPPS3 (3 μM, pH 1.5 red line); in inset are reported in detail the Q-bands' region.

The first experiment was performed recording UV-vis (**Fig.51**) spectra of different solutions of H₂DPPS3 2 μM prepared at different pH values (from 10.30 to 0.43), in order to get information of protonation equilibria and obtain pK_a values of H₂DPPS3 in aqueous solution, minimizing the effect of aggregation (*independent solutions experiment*).

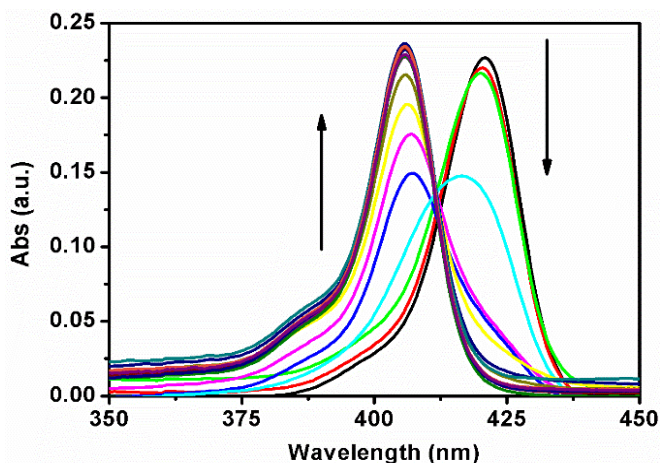


Fig 51 Absorption spectra of independent solutions of H₂DPPS3 2 μM at different pH.

The absorption spectra performed by independent solutions of H₂DPPS3 at different pH (**Fig.51**) show a classical shape of porphyrin core-protonation curve: going down the pH of the solutions, the band at 405.5 nm, related to deprotonated H₂DPPS3, decreases in intensity, giving way to a new band at 420 nm indicating the formation of core protonated H₂DPPS3. Reporting the absorbance values at 405.5 nm and 420 nm vs. the pH of each solution, it is possible to evaluate the pK_a values of the H₂DPPS3 (**Fig.52**). Indeed, we can denote only one protonation step related to the protonation of the nitrogen core atoms, that is pK_a ~ 2.80.

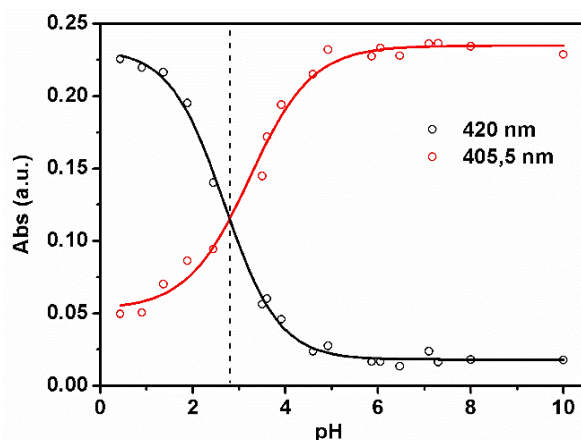


Fig 52 Absorbance ($\lambda = 405.5 \text{ nm}$) vs. pH for independent solutions of H₂DPPS3 (2 μM).

Then, a slow titration of a solution of H₂DPPS3 2 μM decreasing the pH (from 10.31 to 2.44) was carried out to investigate the self-assembly processes (titration experiment, **Fig.53**). As shown in **Fig.53**, during the titration the absorption band of the deprotonated porphyrin (405.5 nm) decreases in intensity and broadens. Noteworthy, in this experiment the intensity of absorption band of the protonated H₂DPPS3 (420 nm) is not higher than the band observed in the case of independent solutions experiment (**Fig.51**). The broadening of the band at 405.5 nm and the very low intensity of protonated band at 420 nm up to pH

2.44 can be ascribed to the formation of aggregates during the titration. As a consequence, the baseline of Uv-vis spectra tends to increase for protonated form, due to the presence of aggregates (**Fig.53**).

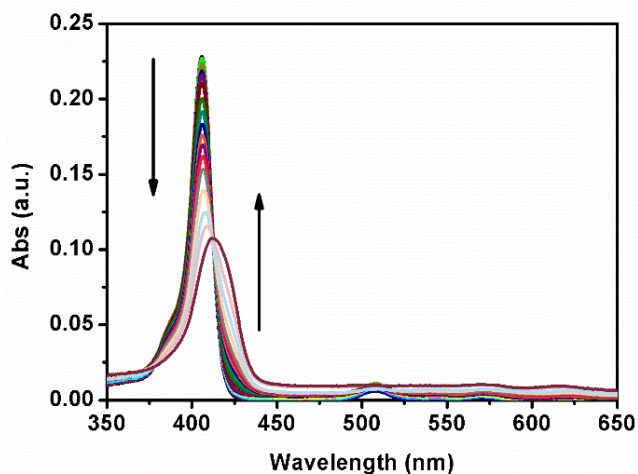


Fig 53 Absorption spectra of the pH titration of a solution 2 μM of H₂DPPS.

The BC4, is an homoditopic bis-calix[4]arene (above in **Fig.44**-left) in which the presence of octa- permanent cationic tri-methylammonium groups make it soluble in water (also in neutral pH conditions) and able to interact with anionic counterparts such as sulfonate-porphyrins. BC4 is characterized by two absorption peaks, one more intense at 270 nm and another about at 320 nm (see inset in, **Fig.54**).

To investigate the interactions between the positively charged templating agent and the tri-anionic porphyrin, we carried out a Uv-Vis titration of an aqueous solution of bis-calix[4]arene BC4 (2.5 μM) with increasing amounts (0.25 μM) of H₂DPPS3 at neutral pH. In agreement with previous studies,^[47,170] hypochromicity and broadening of the porphyrin Soret band was observed over the course of the experiment (**Fig.54**).

4.2.1 Towards porphyrin/calix 1D assemblies:
H₂DPPS3/BC4 and CuDPPS3/chiral-BC4-NH₂ complexes

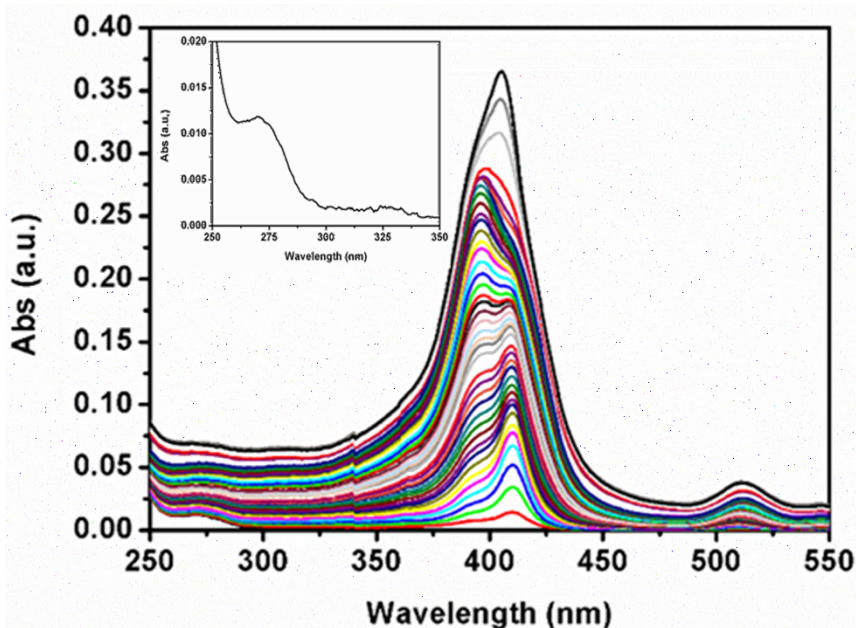


Fig.54 Uv-Vis absorption spectra recorded over the course of the titration of an aqueous solution of bis-calix[4]arene BC4 (2.5 μM) with an aqueous solution of H₂DPPS3, added stepwise (0.25 μM) to reach a final [H₂DPPS3] = 11 μM at pH 7.0. Inset: Uv-Vis spectrum of an aqueous solution of bis-calix[4]arene BC4 (2.0 μM) at pH 7.0.

The self-assembly of the porphyrins in the presence of the bis-calix[4]arene templating agent can best be analyzed and understood by plotting the variation of the absorbance at 405.5 nm versus the [H₂DPPS3] / [BC4] ratio (**Fig.55**). The black dotted line (a) refers to the absorbance of the Soret band of H₂DPPS3 in the absence of BC4. The multicolored dotted curve (b) refers to the experiment in which BC4 was titrated with porphyrin H₂DPPS3.

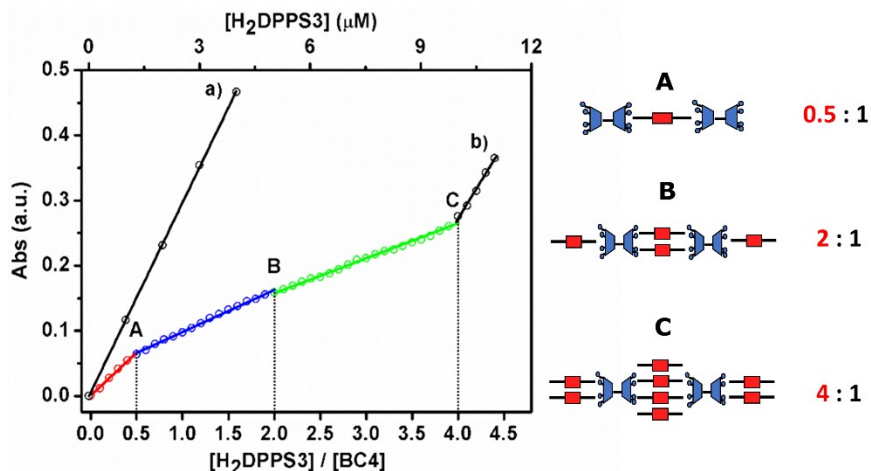


Fig.55 Variation in the absorbance of the H₂DPPS3 Soret band ($\lambda = 405,5 \text{ nm}$) observed upon: (i) increase of the porphyrin concentration in water at pH 10.0 (black trace (a)) and (ii) portion-wise addition ($0.25 \mu\text{M}$) of the porphyrin to a $2.5 \mu\text{M}$ aqueous solution of bis-calix[4]arene BC4 at pH 10.0 (trace (b)). On the right, schematic structures of the complexes are illustrated.

The latter indicates that the interaction of BC4 with H₂DPPS3 causes hypochromic effects modulated by the stoichiometry of the complex. In fact the control of complex stoichiometry is highlighted by the presence of *break-points* evidenced in **Fig.55** at ratio [porph]/[calix] 0.5:1, 2:1 and 4:1. Moreover, after addition of the fourth equiv. of porphyrin, the slope of the titration curve becomes almost identical to that detected for H₂DPPS3 on its own (black dotted line - trace (a)), indicating that the porphyrins are no longer interacting with the supramolecular complex.

The absence of break-points at ratio 1:1 and 3:1(H₂DPPS3:BC4) allows us for speculating about presence of an equilibrium between two species with same stoichiometry but difference conformation. For instance, in 1:1 complex two porphyrin could occupy the central core, or alternately, one into the core and the other one bound externally (see **Fig.56** below).

4.2.1 Towards porphyrin/calix 1D assemblies:
H₂DPPS3/BC4 and CuDPPS3/chiral-BC4-NH₂ complexes

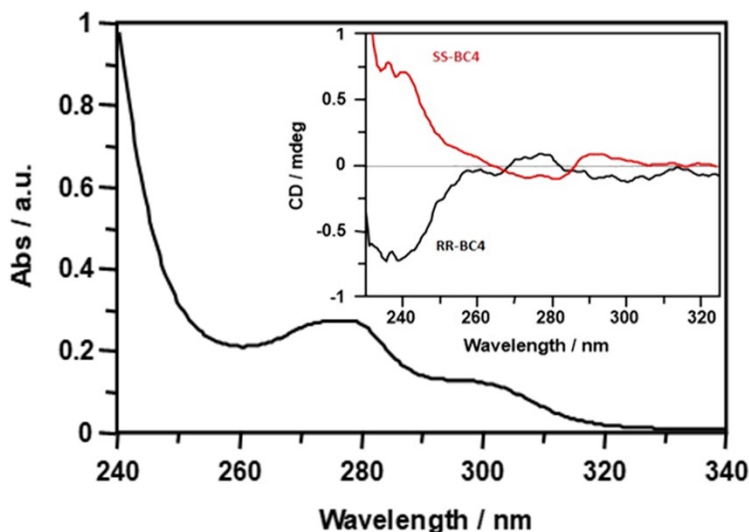


Fig.57 UV-vis spectrum of an aqueous solution of chiral bis-calix[4]arene (50.0 μM) at pH 2.0. Inset: CD spectra of the same solutions (SS-BC4-red line, RR-BC4 black line).

Unlike the analogous achiral BC4, these compounds own octa-reversible cationic charges (quaternary ammonium chloride salts) as a function of pH. A spectrophotometric pH titration in aqueous solution (from pH 1.50 to pH 10.70) was performed in order to obtain the pK_a value for the ammonium moieties, revealing a pK_a equal to ~ 4.64 (**Fig.56**).

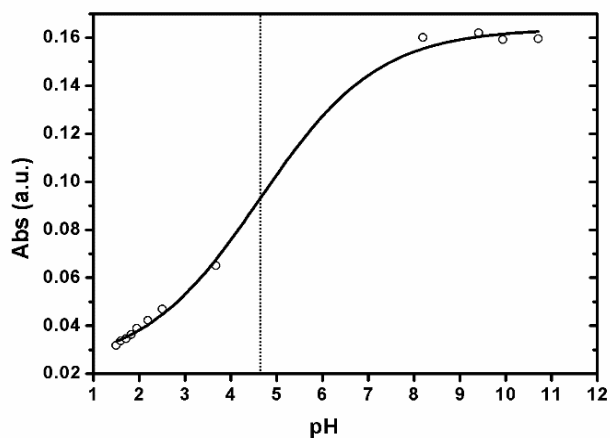


Fig.56 Absorbance ($\lambda = 300$ nm) vs. pH for titration of chiral-BC4-NH₂ (10 μM).

Water solutions of (RR)- or (SS)-BC4 are steady only in acid conditions (pH < 4) and this evidence suggests that free-base porphyrin, such as H₂DPPS3, cannot be employed in supramolecular complexes, due to the self-assembly phenomena, as a consequence of the core protonation steps. Hence, the need arises to employ a metal-derivative of H₂DPPS3 in order to prevent the core protonation under acid conditions.

The use of copper (II)-derivatives may be the suitable choice since the demetallation does not occur in acid solution and the tetra-coordination of the copper (II) does not hinder the formation of porphyrin-calixarene complexes.

The selected tri-anionic copper(II) 5,15-meso-bis(4-sulfonatophenyl)-2-sulfonato porphyrin (CuDPPS3) was synthesized starting from the H₂DPPS3 through a heterogeneous metal-insertion reaction by using copper(II) oxide (CuO).^[172]

The metalation reaction was carried out by adding about 1 mg of H₂DPPS3 to 10 ml of ultrapure water, obtained from Elga Purelab Flex system by Veolia, containing 20 mg of copper(II) oxide. The mixture was refluxed and kept under stirring up to 12 h during which small aliquots were withdrawn to monitor the progress of the reaction spectrophotometrically. The reaction was completed when the four Q-bands of the free-base porphyrin changed to two Q-bands of the metalloporphyrin (**Fig.57**-inset) and the excess solid phase was collected on a 0.2 μm Whatman syringe filter without further purification processes. Compared to free-base, CuDPPS3 ($\epsilon_{405,5}/\text{H}_2\text{O} = 1.100 \cdot 10^5 \text{ cm}^{-1} \text{ M}^{-1}$) displays a Soret band at 405,5 nm and two Q-band at 532 nm and 570 nm (**Fig.57**).

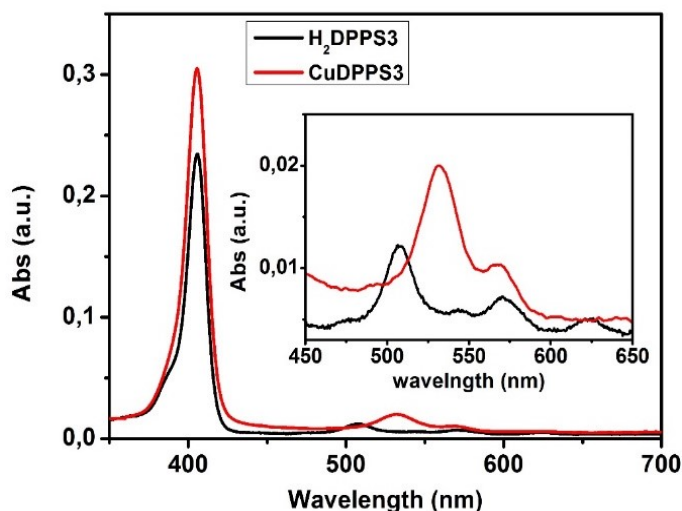


Fig.57 Absorption of an aqueous solution of H₂DPPS3 (2 μ M, pH 10.0 black line) and of CuDPPS3 (2.5 μ M, pH 7.0 red line); in inset are reported in detail the Q-bands of the two porphyrins.

The remarkable stability of CuDPPS3 under strong acid conditions (pH < 2.5) is shown in **Fig.58** in which a 3 μ M water solution of metallo-porphyrin is kept at pH = 2.0 for 24 hours. Indeed, the CuDPPS3 absorption spectrum at pH 2.0 is quite identical to that recorded at pH 7.0.

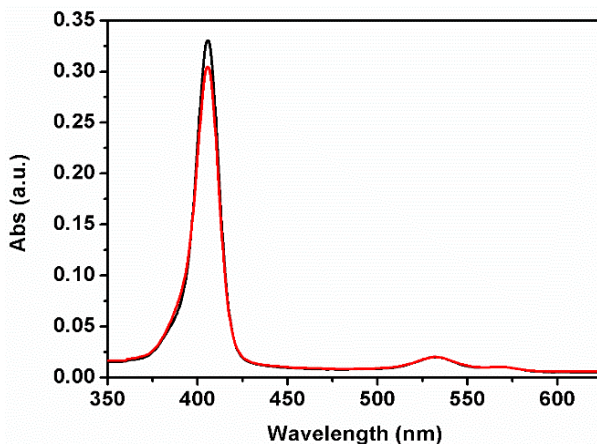


Fig.58 *Uv-vis spectra of an aqueous solution of CuDPPS3 (3 μ M) recorded at pH 7.0 (as prepared) and at pH 2.0 (incubated for 24h).*

A UV-vis spectrophotometric titration of a 2.5 μM aqueous solution (pH = 2.0) of chiral BC4-NH₂ with increasing amounts of CuDPPS3 (0.25 μM) causes, on the porphyrin Soret band ($\lambda = 405.5 \text{ nm}$), a progressive hypochromic effect modulated by the relative stoichiometry of the two complementary components present in solution (**Fig.59**).

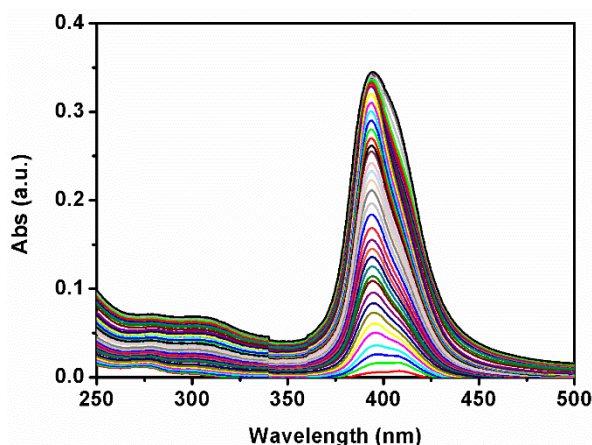


Fig.59 UV-vis absorption spectra recorded over the course of the titration of an aqueous solution of chiral BC4 (2.5 μM) with an aqueous solution of CuDPPS3, added stepwise (0.25 μM) to reach a final [CuDPPS3] = 11 μM at pH 2.0.

Close inspection of the diagram obtained by plotting the CuDPPS3 absorbance vs. the [CuDPPS3]/[chiral-BC4] ratio (**Fig.60**) reveals the formation of complexes of different stoichiometry.

The straight black dotted line (a) of **Fig.60** accounts for the absorbance (at $\lambda = 405.5 \text{ nm}$) of CuDPPS3 on its own, at increasing concentrations, while the multicoloured dotted line (b) refers to the absorbance measured, at 405.5 nm, upon titration of a 2.5 μM chiral-BC4 solution with increasing amounts of CuDPPS3 (0.25 μM) at pH = 2.0.

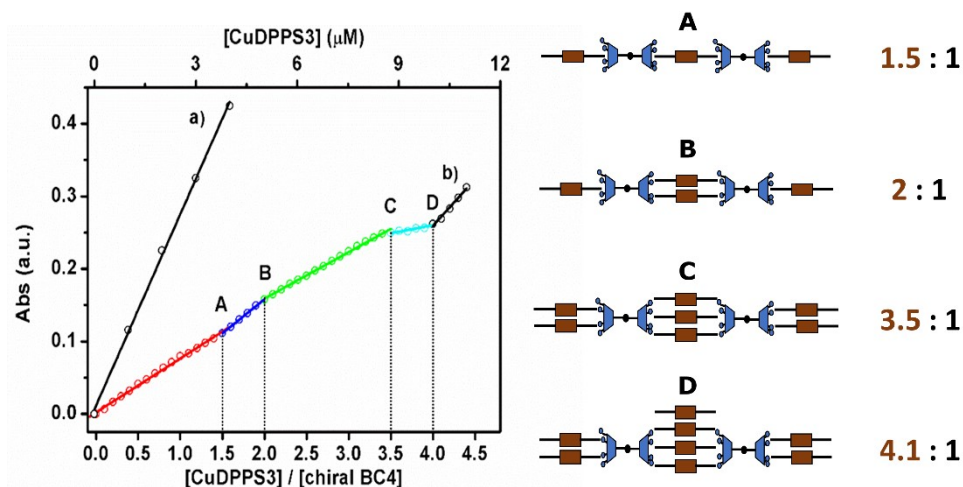


Fig.60 Variation in the absorbance of the CuDPPS3 Soret band ($\lambda = 405,5 \text{ nm}$) observed upon: (i) increase of the porphyrin concentration in water at pH 2.0 (black trace (a)) and (ii) portion-wise addition ($0.25 \mu\text{M}$) of the porphyrin to a $2.5 \mu\text{M}$ aqueous solution of chiral bis-calix[4]arene-NH₂ at pH 2.0 (trace (b)). On the right, schematic structures of the complexes are illustrated.

Stepwise formation of four discrete species – namely a 1.5:1-, 2:1-, 3.5:1- and 4:1 ([CuDPPS3] / [chiral BC4]) complexes – is indicated by the presence of four distinct *break-points* (labelled in **Fig.60** as A, B, C, D, respectively) characterized by a change in the trace slope (at least 12%). After addition of the fourth equiv. of porphyrin to *chiral* BC4, the slope of the titration curve becomes almost identical to that detected in the case of CuDPPS3 on its own (compare trace (a) with the black section of trace (b)) indicating that once the 4:1-(CuDPPS3/chiral-BC4) complex has quantitatively formed, the porphyrin molecules added in excess remain unbound in solution.

Compared to previous H₂DPPS3/BC4 system, we observe similar structure, confirming as well, the absence of break-points at 0.5, 1.0 and 3.0 CuDPPS3/chiral-BC4-NH₂ ratio. These latter changes may be explained in terms of *i*) different symmetry for metallo-porphyrin CuDPPS3 than free-base H₂DPPS3, and *ii*) peculiar molecular structure of chiral-BC4-NH₂ (**Fig.49b**) with

respect to reported BC4 (**Fig.44**-left). In addition, the presence of an equilibrium, as illustrated in **Fig.56**, could further affect the resultant stoichiometries.

In order to confirm these data, a Resonance Light Scattering (RLS) measurement were performed (**Fig.61**).[†]

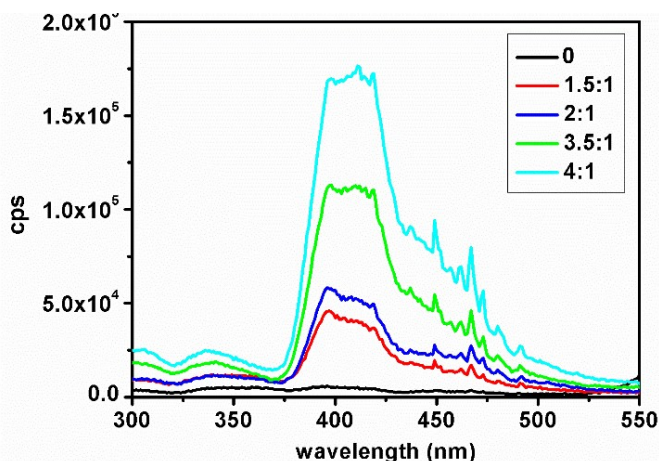


Fig.61 RLS spectra observed at the break-points upon portion-wise addition ($0.25 \mu\text{M}$) of the CuDPPS3 to a $2.5 \mu\text{M}$ aqueous solution of chiral bis-calix[4]arene at pH 2.0.

In accordance with the Uv-vis titration the formation of discrete porphyrin-calixarene complexes is also highlighted by an enhanced RLS response in the abovementioned break-points (1,5:1, 2:1, 3.5:1, 4:1- [CuDPPS3] / [chiral-BC4]).

Finally, the chiral nature of (RR)- or (SS)-BC4-NH₂ offers an immediate method to transfer chirality to the complexes by exploiting the chiral induction processes. In **Fig.62** is reported the step-wise formation of CuDPPS3/chiral-BC4-NH₂ complexes by monitoring the induced circular dichroism (ICD) signal. Noteworthy, under 2:1 ratio is not observed any ICD, likely due to a very low absorbance of the complexes (data not shown). Instead more striking an ICD

[†] Presumably, an instrumental problem is responsible for clipped peaks in RLS spectra.

4.2.1 Towards porphyrin/calix 1D assemblies:
H₂DPPS3/BC4 and CuDPPS3/chiral-BC4-NH₂ complexes

signal appears at 2:1 ratio, becoming more evident at 4:1 ratio. In other words, we succeeded to induce supramolecular chirality in 1D CuDPPS3/*chiral* BC4-NH₂ complexes.

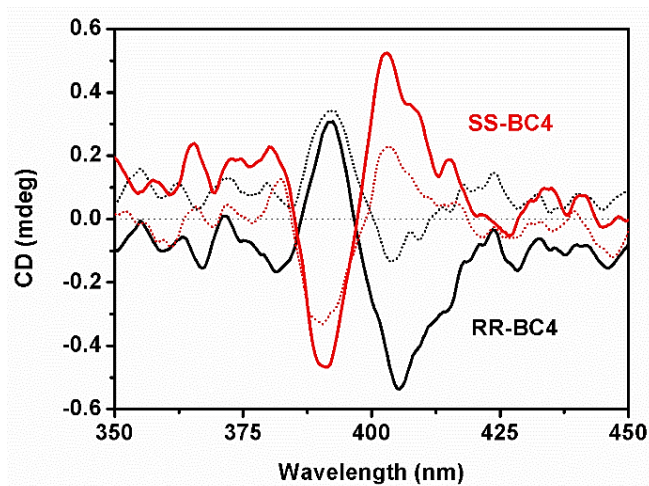


Fig.62 CD spectra of an aqueous solution at pH 2.0 of a) CuDPPS3 (5 μ M red dotted line, 10 μ M red solid line) in presence of (SS)-BC4 (2.5 μ M); b) CuDPPS3 (5 μ M black dotted line, 10 μ M black solid line) in presence of (RR)-BC4 (2.5 μ M).

- **H₂DPPS2 / BC4 complexes**

As illustrated, H₂DPPS3 and CuDPPS3 not only complex bis-calix[4]arenes hierarchically and stoichiometrically, but we are also able to transfer particular electronic properties into complexes, such as the chirality. However, both porphyrins own a sulfonate groups directly bonded to β -pyrrolic position and it may be intriguing to investigate about its role in the self-assembly process. To this end, we employed the corresponding di-sulfonated *5,15-meso-bis(4-sulfonatophenyl) porphyrin*, **H₂DPPS2** (**Fig.63**), and the cationic bis-calix[4]arene, BC4 (**Fig.44-left**).

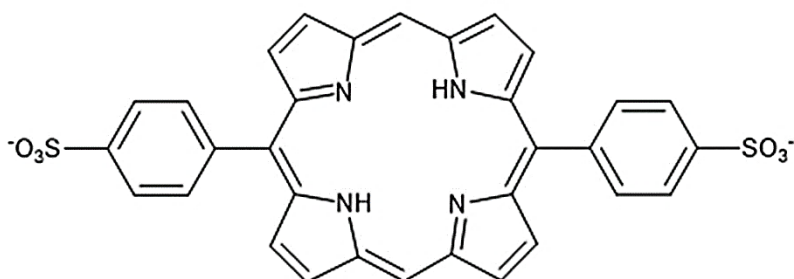


Fig.63 Molecular structure of H₂DPPS2.

H₂DPPS2 ($\epsilon_{400}/\text{H}_2\text{O} = 2.53 \cdot 10^5 \text{ cm M}^{-1}$) in water at pH 11 shows an intense *Soret* band at 400 nm and four *Q* band at 503 nm, 539 nm, 565 nm and 617 nm (**Fig.64a**, black plot). In acid condition (pH = 2.5) the core protonation occurs provoking the red-shift at 414 nm with two *Q* band at 562 nm and 619 nm (**Fig.64a**, red plot and its inset). Moreover, in **Fig.64b** are reported the respective fluorescence spectra at the same conditions.

4.2.1 Towards porphyrin/calix 1D assemblies: H₂DPPS2/BC4 complexes

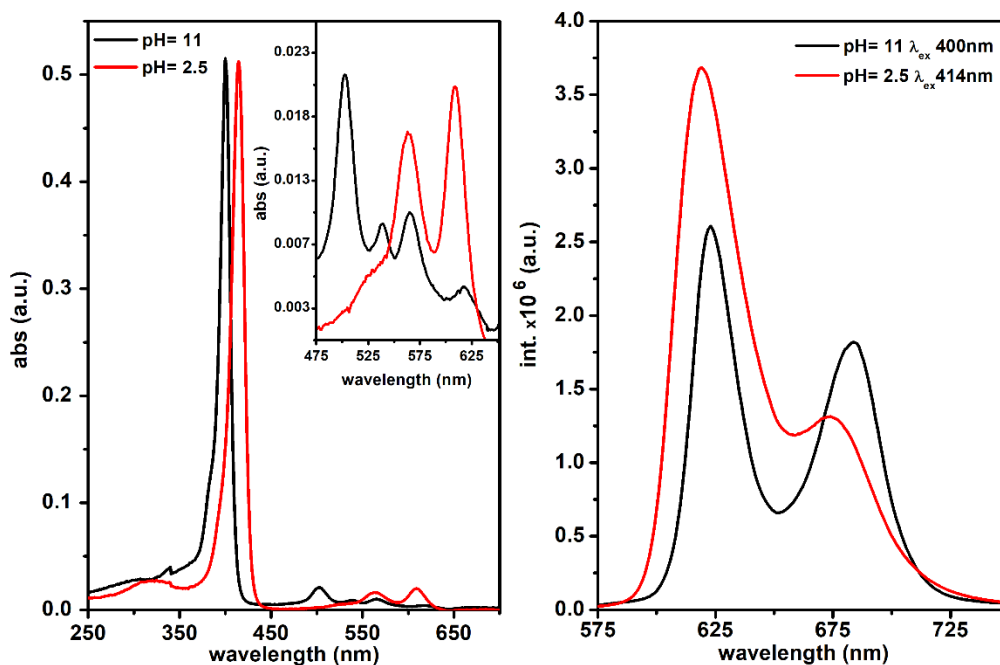


Fig.6.4 a) Abs spectra in water solution of H₂DPPS2 (2 μ M, pH 11.00-black solid line, pH 2.50-dotted red line), Q-bands are evidenced in inset; **b)** Fluorescence spectra of H₂DPPS2 2 μ M at pH 11.0 (λ_{ex} = 400nm-black line) and at pH 2.50 (λ_{ex} = 414nm-red line).

From *independent solutions experiments* (Fig.6.5) we calculated that the value of pK_a is about 3.50 (see inset of Fig.6.5). However, the pK_a becomes equal to 3.30 when a titration experiment is performed as shown in inset of Fig.6.6-panel b. This slight difference may be attributed to slow kinetic formation of H₂DPPS2's small aggregates by decreasing the pH during the titration, affecting as well, the real pK_a of the *porphyrin core*. The modest growth of the light scattering in RLS measurements (Fig.6.6-panel a), as result of the addition of acid to naked H₂DPPS2, seems to confirm such hypothesis. However, the experimental data rule out the possibility of an extensive aggregation process.

4.2.1 Towards porphyrin/calix 1D assemblies:
H₂DPPS2/BC4 complexes

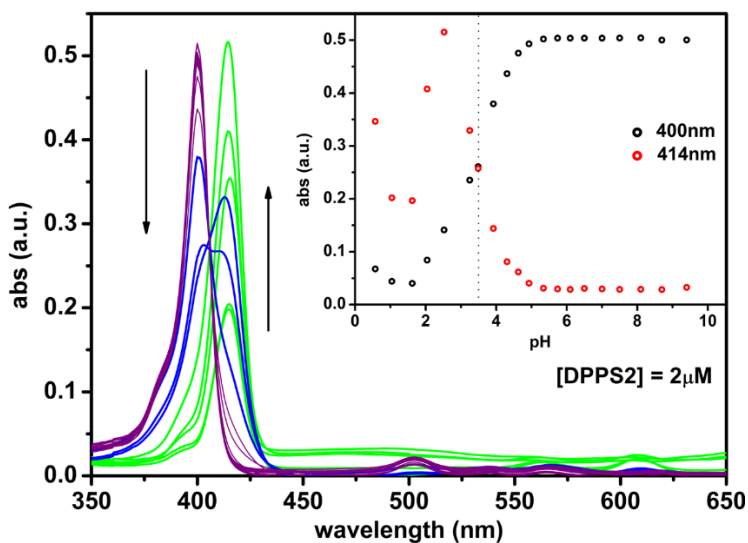


Fig.65 Absorption spectra of independent solutions of H₂DPPS2 2 μM at different pH from 9.43 to 0.69. Inset: Absorbance value at 400 nm (black circles) and at 414nm (red circles) vs. pH. The $pK_a \approx 3.50$.

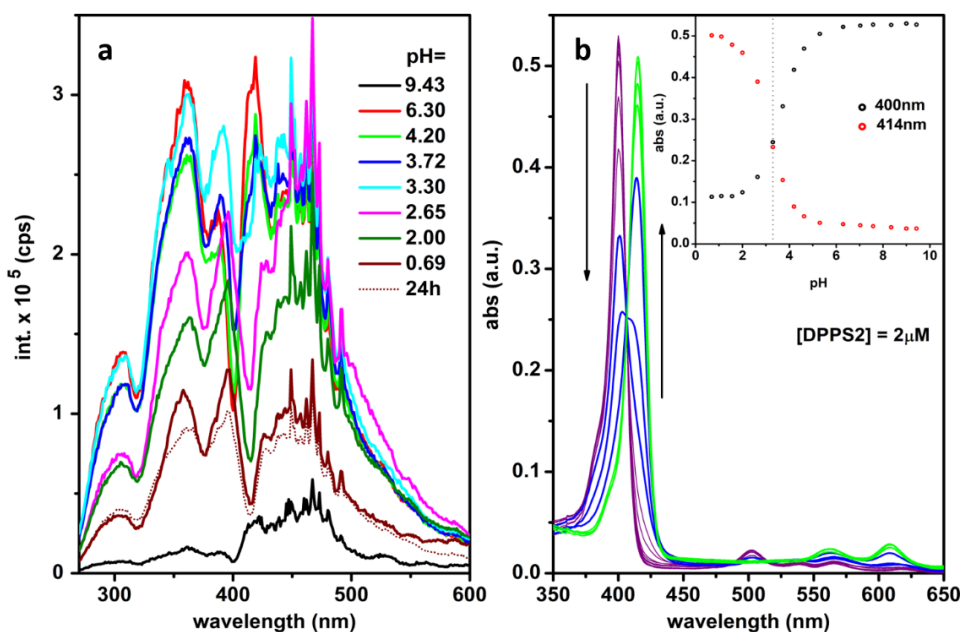


Fig 66 a) RLS spectra recorded during the titration of 2 μM H₂DPPS with HCl 6M and **b)** related Uv-Vis spectra. Inset: Abs value at 400 nm (black circles) and at 414nm (red circles) vs. pH. The $pK_a \approx 3.30$.

4.2.1 Towards porphyrin/calix 1D assemblies: H₂DPPS2/BC4 complexes

Afterwards, to investigate the interactions between the positively charged templating agent and the di-anionic porphyrin, we carried out a Uv-Vis titration of an aqueous solution of bis-calix[4]arene BC4 (2 μM, pH = 10) with increasing amounts (0.25 μM) of H₂DPPS2. As previously-observed, hypochromicity and broadening of the porphyrin Soret band occurs again over the course of the experiment (**Fig.67a**). Notable, a further absorption is present at about 350 nm (see panel a in **Fig.67**). According to literature,^[47] this band may be assigned to an energy-transfer process between BC4 and H₂DPPS2.

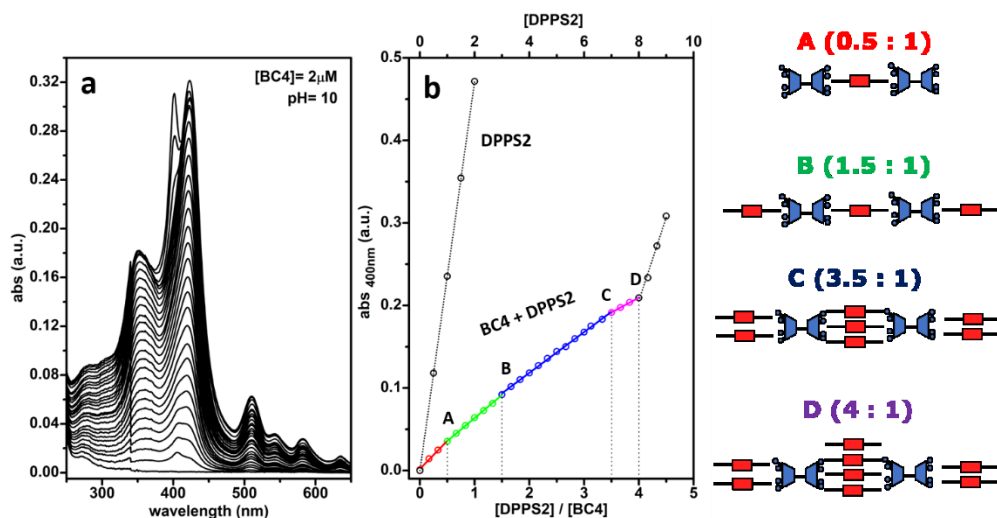


Fig 67 a) Uv-Vis absorption spectra recorded over the course of the titration of an aqueous solution of BC4 (2 μM) with an aqueous solution of H₂DPPS2, added stepwise (0.25 μM) at pH 10.0 **b)** Variation in the absorbance of the H₂DPPS2 Soret band (λ = 400 nm) observed upon: (i) increase of the porphyrin concentration in water at pH 10.0 (black dotted line) and (ii) portion-wise addition (0.25 μM) of the porphyrin to a 2 μM aqueous solution of BC4 at pH 10.0 (multi-colored line). On the right, schematic structures of the complexes are illustrated.

By plotting the variation of the absorbance at 400 nm versus the [H₂DPPS2] / [BC4] ratio, we can best monitor the self-assembly process. (**Fig.67b**). The self-assembly of the porphyrins in the presence of the bis-calix[4]arene templating

4.2.1 Towards porphyrin/calix 1D assemblies:
H₂DPPS2/BC4 complexes

agent (**Fig.67b** the black dotted line) corresponds to the absorbance of the Soret band of H₂DPPS2 in the absence of BC4. Instead, the multicolored dotted curve, refers to the experiment in which BC4 was titrated with H₂DPPS2. The latter indicates that the interaction of BC4 with H₂DPPS3 causes hypochromic effects modulated by the stoichiometry of the complex. In fact the control of complex stoichiometry is highlighted by the presence of *break-points* evidenced in **Fig.67b** at ratio [porph]/[calix] 0.5:1, 1.5:1, 3.5:1 and 4:1. Moreover, after addition of the fourth equiv. of porphyrin, the slope of the titration curve becomes almost identical to that detected for H₂DPPS3 on its own, indicating that the porphyrins are no longer interacting with the supramolecular complex. Nevertheless, the RLS spectra, performed at stoichiometric ratio (**Fig.68**), confirms the expected complexes as a consequence of their enhanced scattering.

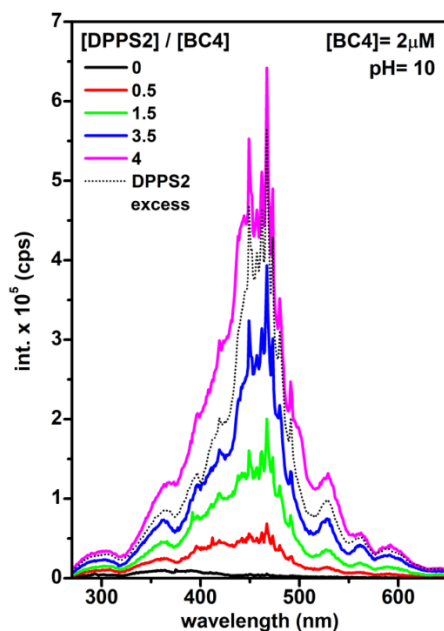


Fig 68 RLS spectra observed at the break-points upon portion-wise addition (0.25 μ M) of the H₂DPPS3 to a 2 μ M aqueous solution BC4 at pH 10.0.

4.2.1 Towards porphyrin/calix 1D assemblies: H₂DPPS2/BC4 complexes

The successful formation of H₂DPPS2/BC4 assemblies, having similar stoichiometries compared to H₂DPPS3/BC4 and CuDPPS3/chiral BC4-NH₂, suggests that the sulfonate group in β -pyrrolic position doesn't affect the entire self-assembly process.

4.2.2 Towards porphyrin/calix 2D assemblies:

- **CuTPPS/ Bis-Calix[4] tube complexes**

It has been demonstrated the possibility to govern the dimensionality of the porphyrin assemblies by means of the employment of suitable bis-calix[4]arenes (see ref.^[170] and also the state-of-the art in chapter 4.1).

However, the need to increase the rigidity of the entire assemblies is required in order to optimize the electronic communication. For this reason, a new calixarene building is necessary, and the choice falls on a water-soluble calix[4]tube based on a bis calix[4]arene scaffold: the octa-amino bis-calix[4]arene tube, namely BC4T, whose structure is reported in **Fig.69**.[†]

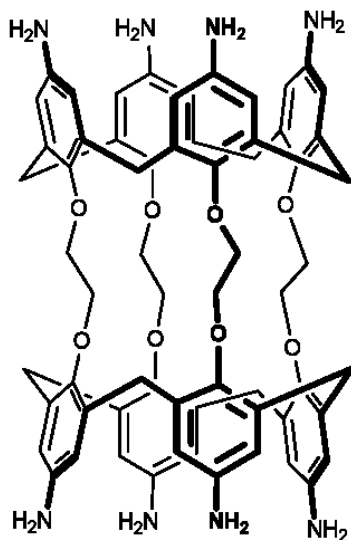


Fig 69 Molecular structure of BC4T.

[†] The organic synthesis of BC4T was performed by research group of Prof. M.F.Parisi (University of Messina), and research group of Prof. S.Pappalardo (University of Catania).

The BC4T reported in **Fig.69** owns the typical *cone* C_4 symmetry, nonetheless, in water a conformational equilibrium occurs, by determining the presence of flattened-cone conformers with C_{2v} symmetry (**Fig.70**).

As a rule, in mono-calix[4]arenes the interconversion between two C_{2v} symmetrical flattened cone conformers is fast on the NMR time scale and produces broadened spectra reflecting the time-averaged C_4 symmetry of the core.^[173] However, the conformational motions can be more or less efficiently suppressed by intramolecular bridging,^[174,175] or cation complexation.^[176,177]

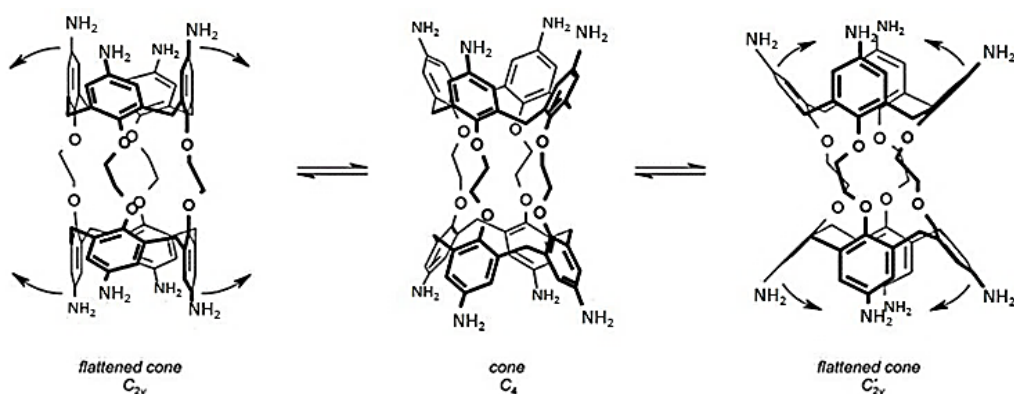


Fig 70 Conformational equilibrium in BC4T.

In BC4T, although the calix[4]arene counterparts are greatly rigidified in C_{2v} symmetry (in the solid state and also in solution), the conformational interconversion is not blocked but significantly decelerated.^[173] The conformational instability in water could represent an issue to achieve the porphyrin complexation correctly. To this end, we carried out a spectroscopic titration, by adding small aliquots (0.25 μM) of CuTPPS (**Fig.44-right**) to an aqueous solution of BC4T (2 μM , pH = 2.0[‡]). The host-guest interaction

[‡] Strong acid conditions are strictly necessary to guarantee the full protonation of the eight amino-groups in the BC4T. The evaluation of BC4T's pK_{a} s are under investigation.

CuTPPS4-BC4T are evidenced thanks to the Soret band's broadening and related hypochromicity (data not shown for this system). Moreover, a better analysis is reached by plotting the absorption at 412nm (i.e. Soret band's maximum) against the CuTPPS4/BC4T ratio, as reported in trace *b* of **Fig.71**.

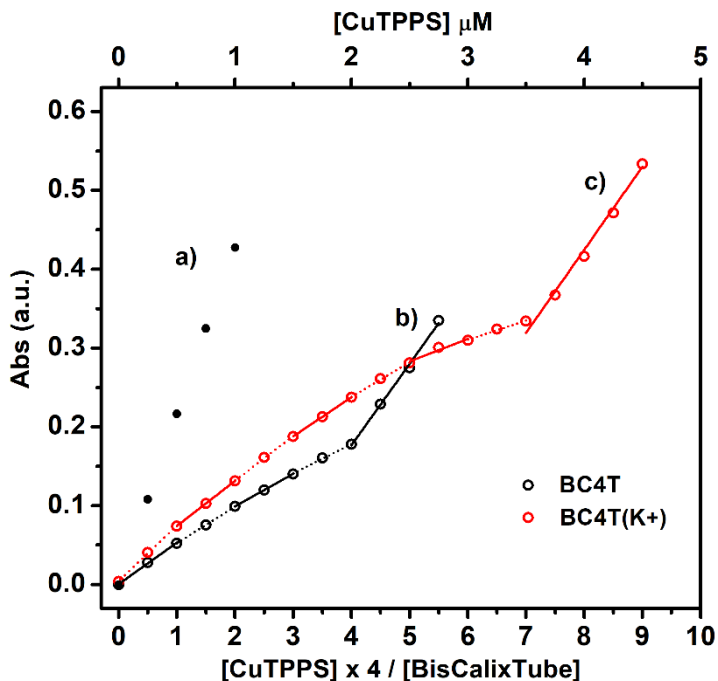


Fig.71 Absorbance at 412nm of CuTPPS4 ($\lambda = 412 \text{ nm}$) vs. $[\text{CuTPPS4}]x4/[\text{BC4Tube}]$ ratio upon: i) increase of porphyrin in water on its (trace *a* in black dots); ii) portion-wise addition of CuTPPS4 ($0.25 \mu\text{M}$) to $2\mu\text{M}$ aqueous solution of BC4T ($\text{pH}=2.0$, trace *b* in black); iii) portion-wise addition of CuTPPS4 ($0.25 \mu\text{M}$) to $2\mu\text{M}$ aqueous solution of BC4T(K^+) ($\text{pH}=2.0$, trace *c*).

However compared to previous systems, a close inspection of trace *b* in **Fig.71** reveals the absence of clear break-points, highlighting as well, the appearance of an unpredictable break-point at 4:4 ratio. After that, the absorbance becomes equal to a solution containing bare CuTPPS4 (compare the traces *a* and *b*). The excessive conformational mobility of the BC4T displays important effect on the lack of stoichiometric control.

Nevertheless, BC4T show a remarkable high selectivity for potassium cation, and as a consequence, the potassium complexation blocks the bis-calix[4]tube in the cone conformation (C_4 symmetry).^[178]

Concerning the mode of entry of potassium into the calix[4]tube, two routes can be possible: *axial route*, where the cation initially passes through the calix[4]arene filter and then onto the polyether binding site, and the equatorial route, in which the cation is complexed directly by rearrangement of the cryptand-like binding site (**Fig.72**). The NMR kinetic results showing dramatic variation in the rate of potassium complexation on alteration of the calix[4]arene upper rim substituent tend to suggest the axial route of complexation, as NMR structural investigations show the polyether binding region to be conserved.^[178]

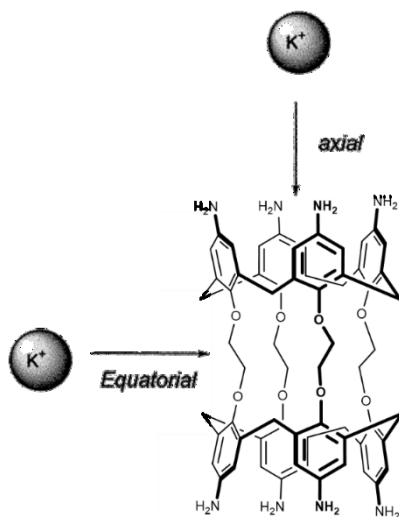


Fig 72 Potential routes for complexation of potassium by BC4T.

The potassium complexation was reached by treating 1 mg of BC4T, solubilized into 3 ml of DMF, with 10 mg of KI (molar ratio BC4T : KI = 1:88) under vigorous stirring for 20 days. Afterwards, the solution was filtered and evaporated in a rotavapor apparatus. The H^1 NMR characterization, as reported in

Fig.73, evidences several peaks due to simultaneous presence of the bis-calix[4] tube and the solvent (deuterated DMF). Respectively, the signals at 8.0ppm, 3.5ppm and around 2.7ppm are ascribable to the solvent. Instead, the doublet about at 4.60-4.62ppm is attributable to methylene bridges of the calix, but more important is the singlet at 6.63ppm. This latter represents the aromatic hydrogens when a cone conformation is obtained. Conversely, if the BC4T was in flatted cone conformation two different peak should be expected, as the C_{2v} symmetry implies unequal aromatic hydrogens. As a result, the 1H NMR measurements confirm the potassium complexation with a blocked cone conformation for the BC4T, now called BC4T(K^+)

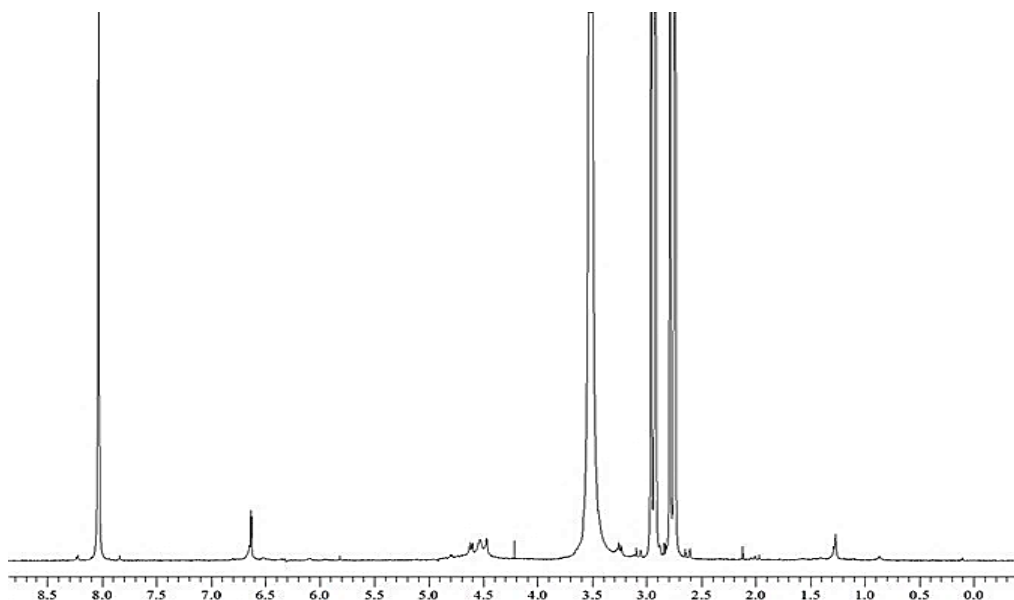


Fig 73 1H NMR pattern of BC4T(K^+) in deuterated DMF as solvent.

In addition to NMR experiments, ESI-MS measurements were carried out in order to confirm the correct compound, by preparing aqueous solution of

4.2.2 Towards porphyrin/calix 2D assemblies: CuTPPS4/bis-Calix[4]tube complexes

BC4(K⁺) 5 μM at pH = 2 to guarantee the protonation the amino group on the upper and lower rim (**Fig.74**).

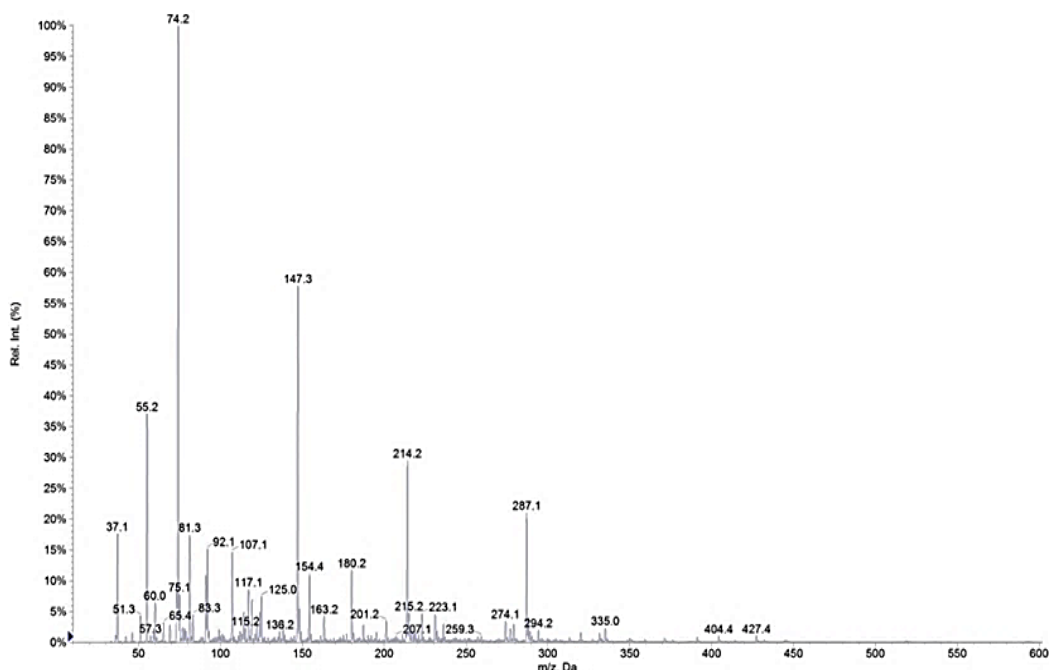


Fig 74 ESI-MS spectrum of BC4T(K⁺) sample in water (5 μM, pH=2.0).

MS pattern shows various peak ascribable not only to sample but also to traces of DMF from the previous potassium complexation step. In fact, signals at 74Da and 147Da belong to protonated DMF and protonated dimeric-DMF, respectively. Nevertheless, the most interesting peak is centered at 287.1Da as attributed to the species [BC4T(K⁺) + HCl] + 3H⁺. The remaining signals are ascribable to other fragmented cations of BC4T(K⁺) and related counterions.

As illustrated, BC4T(K⁺) is an homoditopic bis-calix[4]tube (above in **Fig.69**) with octa- amino groups whose protonation at pH =2.0 makes it soluble

in water and able to interact with anionic porphyrin such as copper (II) meso-tetrakis(4-sulfonatphey) porphyrin, CuTPPS4 (**Fig.44-right**).

To investigate the interactions between the positively charged templating agent and the tetra-anionic porphyrin, we carried out a Uv-Vis titration of an aqueous solution of bis-calix[4] tube BC4T(K⁺) (2 μ M) with increasing amounts (0.25 μ M) of CuTPPS at pH=2.0. In agreement with previous studies,^[47,170] hypochromicity and broadening of the porphyrin Soret band was observed over the course of the experiment (**Fig.75**).

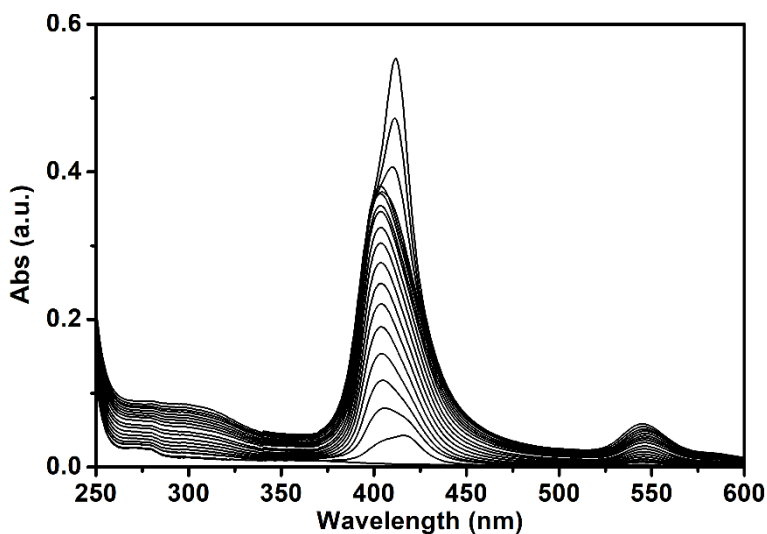


Fig.75 UV-vis absorption spectra recorded over the course of the titration of an aqueous solution of BC4T(K⁺) (2 μ M) with an aqueous solution of CuTPPS4, added stepwise (0.25 μ M) at pH 2.0.

The self-assembly of the porphyrins in the presence of the bis-calix[4]arene templating agent can best be analyzed and understood by plotting the variation of the absorbance at 412 nm versus the [CuTPPS] x 4/ [BC4T(K⁺)] ratio. Compared to CuTPPS4-BC4T system (trace b in **Fig.71**), here the stoichiometric control is proved by visible *break-points* at ratio [porph]/[calix] 1:4, 2:4, 3:4, 4:4, 5:4, 6:4 and 7:4 (see trace c -red circles- in **Fig.71**). Moreover, after addition of

the seventh equiv. of porphyrin, the slope of the titration curve becomes almost identical to that detected for CuTPPS on its own (compare traces *a* and *c* in **Fig.71**) indicating that *i*) porphyrins are no longer interacting with the supramolecular complex and *ii*) the maximum stoichiometry [porph]/[calix] is 7:4.

The CuTPPS-BC4T(K⁺) complex with stoichiometry 7:4 corresponds to a tridimensional structure where two porphyrins are stacked above and below the plane traced from the 5:4 complex (see **Fig.76** route **a** and also trace *b* in **Fig.77**).

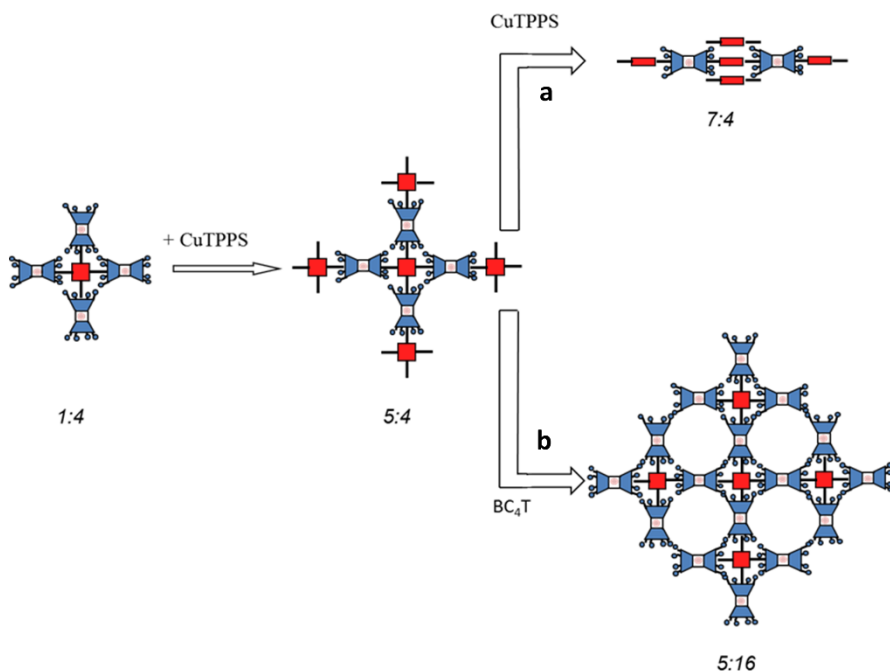


Fig.76 Schematic illustration about the dimensionality control in supramolecular complex CuTPPS-BC4T(K⁺): route **a**, 3D growth when two equivs. of CuTPPS are added to 5:4 structure; route **b**, in-plane growth when four equivs. of BC4T(K⁺) are added to pre-formed 5:4 complex.

Nonetheless, the addition of twelve equivalents of BC4T(K⁺) at the 5:4 complex doesn't produce large variation in absorbance (compare the *abs* between 5:4 and 5:16 complexes as indicated in **Fig.77**), pointing out the opportunity to

extend the structure over the plane (i.e., the 5:16 species – see **Fig.76** route *b* and also trace *c* in **Fig.77** below).

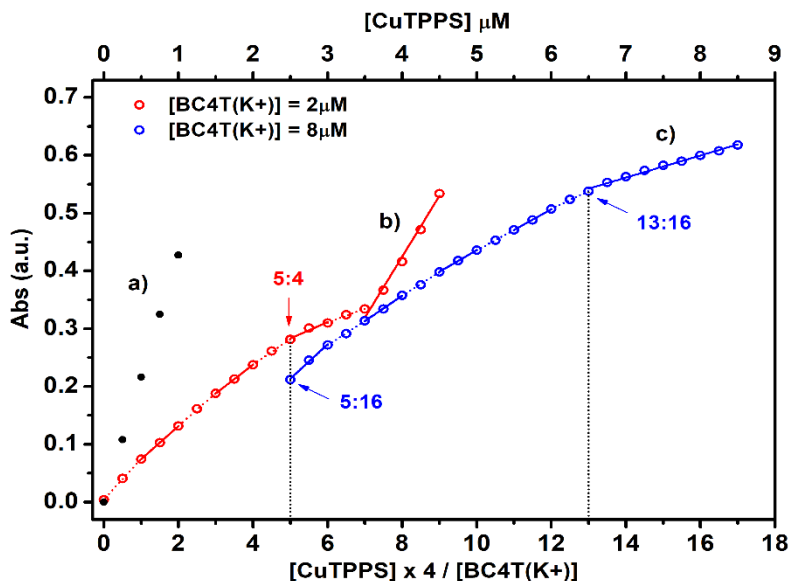


Fig.77 Variation in the absorbance of the CuTPPS4 Soret band ($\lambda = 412 \text{ nm}$) observed upon: i) increase of the porphyrin concentration in water at pH 2.0 (black dots, trace *a*); ii) portion-wise addition ($0.25 \mu\text{M}$) of CuTPPS4 to $2 \mu\text{M}$ aqueous solution of BC4T(K⁺) at pH 2.0 (red dots, trace *b*). Another experiment is shown in, trace *c*: as in the first case, a gradual titration of BC4T(K⁺) ($2 \mu\text{M}$, pH = 2.0) with CuTPPS4 is performed up to ratio 5:4 (see the red arrow at ratio 5:4 in trace *b*). Then, twelve equiv. of BC4T(K⁺) are added (i.e. total [BC4T(K⁺)] = $8 \mu\text{M}$) to build 5:16 complex (see the blue arrow at ratio 5:16 in trace *c*). The titration was continued until $8.5 \mu\text{M}$ of CuTPPS4 (trace *c*, blue circles).

In fact, the addition of CuTPPS4 at pre-formed 5:16 complex provokes a significant hypochromicity (see trace *c* -blue circles- in **Fig.77**) which becomes more evident after the ratio [porph]/[calix] = 13:16 (see blue arrow at 13:16). In other words, in order to increase the stoichiometric from 5:16 to 13:16, 8 equiv. of CuTPPS4 bind the BC4T(K⁺)'s free-cavities as schematized in **Fig.78**. The following porphyrin piling, above and below the plane of 13:16 species, is responsible of a more significant hypochromic effect after ratio 13:16. Although

4.2.2 Towards porphyrin/calix 2D assemblies: CuTPPS4/bis-Calix[4]tube complexes

the highest stoichiometry observed in these complexes is 32:16 (i.e. due to charge balance), beyond ratio 17:16 the species start to precipitate and ,consequently, the titration was interrupted.

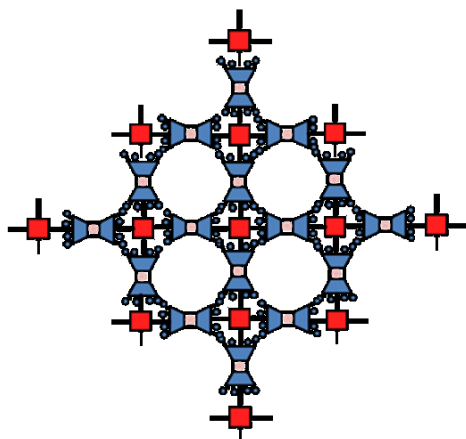


Fig.78 Schematic illustration of the 2D complex with ratio $[porph]/[calix] = 13:16$.

In conclusion, we demonstrated that the entrapping of potassium ion blocks the octa-amino bis-calix[4]tube in a *cone* conformation makes it able to complex the CuTPPS4 in water with 100% of yield. Moreover, the hierarchical titration allows for an exact stoichiometric control, switching as well, from 3D to 2D structure.

4.2.3 Towards long distance chiral transfer in porphyrin/calix 2D assemblies

In state-of-the-art (chap. 4.1- pag.68), it has demonstrated the possibility to transfer chirality to porphyrin-calixarene complexes in water solution by a fully non-covalent approach.^[171] In summary, upon formed the 1:4 (porph:calix) complex using the stepwise addition of copper(II) meso-tetrakis(4-sulfonatophenyl)-porphyrin (CuTPPS4, **Fig.79-right**) to water solution of (BC4-NH2, **Fig.79-left**), we performed addition of Δ -[Ru(phen)₃]²⁺ (or Λ -[Ru(phen)₃]²⁺), as chiral templating agents,^[179] producing the final ternary complex 1:4:4 (CuTPPS:BC4-NH2:Ru(phen)₃). Finally we detected optical activity in the Soret region of the central CuTPPS, suggesting electronic communication between the external inducer and the central core of the supramolecular complex and consequently transmission of chirality.

Although we have evidenced a short-range chiral transmission, most striking is, however, the perspective to enhance the chiral-transfer path in order to achieve a long-range chiral induction. In the light of these considerations, herein, we demonstrate that control over long-distance chiral communication has now been achieved. In order to demonstrate long-range chiral induction, we employed two metallo-porphyrins, such as manganese(III) meso-tetrakis(4-sulfonatophenyl)-porphyrin (MnTPPS4) and CuTPPS4 (**Fig.79-right**), having different values of absorbance maximum wavelength, allowing to detect distinct induced CD bands. BC4-NH2 (**Fig.79-left**) was selected as molecular building blocks to realize the multi-porphyrin complexes with desired stoichiometry.

4.2.3 Towards long distance chiral transfer in porphyrin/calix[4]arene 2D assemblies

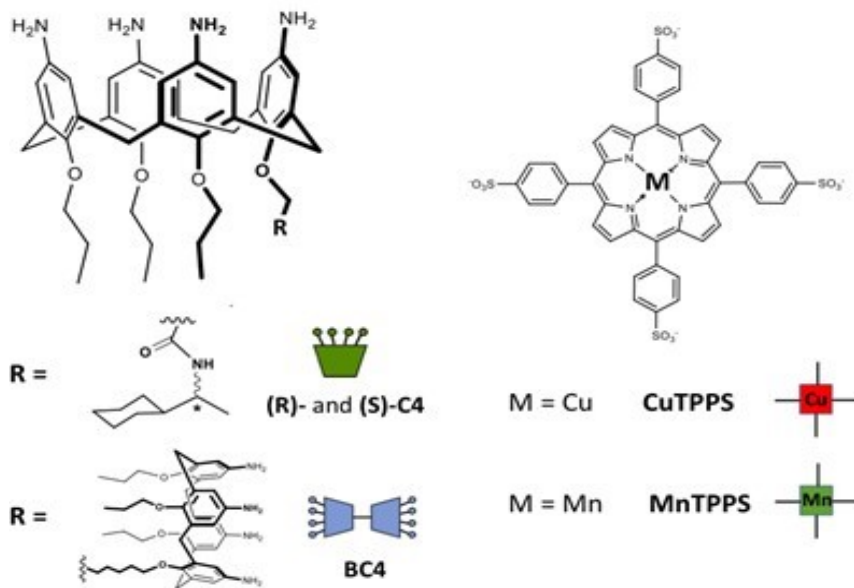


Fig.79 Molecular structure of BC4-NH₂, (R)-and (S)-C4, MnTPPS₄ and CuTPPS₄.

Then, enantiomeric forms of 5,11,17,23-tetraamino-25,26,27-tripropoxy-28-[1-cyclohexylethylaminocarbonyl methoxy] ((R)- and (S)-C4, **Fig.79**-left) were employed to convey chirality in the entire network.

First of all, we have confirmed the formation of MnTPPS₄-BC4-NH₂ complex at the desired ratio (1:4) in water solution by Uv-Vis and fluorescence measurements (**Fig.80**). In details, we performed stepwise addition of increasing amount of MnTPPS₄ (up to 2.50 μM) to 10 μM aqueous solution of BC4-NH₂. As we reported previously the formation of porphyrin-calixarene complexes is driven by electrostatic interaction, therefore in order to foster the formation of MnTPPS₄-BC4-NH₂ (1:4) complex we decrease the pH of the bis-calix solution at 2. Indeed at this pH we demonstrated that BC4-NH₂ is completely cationic.^{[171]†}

† BC4-NH₂ pK_{a1} = 4.5, pK_{a2} = 7.0 and chiral-C4 pK_a = 2.5

4.2.3 Towards long distance chiral transfer in porphyrin/calix[4]arene 2D assemblies

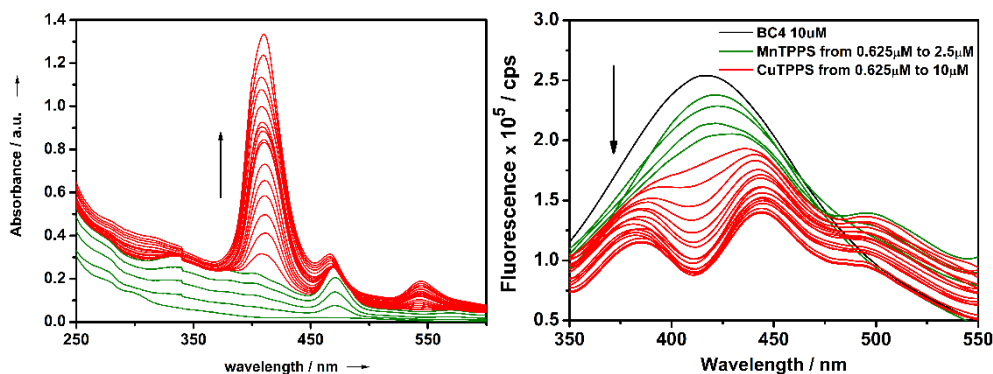


Fig.80 Left-UV-Vis spectra throughout the stepwise titration of 10 μM BC4 (pH=2.0) with small aliquots of MnTPPS4 (up to 2.5 μM, green line) and CuTPPS (up to 10 μM red line). At the end of titration the total concentration of porphyrin was 12.5 μM; Right- Fluorescence emission spectra of the same experiment.

Gradual hypochromic effects and broadening band in the Soret regions of MnTPPS4 (see **Fig.80**-left), supported by a progressive quenching of the emission of BC4-NH2 (**Fig.80**-right), indicate the self-assembly of MnTPPS4 and BC4-NH2. According to previous works,^[47,171] the step-by-step formation of the porphyrin-calixarene complexes can be monitored by plotting the absorbance value (or the fluorescence emission) of porphyrin versus [porphyrin]⁴/[BC4-NH2] ratio (**Fig.81**).

In the case of multi-metalloporphyrin:calixarene complexes in order to avoid spectral interferences due to simultaneous presence of different metallo porphyrin with similar absorbance wavelength maximum i.e. MnTPPS4 ($\lambda_{max} = 467\text{nm}$) and CuTPPS4 ($\lambda_{max} = 412\text{nm}$), we prefer report the absorbance and fluorescence of calixarene involved in the assembly (absorbance at $\lambda = 300\text{nm}$ and fluorescence at $\lambda=425\text{nm}$ for BC4-NH2, **Fig.81**).

Consequently, the addition of 1 equivalent of MnTPPS4 to BC4-NH2 solution causes the formation of the first stoichiometric complex 1:4 (MnTPPS4 : BC4-NH2) denoted by the break-point A (**Fig.81**).

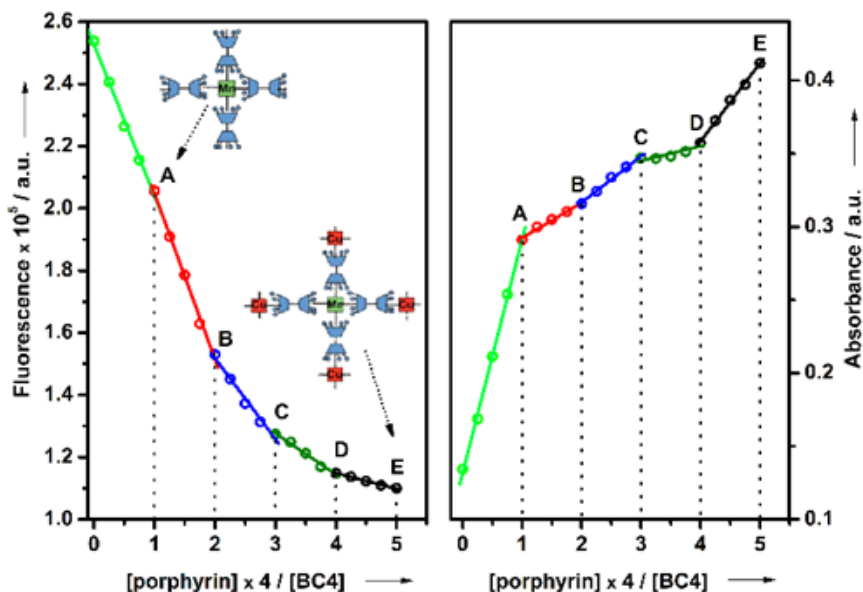


Fig.81 Spectroscopic variations of BC4-NH2 ($10\mu\text{M}$, $\text{pH}=2.0$) in emission (left part) at 425nm ($\lambda_{\text{ex}}=300\text{nm}$) and in absorption (right part) at 300nm . Break-points, namely A, B, C, D and E, represent the stoichiometric ratio 1:4-, 2:4-, 3:4-, 4:4- [porphyrin]/[BC4-NH2] of the mixed-complexes. On the left panel are illustrated the schematic structures for the first complex -1:4 MnTPPS4/BC4-NH2- and for the intermediate complex -1:4:4 MnTPPS4/BC4-NH2/CuTPPS4.

Afterwards, we proceeded the titration by adding different anionic porphyrin, CuTPPS, to fabricate the multi-metalloporphyrin complexes. Noteworthy, the complexation of CuTPPS provokes remarkable spectra variations in the fluorescence and absorbance of BC4-NH2, resulting in a large slope change beyond the first break-point (**Fig.81**-red dots). In details, fluorescence and absorption plots of **Fig.81** show the existence of five distinct break-points (A, B, C, D and E) characterized by a change in the trace slopes (at least 15% of variation) suggesting the formation of stable discrete species (1:4:1, 1:4:2, 1:4:3, 1:4:4 MnTPPS4:BC4-NH2:CuTPPS4 complexes), not in equilibrium each other and with 100% yield.

As we demonstrated previously, electronic communication between peripheral (CuTPPS4) and central (MnTPPS4) porphyrin mediated by BC4-NH2 occurs.^[170] As a result of perturbing the electronic properties of the peripheral porphyrin, some effect should be detected also for the central porphyrin. Starting from this consideration, we have induced the interaction of chiral mono calixarene C4 (**Fig.79**-left) with peripheral CuTPPS4 in the 1:4:4 complex (MnTPPS4:BC4-NH2:CuTPPS4) in order to transfer the chiral information also to the central MnTPPS4.

In details, we performed addition of 12 equivalents of (S)-C4 to preformed 1:4:4 complex (MnTPPS4:BC4-NH2:CuTPPS4) at pH=2; identical experiment was carried out with (R)-C4. Unlike the previous case discussed above, concerning ternary complexes in presence of chiral $[\text{Ru}(\text{phen})_3]^{2+}$, here major complexity is expected, indeed in the new assembly 1:4:4 complex (MnTPPS4:BC4-NH2:CuTPPS4) the transfer of chirality should occur across a long-distance from the outside to the inner part of the assembly. Hence, the gradual addition of chiral (S)-C4 to preformed assemblies, as expected, provokes the appearance of dichroic signals in the Soret region of CuTPPS4 (**Fig.82**). Noteworthy, optical activity is observed also in the MnTPPS4 absorption region (**Fig.82**) confirming the long-distance chiral induction. Mirror image is detected when the (R)-C4 enantiomer is used.

A potential explanation of this phenomena is the strong electron communication of the molecular building blocks involved in the supramolecular complex. In particular, the presence of a robust electronic coupling between the two chromophores, CuTPPS4 and MnTPPS4, detectable in the above-mentioned spectroscopic data, is responsive for long-range chiral transfer by non-covalent approach.

In summary, we have demonstrated that exploiting the hierarchical rules of supramolecular systems it possible to induce controlled self-assembly in aqueous solution of MnTPPS4, BC4-NH2, CuTPPS4 and chiral-C4 to realize a discrete supramolecular complex with desired stoichiometry. Moreover chirality has been successfully transferred to entire complex via the non-covalent interaction of chiral C4 with the peripheral building block, proving as well, the first long-range chiral induction in multi-porphyrin-calixarene complexes. Noteworthy, the central MnTPPS4 does not directly interact with chiral mono calix C4 as well as it is not in close contact with CuTPPS4.

On the other hand, these findings accentuate the feasibility of non-covalent synthesis as efficient strategy for the building of complex supramolecular arrays imprinting defined features in terms of electron and chiral properties.

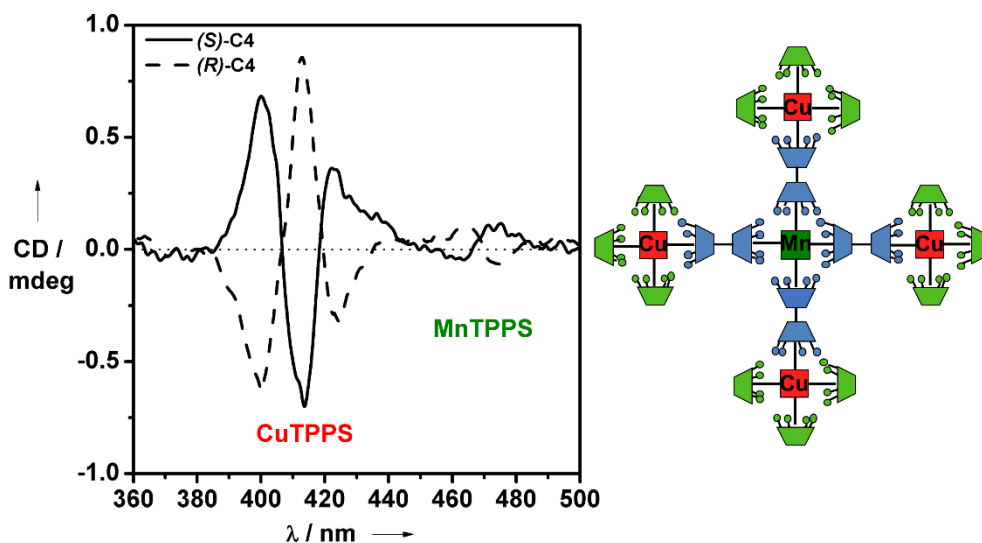


Fig.82 Circular dichroism spectra of the enantiomeric 1:4:4:12-MnTPPS4/BC4-NH2/CuTPPS4/(S)-C4 complex (solid trace, pH=2.0, [MnTPPS]=2.5 μ M, [BC4-NH2]=10 μ M, [CuTPPS]=10 μ M, [(S)-C4]=30 μ M). A mirror image CD signal is correctly observed in presence of the enantiomer (R)-C4 (dashed trace). On the right part is schematized the structure of the final chiral mixed-complex.

4.2.4 Towards porphyrin/calix 2D/3D assemblies:

- **CuTPPS4/ tris-calix[4] arene complexes**

Tris-calix[4]arene dodeca-ammonium chloride, **TC4** (**Fig.83**-left), was obtained from the corresponding dodeca-amino precursor upon treatment with a 0.01 M aqueous HCl solution. Enantiopure calix[4]arene tetra-ammonium chlorides, (R)- and (S)-C4 (**Fig.83**-centre) were available from previous studies.^[171] TC4 and C4 are soluble in water and, as a result, readily available to electrostatically interact with the tetra-anionic Cu(II) meso-tetrakis(4-sulfonatophenyl)porphyrin tetrasodium salt, CuTPPS4 (**Fig.83**-right).

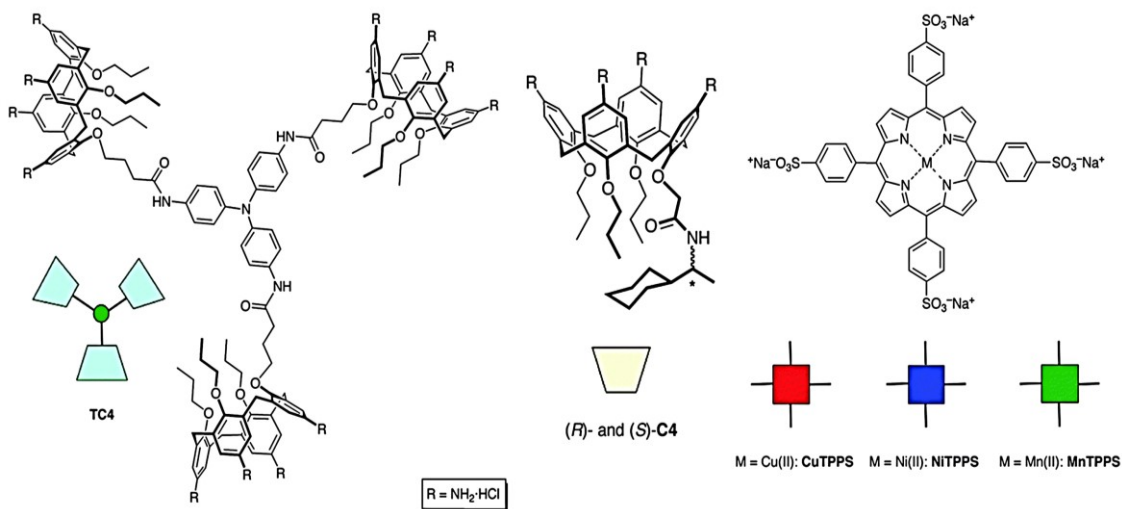


Fig.83 Molecular structures of *TC4* (left), (R)- and (S)-C4 (centre), CuTPPS4, NiTPPS4 and MnTPPS4 (right).

A Uv-Vis spectrophotometric titration of a 0.5 μ M aqueous solution of TC4 with increasing amounts of CuTPPS4 causes, on the porphyrin Soret band (λ_{max} = 412nm), a progressive hypochromic effect modulated by the relative stoichiometry of the two complementary components present in solution (data

not shown).^[18] Close inspection of the diagram obtained by plotting the CuTPPS4 absorbance vs. the [CuTPPS4]/[TC4] ratio (**Fig.84**) reveals the formation of complexes of different stoichiometry.

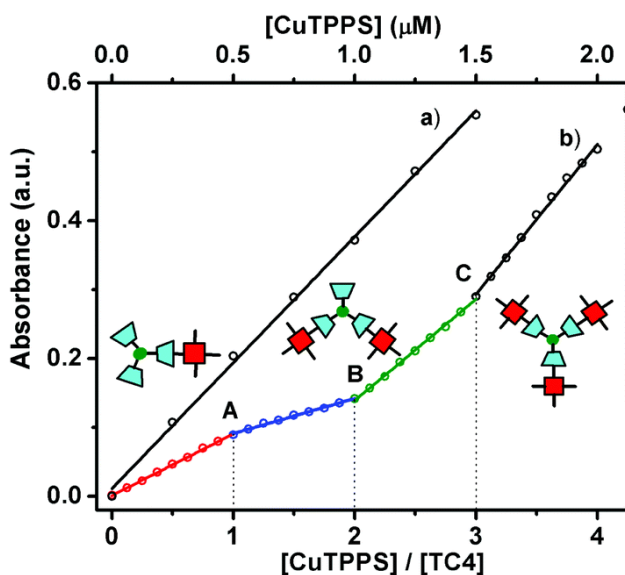


Fig.84 Variation in the absorbance of the CuTPPS4 Soret band ($\lambda_{max} = 412$ nm) observed upon: (i) increase of the porphyrin concentration in water (black trace a)) and (ii) portion-wise addition of the porphyrin to a 0.5 μM aqueous solution of tris-calix[4]arene TC4 at pH 2 (trace b).

The straight black line (a) of **Fig.84** accounts for the absorbance (at $\lambda_{max} = 412$ nm) of CuTPPS on its own, at increasing concentrations, while the multicoloured broken line (b) refers to the absorbance measured, at 412 nm, upon titration of a TC4 solution with increasing amounts of CuTPPS4.

Stepwise formation of three discrete species – namely a 1:1, 2:1 and 3:1- (CuTPPS4:TC4) complex – is indicated by the presence of three distinct *break-points* (labelled in **Fig.84** as A, B and C, respectively) characterized by a change in the trace slope. After addition of the third equiv. of porphyrin to TC4, the slope of the titration curve becomes almost identical to that detected in the case of

CuTPPS4 on its own indicating that once the 3:1 (CuTPPS4:TC4) complex has quantitatively formed, the porphyrin molecules added in excess remain unbound in solution.

Unlike the supramolecular assemblies formed in the presence of mono- and bis-calixarenes CuTPPS4 was seen to occupy the center of the supramolecular aggregate, driving the formation of the initial 1 : 4-(porphyrin-bis-calixarene) complex, in the present case tris-calixarene TC4 is the species dictating the stoichiometry of the self-assembly. The shape and bulkiness of TC4 most likely prevents the formation of a similar 1 : 4-(porphyrin/tris-calixarene) complex, favoring, on the contrary, the assembly of a 3:1 (porphyrin : tris-calixarene) complex in which TC4 acts as the core unit and the three CuTPPS4 units surround it (see the schematic structure in **Fig.84**).

The three distinct break-points not only provide clear-cut evidence of the stepwise formation of 3: 1 (CuTPPS4:TC4) complexes, but also suggest the possibility of preparing mixed-porphyrin/tris-calixarene supramolecular complexes, by simply tuning the stoichiometric addition of different anionic metallo-porphyrins to a tris-calixarene solution. To this end, a spectrofluorimetric (as well as a Uv-Vis) titration of a 10 μ M aqueous solution of TC4 with increasing amounts of different metallo-porphyrins (*i.e.*, the tetrasodium salt of Cu(II), Ni(II) and Mn(III) *meso*-tetrakis(4-sulfonatophenyl)porphyrins, **CuTPPS4**, **NiTPPS4** and **MnTPPS4**, respectively, see **Fig.83-right**) was carried out (**Fig.85**).

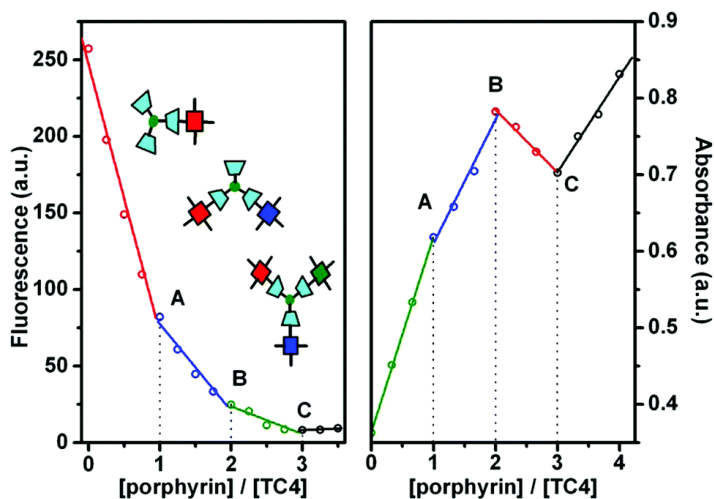


Fig.85 Variation of the TC4 ($10\mu\text{M}$ at pH 2) emission at 390 nm ($\lambda_{\text{ex}} = 320$ nm, left panel) and absorption at 320 nm (right panel) vs. $[\text{porphyrin}]/[\text{TC4}]$. Break-points A, B, and C indicate the $[\text{porphyrin}]/[\text{TC4}]$ ratio at which the 1:1 -, 2:1- and 3:1- complexes, respectively are fully formed. The red, blue and green segments are meant to match the color code used to represent the three different porphyrins CuTPPS4, NiTPPS4 and MnTPPS4, respectively.

The plot of the variation of the TC4 emission vs. the $[\text{porphyrin}]/[\text{TC4}]$ ratio, in analogy to what was seen above, shows also in this case three break-points peaking at the expected 1:1, 2:1 and 3:1 ratios, thus confirming the stepwise formation of mixed-porphyrin/tris-calixarene complexes of well-defined stoichiometry (**Fig.85** left panel). Consistently, a similar trend was also detected (**Fig.85** right panel) when the order of addition of the metallo-porphyrins to TC4 was reversed and the titration experiment was followed by Uv-Vis spectroscopy by looking at the TC4 absorbance ($\lambda_{\text{max}} = 320$ nm).

Besides the additional proof in favour of a stepwise assembly, collected with this mixed-porphyrin experiment, it should be emphasized that metallo-porphyrins, in general, exhibit different electronic properties and consequently the non-covalent synthesis of hetero-porphyrin arrays with tuneable stoichiometry and sequence is a very appealing starting point towards the design of materials for electronic devices. Further growth of the 3 : 1-(CuTPPS4:TC4)

complex into bigger aggregates may in principle proceed along to two different pathways depending on the order/type in which building blocks are added: *i*) addition of TC4 (3 equiv. with respect to the initial tris-calixarene concentration), should induce a radial growth as a result of multiple electrostatic (sulfonate/ammonium) interactions between porphyrin and tris-calixarene subunits, *ii*) conversely, addition of appropriate monotopic calix[4]arene “stoppers” (9 equiv. with respect to the initial tris-calixarene concentration) followed by a porphyrin topping should, likely, yield a thickening of the supramolecular assembly promoted by π - π stacking interactions between piled porphyrins (**Fig.86**).

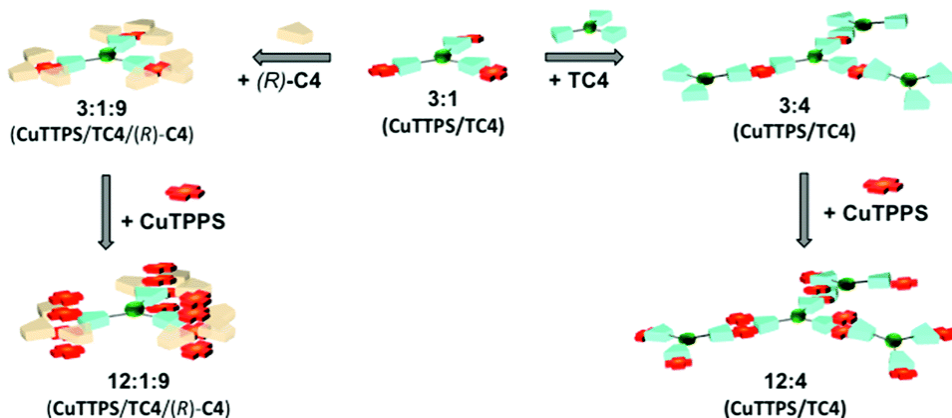


Fig.86 Schematic representation of the two-possible growth pathways starting from the 3:1-(CuTPPS4/TC4) core complex.

The former path relies on the above-mentioned inability of CuTPPS4 to simultaneously bind four (sterically congested) TC4 molecules. In line with our prediction, addition of TC4 (3 equiv.) to the 3 : 1-(CuTPPS4:TC4) complex did not produce any significant variation of the absorbance (compare the two data-points represented by the first red circle of trace (b) in **Fig.87** with the close blue square. This spectroscopic evidence is consistent with the formation of a 3 : 4-

(CuTPPS:TC4) assembly depicted in **Fig.86**, where one cavity of the newly added tris-calixarene is most likely interacting with the less hindered sulfonate group of the porphyrin.

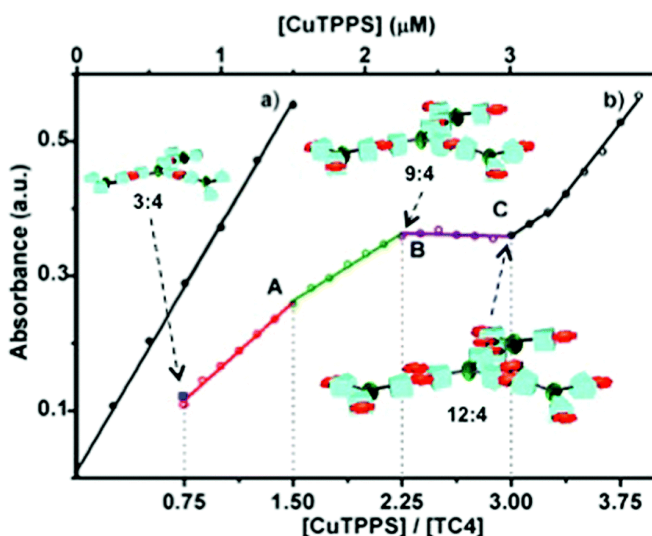


Fig.87 Variation in the absorbance of the CuTPPS4 Soret band ($\lambda_{\max} = 412 \text{ nm}$) observed upon: (i) increase of the porphyrin concentration in water (black trace a) and (ii) portion-wise addition of CuTPPS4 to a pre-formed 3:4 species ($[\text{CuTPPS4}] = 0.75 \mu\text{M}$ and $[\text{TC4}] = 1.0 \mu\text{M}$) at pH 2 (trace b). The changes in slope of trace (b) – corresponding to break-points A, B and C – indicate the $[\text{CuTPPS4}]/[\text{TC4}]$ ratio at which the 6:4, 9:4 and 12:4 assemblies, respectively are fully formed. The data-point represented by the blue square, next to the red section of trace (b), refers to the absorption of the 3:1-(CuTPPS4/TC4) assembly.

Subsequent addition of increasing amounts of CuTPPS4 (up to 9 equiv. in total) to the 3:4 (CuTPPS4:TC4) assembly produces initially steady increments of the absorbance and then (in the 9–12 range) a small hypochromic effect (purple section of trace (b) in **Fig.87**).

Accordingly, break-points A and B are compatible with the formation of a 6:4 and a 9:4 (CuTPPS4:TC4) assembly, both obtained as a result of complementary electrostatic interactions (sulfonate/ammonium) between the porphyrin molecules and the empty cavities of the outer layer of the tris-

calixarene molecules. Break-point C, on the other hand, indicates the formation of a discrete assembly where the newly added porphyrin molecules have most likely piled onto the three bridging CuTPPS4 units – present in the 9:4 species – ultimately yielding a 12:4 (CuTPPS4:TC4) assembly. Further incremental increase in the porphyrin concentration makes the slope of the titration curve grow again to eventually become almost identical to that detected for CuTPPS4 on its own (compare trace (a) with the black section of trace (b) in **Fig.87**), indicating that porphyrins in excess remain unbound in solution.

Overall, the sequence described so far allows the radial growth of tritopic calixarene/porphyrin assemblies to take place in a stepwise controlled fashion depending on the fine tuning of the two components added.

As an alternative to a radial/planar growth, the 3:1 (CuTPPS4:TC4) core assembly may also expand in height, providing an appropriate water-soluble calix[4]arene is supplied instead of tris-calix[4]arene TC4. According to **Fig.88**, addition of (R)- or (S)-C4 (up to 9 equiv.) to the 3:1 (CuTPPS4:TC4) complex does not induce any substantial change to the absorbance of the CuTPPS4 Soret band (compare the pertinent data-points represented by the first red circle of trace (b) and the blue square, respectively), suggesting the initial formation of a 3:1:9 (CuTPPS4:TC4:C4) assembly.

After this, consistent with the break-points observed in **Fig.88**, portion-wise addition of CuTPPS4 give rise to higher order aggregates (i.e., 6:1:9, 8:1:9, 10:1:9, 11:1:9 and 12:1:9 (CuTPPS4:TC4:C4) with porphyrins stacked above/below the three positively charged regions, formed after the addition of calix[4]arene (R)- or (S)-C4.

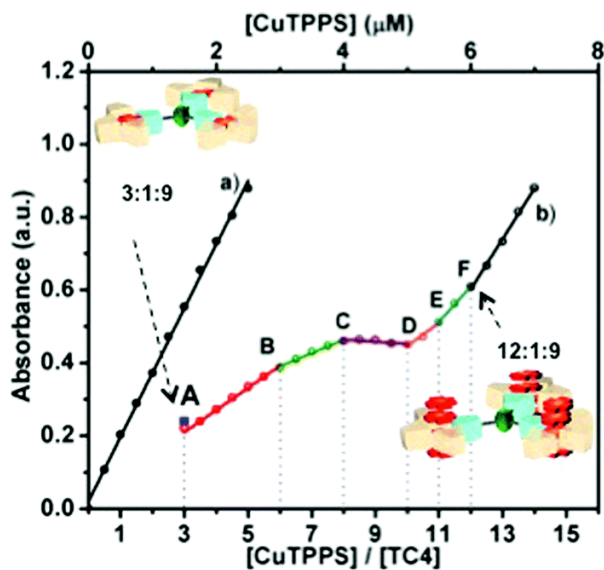


Fig.88 Variation in the absorbance of the CuTPPS4 Soret band ($\lambda_{max} = 412$ nm) observed upon: (i) increase of the porphyrin concentration in water (black trace a) and (ii) portion-wise addition of CuTPPS4 to a $0.5 \mu\text{M}$ aqueous solution of TC4 at pH 2 containing 9 equiv. of (S)-C4 (trace b). The changes in slope of trace (b) – corresponding to break-points A, B, C, D, E and F – indicate the ratio of the components at which the 3:1:9, 6:1:9, 8:1:9, 10:1:9, 11:1:9 and 12:1:9 (CuTPPS4:TC4:(S)-C4) assemblies, respectively, are fully formed. The data-point represented by the blue square, next to the red section of trace (b), refers to the absorption of the 3:1 (CuTPPS4:TC4) assembly.

Compared to the case of the radial growth (**Fig.86-right** and **Fig.87**), the hypochromic effect seen on the porphyrin Soret band upon portion-wise addition of CuTPPS4 to a solution of the 3:1:9 (CuTPPS4:TC4:C4) assembly is more pronounced. This difference stems from a more intense electronic communication between the stacked porphyrins and the peripheral C4 units present in the complex. Between the 8:1:9 and the 10:1:9 (CuTPPS4:TC4:C4) assemblies the hypochromic effect is more pronounced owing to the presence of additional porphyrin molecules that stack above/below the plain, increasing the electronic communication.

Once the 12:1:9 (CuTPPS4:TC4:C4) assembly has formed, further addition of porphyrin aliquots to the solution does not cause any optical variation

compatible with a further growth of the supramolecular assembly. Porphyrins added at this stage do not interact with the supramolecular aggregate present in solution and, as a result, the slope of the titration curve (black segment of trace b in **Fig.88**) matches the one observed in the case of CuTPPS4 on its own (trace a in **Fig.88**).

Furthermore, the use of enantiomerically pure calix[4]arenes (R)-C4 and (S)-C4 as supramolecular “*stoppers*” of the radial growth of our systems raised the question whether or not these species were able to induce chirality to the entire supramolecular aggregate.

Surprisingly and unlike earlier findings on the chiral induction mediated by C4 on the 1:4 (CuTPPS4:C4) complex,^[171] in the case of the 3:1:9 (CuTPPS4:TC4:(R)-C4) assembly, the presence of 9 molecules of (R)-C4 gives rise – in the porphyrin Soret region – to a very modest positive, induced circular dichroism (ICD) signal. This signal is shown in the inset to **Fig.89** (the mirror image seen in the same inset refers to the ICD signal detected upon addition of the (S)-C4 enantiomer).

This unexpected result is probably related to the inability of each porphyrin molecule to tightly interact with three chiral (R)- or (S)-C4 calixarene molecules while simultaneously bound to the sterically demanding tris-calixarene core.

On the other hand, addition of CuTPPS (3 equiv.) to the 3:1:9 (CuTPPS4/TC4/(R)-C4) assembly yields a new 6:1:9 (CuTPPS4/TC4/(R)-C4) species that displays an intense bisignate ICD signal in the porphyrin absorption region (**Fig.89**, solid black trace).

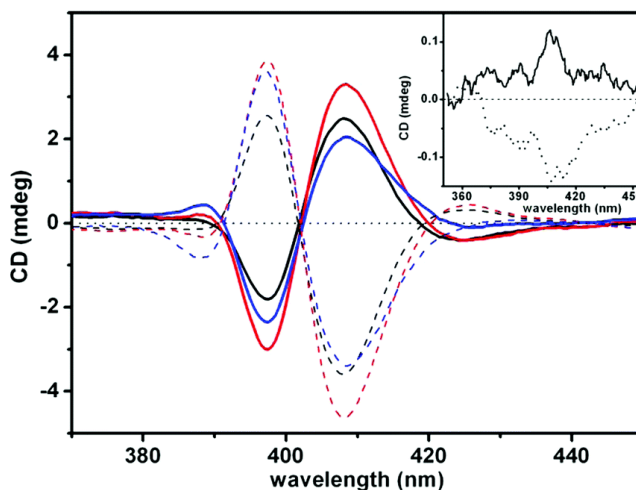


Fig.89 CD spectra of an aqueous solution (pH 2.5) of the 3:1:9 (CuTPPS4:TC4:(R)-C4) assembly ([TC4], [CuTPPS4] and [(R)-C4]: 1.5, 0.5 and 4.5 μ M, respectively; solid trace in the inset), the 6:1:9, 9:1:9 and 12:1:9 (CuTPPS4:TC4:(R)-C4) assemblies (black, red and blue traces, respectively; [CuTPPS4] was varied from 1.5 to 3.0, 4.5 and 6.0 μ M, respectively). Dashed traces (and the dotted one in the inset) refer to the same experiment carried out in the presence of the (S)-C4 enantiomer.

The intensity of this ICD signal reaches a maximum upon formation of the 9:1:9 (CuTPPS4/TC4/(R)-C4) assembly (**Fig.89**, solid red trace) and then in the 12:1:9 assembly almost halves, after a further aliquot of **CuTPPS** (3 moles) has been added (**Fig.89**, solid blue trace). A similar trend, but with mirror-image signals, is detected when (S)-C4 is added instead of (R)-C4 (**Fig.89**, dashed traces).

In agreement with the dramatic intensity enhancements of the ICD signal observed in **Fig.89**, our data suggest that the porphyrin stacking acts as a sort of “molecular glue” by strengthening the electronic communication between the achiral 3:1 (CuTPPS4:TC4) core complex and the chiral (R)- or (S)-C4 supramolecular stoppers. The intensity drop observed on moving from the 9:1:9 to the 12:1:9 (CuTPPS4:TC4:(R)-C4) assembly is attributable to the increasing distance between the chiral inducer ((R)-C4) and the outer layer of porphyrins added.

4.3

Final Remarks

In the first paragraph (chap. 4.2.1) we have shown that tri-sulfonate porphyrin (H_2DPPS3) and its metal-derivative ($CuDPPS3$), in the presence of ditopic calix[4]arene $BC4$ and *chiral*- $BC4-NH_2$, respectively, self-assembles in aqueous solution. The self-assembly of porphyrin/calixarene complexes follows strict hierarchical rules, in terms of sequence of reagents' addition and formation of specific final stoichiometry. In particular, we observed, for $H_2DPPS3:BC4$ complexes, exact break-points at 0.5:1, 2:1 and 4:1 [H_2DPPS3]:[$BC4$] by means of a step-wise titration at neutral pH.

Regardless, complexes with stoichiometry higher than 4:1 [H_2DPPS3]:[$BC4$] have not been achieved yet. On the contrary, a step-wise titration of both enantiomeric forms of $BC4-NH_2$ (*SS*- and *RR*-) with $CuDPPS3$ leads to break-points at 1.5:1, 2:1, 3.5:1 and 4:1 [$CuDPPS3$]:[*chiral*- $BC4$] confirmed as well by RLS measurements. The employment of $CuDPPS3$ with *chiral*- $BC4-NH_2$ rather than its free-base precursor is explained by the need to have acid pH values during the titration where else the H_2DPPS3 protonation occurs. Moreover, the chiral nature of (*RR*)- and (*SS*)- $BC4$ provides a quite simple strategy to induce chirality in $CuDPPS3:chiral-BC4$ complexes. The transfer of chirality has been demonstrated by monitoring the ICD signals throughout the titration. The 4:1 [$CuDPPS3$]:[*chiral*- $BC4$] complexes display the higher induced circular dichroism.

The presence of a β -sulfonate group in H_2DPPS3 and $CuDPPS3$ asks the question concerning its role in the self-assembly process with $BC4$. For this reason, a gradual titration of $BC4$ with di-sulfonate H_2DPPS2 was carried out, by

demonstrating a hierarchical and stoichiometric self-assembly, almost comparable to aforementioned complexes. Presumably, the β -sulfonate group acts as electrostatic stabilizer rather than as active part in the self-assembly.

Towards a major complexity is argument of the paragraph 4.2.2. Here, the bis-calix[4] tube, BC4T(K⁺) has been employed successfully to build 2D arrangements with the CuTPPS4 porphyrin. In particular, if the potassium ion is entrapped into the bis-calix cage, the BC4T will be blocked in the cone conformation. As a result, the reduced conformational equilibrium makes BC4T(K⁺) suitable to interact with CuTPPS4, achieving in turn, defined 3D or 2D complexes. In fact, the use of a di-topic calixarene with an oppositely charged tetra-topic porphyrin allows to build supramolecular structure whose growth in the space (i.e. 7:4-CuTPPS4:BC4T(K⁺) complex) or over the plane (that is 13:16-CuTPPS4:BC4T(K⁺) complex) depends on the addition's sequence of porphyrins and calix[4]arenes.

As such, the control of stoichiometry, sequence and dimensionality becomes essential when we desire to confer some precise electronic properties in all supramolecular complex. In this respect, paragraph 4.2.3 illustrates the possibility to convey chirality in a 2D multi-porphyrin/calixarene complex. Indeed, the hierarchical self-assembly of anionic MnTPPS4 and CuTPPS4 with cationic BC4-NH2 produces a planar mixed-complex (i.e. 1:4:4-MnTPPS4:BC4-NH2:CuTPPS4). The coordination of the chiral mono-calix[4]arene (namely chiral-C4) onto bis-calix[4]arenes' free cavities transmits chirality in the mixed-complex. Indeed, we observe optical activity in the Soret region of CuTPPS4 (external porphyrin) and MnTPPS4 (internal porphyrin), providing for the first time the evidence of a long-distance chiral transfer in porphyrin-calixarene complexes.

In paragraph 4.2.4, we have shown that tetra-sulfonate metallo-porphyrins (CuTPPS4, MnTPPS4 and NiTPPS4) in the presence of tripodal calixarene TC4,

bearing three tetra-ammonium-calix[4]arene subunits covalently linked to a tris-phenylamino central core, self-assemble.

However, unlike previously reported porphyrin/calixarene assemblies, the discrete 3:1 CuTPPS:TC4 complex formed here displays a TC4 unit acting as the central/inner molecular building-block. Formation of this 3:1 core complex as well as the following higher-order assemblies (up to the 12:4-(CuTPPS:TC4) species) is consistent with hierarchical (electrostatic sulfonate/ammonium over π - π interactions) and steric hindrance effects operating simultaneously. On the other hand, the radial growth of the 3:1 CuTPPS:TC4 complex can be deliberately prevented by adding appropriate supramolecular “*stoppers*” (e.g., (R)- and (S)-C4) and, as a result, the growth of the intermediate three-component assembly thus formed 3:1:9 (CuTPPS:TC4:C4) can be redirected. Further addition of porphyrin molecules, at this stage, forces the assembly to expand in height (3D stacked growth) by taking advantage of π - π interactions between porphyrin molecules. This alternate pathway is confirmed not only by UV-vis observations but also by the appearance of an intense bisignate ICD signal in the porphyrin absorption region. This last finding demonstrates that the addition of an enantiopure component ((R)- or (S)-C4) allows chirality to be transferred from the molecular to the supramolecular level.

In conclusion, we can affirm that calixarenes represents fascinating hosts to govern the porphyrins' aqueous self-assembly in terms of stoichiometry, sequence, dimensionality and electronic properties.

5. SECTION II: covalent approach

5.1

Covalent Organic Framework, Metal-organic Framework and Supramolecular Framework

The molecular synthesis of organic compounds has been dominated^[180] traditionally by kinetically controlled reactions, which result in the irreversible formation of (strong) covalent bonds. In this kind of synthetic chemistry, reagents, catalysts and conditions are chosen very carefully for the efficient production of a single product. In essence, a more favorable energetic pathway to the formation of a particular product, rather than other possible products, is usually the objective. The irreversible nature of the reaction guarantees that, once the particular product is formed, it is not possible either for the starting materials to be reformed from it or for it to be converted into another product (at least under the conditions of the reaction). In this manner, chemists have historically devised efficient syntheses of both natural and synthetic products.

Polymer chemistry is the clearest example how the organic synthesis meets the material science. Polymers are used in a wide range of applications, as coatings, as adhesives, as engineering and structural materials, for packaging and for clothing. A key feature of the success and versatility of these materials is that it is possible to build in properties by careful design of the (largely) organic molecules from which the chains are built up. There is now an increasing demand for highly specialized materials for use in for example optical and electronic applications and polymers have been singled out as having particular potential in this regard. For example, there is considerable interest in the development of polymers with targeted optical properties such as second-order optical

nonlinearity,^[181] and in conducting polymers as electrode materials, as a route towards supercapacitors^[182] and as electroluminescent materials.^[183]

However, a criticism associated to these porous polymers is the difficulty to synthesize a fully crystalline solid. Indeed, the formation of dense non-crystalline solids by linking building units (i.e. monomers) is expected to be thermodynamically favorable.^[22,184] In order to obtain a porous crystalline polymer, the covalent bonds should be reversible, allowing for *self-correction of defects*. This strategy it's also called *Dynamic Polymerization*.^[21]

Recently, an important development is the construction of polymeric porous solids, such as *crosslinked polymers*,^[185] *Covalent Organic Frameworks* (COFs), *Metal-Organic Framework* (MOFs)^[186–189] and *Supramolecular Organic Frameworks* (SOFs).^[190–192]

Here, the main difference between a conventional polymer and a novel porous framework: COFs, MOFs and SOFs are built from organic -or metal-organic and supramolecular- linkers via slightly reversible reactions.^[184,193,194] The reversible nature of such reactions permits the formation of a crystalline structure rather than an amorphous polymer, as it allows for error correction and rearrangement of the network by cleavage and reformation of connections within the lattice.^[194]

5.2

State-of-the-art

Covalent Organic Frameworks (COFs) represent a fascinating class of porous organic materials synthesized by polymerization of suitable organic building blocks through covalent bonds.^[193] The first COF was synthesized by the self-condensation of boronic acids to produce boroxine anhydride-based linkages in the form of B₃O₃ rings.^[195] Since their crystalline and porous structure, COFs are often called as “*organic zeolites*”. In principle, all synthetic routes employed in organic chemistry are useful for building organic frameworks.

The main classes of reactions are reported in **Fig.90**. The reaction A is based on a self-condensation of boronic acids; reaction B involves a condensation between boronic acids and catechols; in alternative, reaction C employs boronic acids and silanols; reaction D represents a nitrile cyclotrimerization; reactions E and F are based on the reversible formation of imine bonds (i.e. Schiff-base linkage). In particular, this latter reactions have been largely used to synthesize several COFs.^[24] In fact, COFs based on Schiff chemistry (or dynamic imine chemistry) own multiple advantages: numerous precursors available, enhanced chemical stability, interesting properties and applications.^[24,31,196]

Solvothermal synthesis is the most used method to prepare COFs based on Schiff-base chemistry.^[24,31] It consists of a reaction performed into a sealed Pyrex tube under inert atmosphere and high temperature (usually, between 85 °C and 120 °C) for several days.

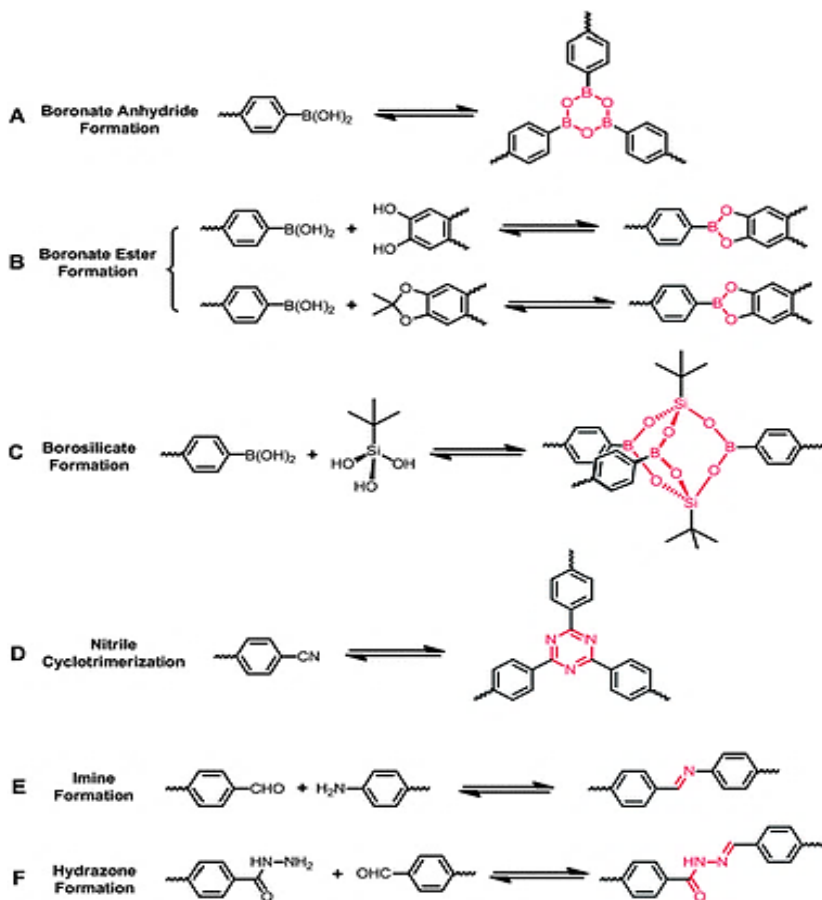


Fig.90 Most important condensations used in COFs synthesis.

The choice of the reaction temperature plays a key role since the condensation's reversibility depends on temperature conditions. The temperature is not the only crucial parameters, but even the solvents (or their combination) and the stoichiometric ratio can affect the reversibility of the reaction as much as COFs' crystallinity.^[24,193]

Concerning imine-based COFs, recently it has reported the first fast synthesis of a crystalline 2D COF, performed at room temperature, **RT-COF-1**.^[30]

The Schiff reaction, catalyzed by acid acetic at room temperature and in air, between two trigonal building blocks, 1,3,5-tris(4-aminophenyl)benzene (**TAPB**) and 1,3,5-benzenetricarbaldehyde (**BTCA**), in *m*-cresol or DMSO, leads to the formation of RT-COF-1, **Fig.91**.

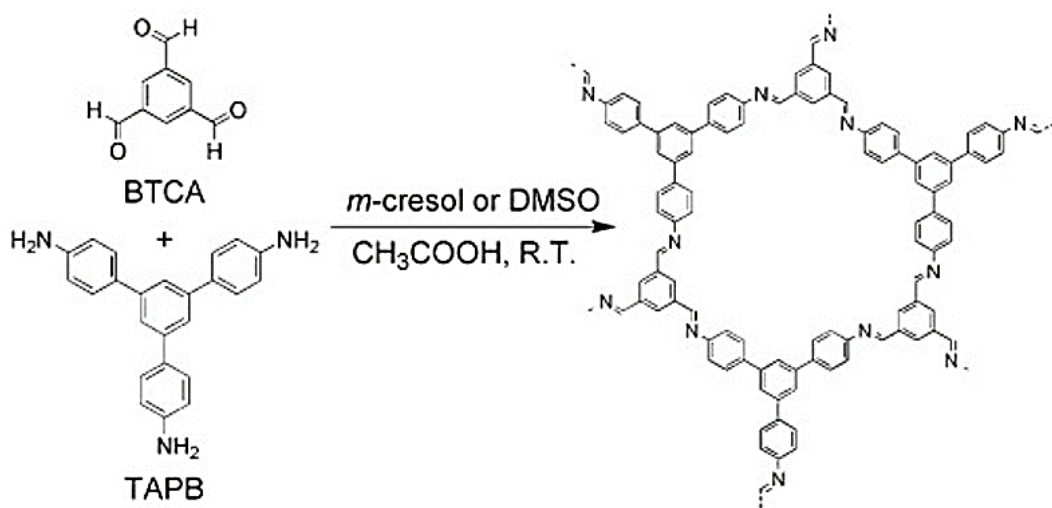


Fig.91 Schematic synthesis of RT-COF-1 from BTCA and TAPB.

Noteworthy, the formation of imine-based frameworks has required the use of high temperatures most of time. As a consequence, this synthesis at room temperature represents innovative advances in COFs chemistry.

RT-COF-1 is steady up to 450 °C, and also it exhibits crystallinity, laminar hexagonal structure and porosity (BET surface N₂ = 329 m² g⁻¹; BET surface CO₂ = 369 m² g⁻¹).

As a result of the easy tunable reaction, conducted under soft conditions, RT-COF-1 was successfully employed to realize direct on-surface patterning on rigid and flexible substrates by using both lithography-controlled wetting (LCW) and inkjet printing technologies.^[30] Moreover, the reaction between BTCA and

TAPB was performed under continuous microfluidic conditions to fabricate an highly crystalline framework, consisting of fibrillar micro-structures with a mechanical stability which allows for a direct 2D and 3D printing on a surface.^[23,63,197]

Although the progress in the synthetic routes has increasingly led to crystalline COFs, their synthesis often yields polycrystalline or amorphous products rather than single crystals. Single-crystal are needed for modeling the COFs nanostructure without resort to theoretical parameters which are often unattainable.^[198] A successfully strategy in order to obtain a 3D single-crystal COF was to increase the reversibility of imine bond formation and dissociation by means of the imine-exchange strategy. This was achieved by adding a large excess of aniline to the reaction mixture, where aniline functions as a modulator. Thus, the addition of aniline (in large excess) increases the overall concentration of amine in the reaction, enhancing the reversibility of imine bond formation and the process of error corrections, and ultimately, crystallization.^[198] Thanks to afore-mentioned strategy, Yaghi and co-authors were able to produce a single crystals of 3D COF-300 up to 100 μm in size within 30 - 40days.^[198]

As such, the supramolecular π - π interactions between single layer in a 2D COF (e.g. RT-COF-1) makes difficult to realize a single-crystal. In this context, a strategy to achieve a single-crystal of RT-COF-1 is highly desirable for unexpected findings that may open up.

Metal-organic Frameworks (MOFs), also called *porous coordination polymers* (PCPs), are coordination networks of metal complexes, often multinuclear species, with multifunctional organic ligands (i.e. linkers). In detail, these materials are constructed by joining metal-containing units with organic linkers, by using strong bonds to create open crystalline frameworks with

permanent porosity.^[188,189] The repeating coordination entities are usually metals or metal ions (clusters, multinuclear complexes) and organic multidentate ligands (linkers).^[189,199–201] The role of the cluster is to direct the coordinating linkers into predefined directions in space. Thus, they are often regarded as the “nodes” of the network.^[188,189,200] Some examples of inorganic *nodes* and organic *linkers* are shown in **Fig.92** below.

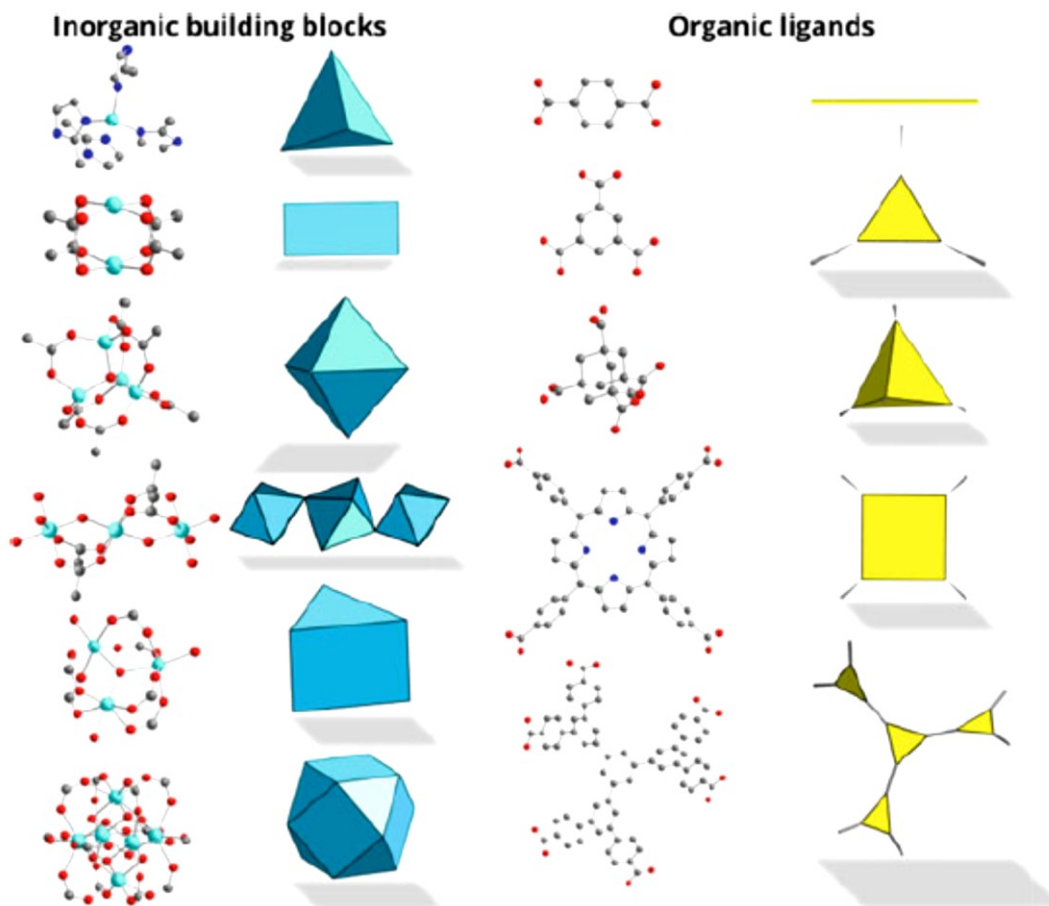


Fig.92 Prototypical examples of the inorganic building blocks and organic ligands, often used for the construction of MOFs.

The basic design principles of MOFs date back to the concept introduced by Robson in 1990, which relies on building block concept.^[202] However, thanks to Omar Yaghi in the early 2000s the concepts of “*reticular synthesis*,” and “*secondary building units*” (SBU) were widely employed to create ordered and porous frameworks.^[186] In essence, *reticular synthesis* can be described as the process of assembling judiciously designed rigid molecular building blocks into predetermined ordered structures (networks), which are held together by strong bonding. It is different from retrosynthesis of organic compounds, because the structural integrity and rigidity of the building blocks in reticular synthesis remain unaltered throughout the construction process—an important aspect that could help to realize fully the benefits of design in crystalline solid-state frameworks.^[186,188] Similarly, reticular synthesis should be strictly distinguished from supramolecular assembly, because in the former, building blocks are linked by strong bonds throughout the crystal.

Moreover, it is difficult (although not impossible) to attempt *a priori* synthesis of structures, such as those presented above, from simple metal ions and organic links because ions hold little directional information. This relative lack of directionality often results in flexibility around the metal ion.^[186] For this reason, Yaghi and co-workers successfully extrapolated the principle secondary building units (SBUs) to design rigid frameworks. The term *secondary building unit* has been used for some time to describe conceptual fragments of zeolites; in the context of reticular synthesis it refers to the geometry of the units defined by the points of extension of the *metal nodes*.^[186,188,189]

This approach, based on the concept of SBUs, has been useful in rationalizing the topologies of MOF structures and more importantly, it has allowed the synthesis and use of a large number of inorganic and organic SBUs with varying geometries. In many of these cases, identifying the reaction

conditions that produce an SBU with a specific geometry in situ means that the addition of a rigid organic SBU will result in the formation of a predetermined network. In other words, with this strategy it is now possible to control the overall coordination number of the inorganic and organic SBUs, and therefore the need to identify the networks that are expected to form from different geometric shapes becomes particularly acute.^[186,188,189]

In Japan, Susumu Kitagawa was among the early pioneers to explore the field of coordination polymers in the early 1990s starting with the synthesis and characterization of Cu- and Ag-based 1D coordination polymers.^[203]

In parallel in another part of the world, Omar Yaghi used squarates in the combination with Mn^{2+} and Zn^{2+} ions in the synthesis, resulting in compounds with hydrogen-bonded chains, sheets, and even 3D frameworks.^[204]

Later, the synthetic strategies for the construction of the porous solids were highlighted by applying a modular approach to a number of organic ligands and metal clusters resulted in numerous porous materials.^[205] Among them, the $Zn_4O(1,4\text{-benzenedicarboxylate})_3$, named as MOF-5 (**Fig.93**), was an absolute record holder in terms of porosity.^[206] Indeed, high gas storage capacity of MOF-5 was confirmed soon experimentally in cryogenic hydrogen physisorption experiment at 77 K, resulting in a record of 7.1 wt.% excess uptake at 40 bar.^[207]

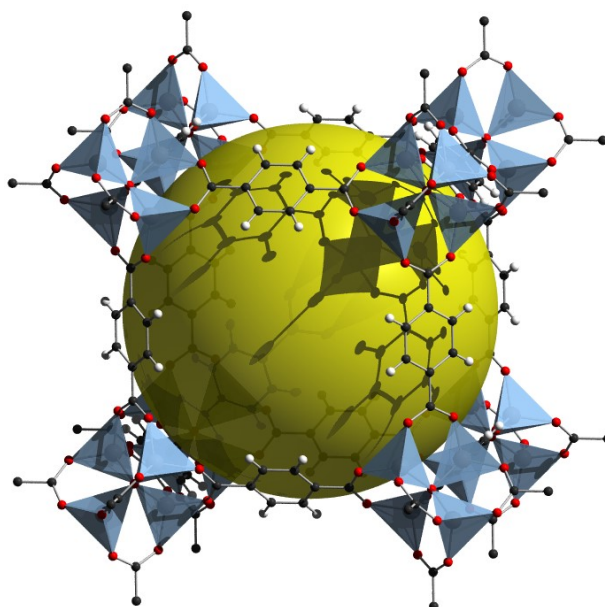


Fig.93 Unit cell structure of MOF-5. The yellow sphere represents the volume of the pore. Oxygen in red, carbon in black, and hydrogen in white. Tetrahedrons represent the coordination of 1,4-benzenedicarboxylate to the Zinc centre.

MOFs are usually synthesized via one-pot self-assembly reactions between ligands and metal salts in solutions between room temperature and 250 °C. Crystalline products, in particular single crystals large enough for single-crystal diffraction, are always desired in MOF synthesis. At near room temperature, the slow evaporation of solvents of a reaction solution or slow diffusion of solvent/solution to control the reaction rate and promote single crystals growth is often adopted. At higher temperature and pressures, generally termed solvothermal approach, reaction times are usually reduced, but single crystalline products are still observed. Controlling the reaction rate, by for example adjusting the pH value of the reaction solution, is always important to obtain high-quality crystalline products, and drive the formation of a kinetic over thermodynamic product, although this last area remains largely unstudied.^[201]

Nowadays, the lively interest to the MOF research is reflected in the constant development of new materials for gas storage^[208,209] and separation^[210] as well as heterogeneous catalysis^[199] and chemical sensors.^[200]

Another class of low-density porous organic crystalline materials is constituted by ***Supramolecular Organic Frameworks*** (SOFs). In respect with COFs and MOFs, SOFs can be defined as porous solid of two or more organic species held together exclusively by non-covalent interactions such as hydrogen-bonding, halogen-bonding, cation- π , π - π , or van der Waals interactions.^[190,191,211,212]

The scientific interest towards SOFs arises from the fact that the hydrothermal or solvothermal techniques for the preparation of traditional “*hard*” materials -COFs and MOFs- typically require high temperatures and long reaction times, which do not appear to provide a promising perspective for self-assembled regular *soft* architectures such as supramolecular frameworks.^[192] Conceptually, SOFs represent a special kind of supramolecular polymers that possess substantially increased structural regularity, which allows enhanced capacity of encapsulation.

Although the library of SOFs is still relatively small and in need of expansion, more examples of SOFs have begun to emerge to bring about unique functions.^[213] Most of the porous SOFs are crystallized with single component organic building blocks by varying different solvents, similar to preparing molecular crystals. The organic components within SOFs are closely packed to maximize the intermolecular interactions, and as a result the porosity in these crystals is often not spontaneous.^[191]

The formation of SOFs is mainly based on two important concepts: preorganization and multivalence, both of which are expected to enable stable

binding and ordering of the resulting supramolecular architectures. In this regard, the first homogeneous 2D SOF was reported in 2013, which utilized the hydrophobically driven encapsulation of the homodimers of the N-phenyl-4,4'-bipyridine (PBP) unit in the cavity of the cucurbit[8]uril (CB[8]) rings to periodically hold rigid triangular monomers together in 2D space (**Fig.94**).^[214] The CB[8]@(PBP)₂ encapsulation motif is one of the representative examples of host-guest chemistry, which have been employed widely for the construction of various supramolecular polymers in aqueous media.

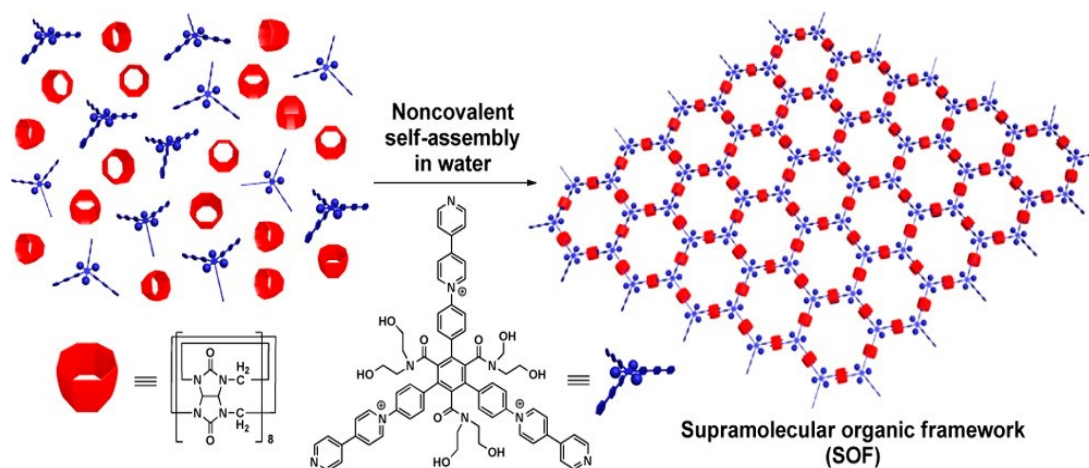


Fig.94 Schematic representation of the water self-assembly patterns of different building blocks with CB[8] in red and PBP in blue.

A similar strategy was employed in 2014 for the formation of a 3D homogeneous SOF. Here, the encapsulation in water of the tetrahedral derivative of 4-(4-methoxyphenyl)pyridin-1-ium by cucurbit[8]uril rings was reported (**Fig.95**).^[215]

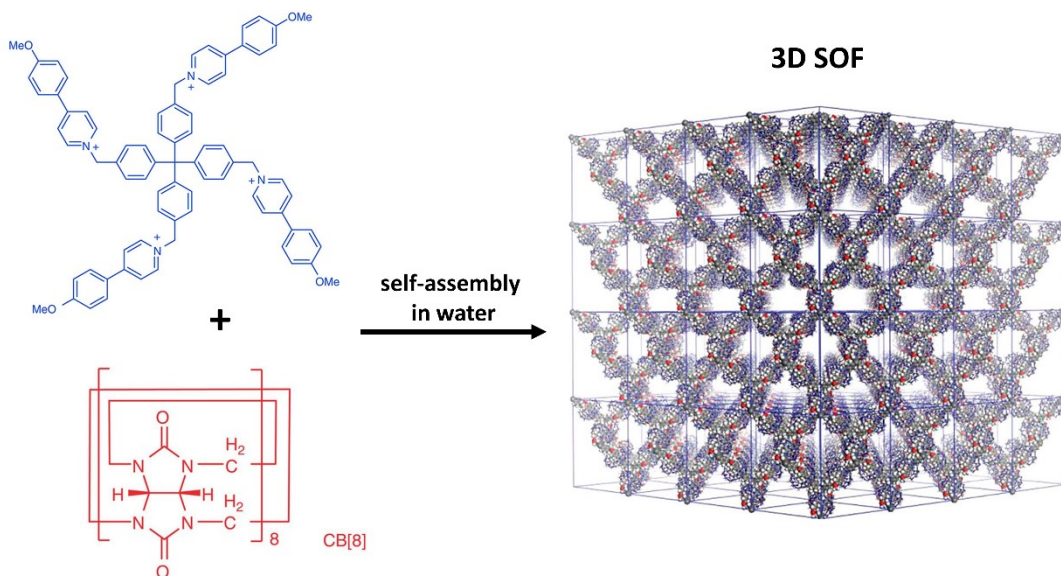


Fig.95 Illustration of the water self-assembly between the tetraprotic derivatives of 4-(4-methoxyphenyl)pyridin-1-ium and cucurbit[8]uril in order to realize a 3D SOF.

Both aforementioned SOFs (2D and 3D) are soluble in water but can also maintain their structural periodicity in the solid state. Noteworthy, the attempt to generate porosity in such materials by means of solvent removal may result in the collapse of the entire molecular assembly into a densely packed or an amorphous phase. However, careful selection of building blocks and meticulous engineering of the intermolecular interactions may afford a robust assembly which can withstand the removal of solvent molecules, forming a porous SOF.^[190,191]

The exploration of the functions of homogeneous SOFs is still at the early stage. Nevertheless, a number of SOFs already exhibit unique properties and functions. For example, Zhao and co-workers synthesized a SOF suitable as efficient fluorescent chemosensor for the detection of picric acid with high selectivity and sensitivity.^[216]

Zhang et al. found a supramolecular framework which exhibits modest antimicrobial activity against methicillin-resistant *Staphylococcus aureus*.^[217] Conversely, the capacity of 3D diamondoid and cubic SOFs for the adsorption of nitrogen was found to be very weak, which may be attributed to the polycationic nature of these frameworks.^[213] However, SOFs exhibit extremely strong capacity of adsorbing anionic organic guests, including dye, drug, peptide, DNA, anionic dendrimer, which can be rationalized on the basis of “*hard and soft acids and bases*” theory.^[213]

Nevertheless, the self-assembly conditions for the formation of these new organic porous materials are extremely mild. Such assembly has been only demonstrated in water but should not be limited to just water and could be extended to other solvents. This is in sharp contrast to the harsh solvothermal conditions for the generation of MOFs and COFs. 2D SOFs are more structurally diverse and have been revealed to exhibit interesting functions in tuning the fluorescence of conjugated segments and antimicrobial activity. As a result, a large family of homogeneous water-soluble porous SOFs may also be expected to find applications as biomedical materials in the future.^[213] Furthermore, the adsorption of anionic organic guests into the internal of 3D SOFs opens the door for exploiting new functions. Several other possibilities could be envisaged by modifications of the monomers and expansion of the pores of the framework.

5.3

Results and Discussions

The purpose of this chapter is to summarise the research activities which were conducted at Universidad Autónoma de Madrid, under the supervision of Prof. Félix Zamora. Noteworthy, all the following data are currently under further investigations. All reagents, solvents and catalysts employed in this chapter, were purchased by Sigma-Aldrich and used without further purification.

First of all, in order to become familiar regarding the organic synthesis of the RT-COF-1's building blocks, we carried out the synthesis of 1,3,5-tris-(4-aminophenyl)benzene (**TAPB**).

As shown in **Fig.96**, the synthesis of TAPB is a palladium-reduction of the corresponding nitro-precursor, the 1,3,5-tris-(4-nitrophenyl)benzene (**TNPB**).

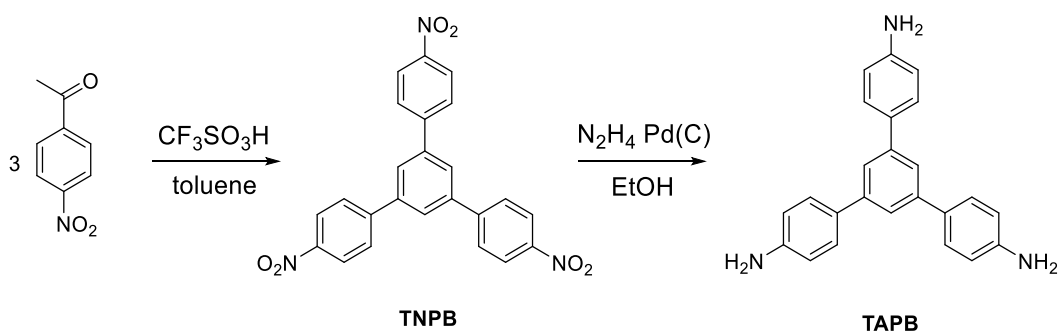


Fig.96 Schematic synthesis of 1,3,5-tris-(4-aminophenyl)benzene (**TAPB**).

In order to obtain the TNPB, trifluoromethanesulfonic acid (0.5 mL, 5.7 mmol) was added to a solution of p-nitroacetophenone (25 g, 152 mol) in toluene (100 mL). The solution was stirred under reflux in a Dean-Stark for 72 h. The

reaction mixture was then cooled with ice to obtain a black solid, which was filtered and washed with DMF in a soxhlet extractor until it turned yellow. 1,3,5-tris-(4-nitrophenyl)benzene was obtained with 75% yield. Afterwards, a suspension of 1,3,5-tris-(4-nitrophenyl)benzene (3 g, 6.8 mmol) and palladium on carbon (10 wt%, 0.7 g, 0.66 mmol Pd) in ethanol (120 mL) was heated until reflux. Then, hydrazine (60 wt%, 25 mL, 482 mmol) was added dropwise, and the mixture was refluxed for 10 h. The hot solution was filtered through celite and left undisturbed until a white product crystallized. The crystals of 1,3,5-tris-(4-aminophenyl)benzene were filtered and washed with cold ethanol. The product was obtained with 82% yield.

Moreover, we performed another synthesis, as shown in **Fig.97**, the triformylphloroglucinol (**TP**).

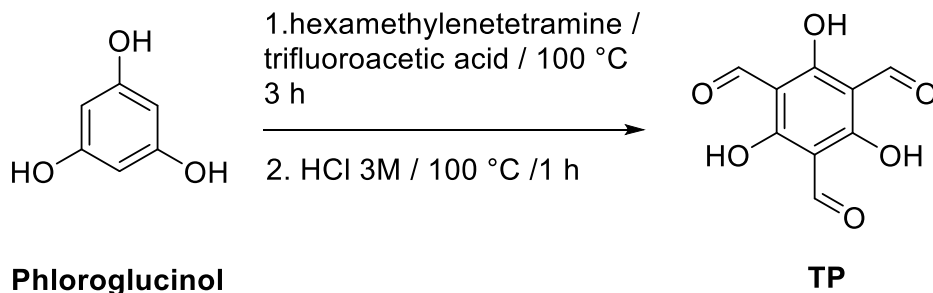


Fig.97 Schematic synthesis of triformylphloroglucinol, TP, (-right) starting from phloroglucinol (-left).

In order to obtain the TP, 90 mL trifluoroacetic acid was added to hexamethylenetetramine (15.098 g, 108 mmol) and dried *phloroglucinol*, 1,3,5-tris-hydroxybenzene, (6.014 g, 49 mmol) under inert atmosphere (Argon). The solution was heated at 100 °C for 3 h under distillation condition. Then, 150 mL of 3 M HCl was added and the solution was heated at 100 °C for 1 h. After cooling to room temperature, the solution was filtered through celite and extracted with

500 mL dichloromethane, dried over magnesium sulfate, and filtered. Rotary evaporation of the solution afforded 1.48 g (7.0 mmol, 14 %) of as an off-white powder.

Subsequently, we synthesized the **RT-COF-1**, as reported in **Fig.98**. However, the procedure to obtain the RT-COF-1 was carried out at room temperature. with an innovative gel-synthesis by using only acetic acid as solvent in comparison with the previous literature.^[30]

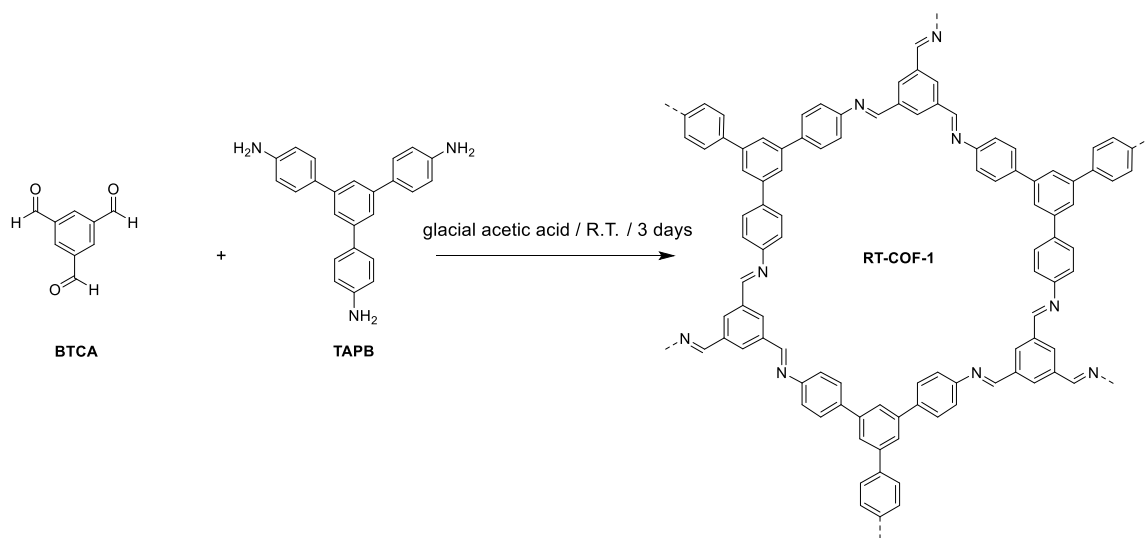


Fig.98 Schematic synthesis of RT-COF-1 in gel conditions at room temperature.

For this reason, 430 mg (1.23 mmol) of 1,3,5-tris(4-aminophenyl)benzene (**TAPB**) were dissolved in 30 mL of glacial acetic. On the other hand, 200 mg (1.23 mmol) of 1,3,5-benzenetricarbaldehyde (**BTCA**) were dissolved in another 30 mL of the same solvent. Both solutions were subsequently mixed at room temperature, under inert atmosphere (Ar) and the mixture was kept under stirring.

It was observed, almost immediately after the mixing, the formation of a yellow gel. Nevertheless, the reaction was conducted until 3 days. Afterwards,

the gel was repeatedly washed with ethanol and tetrahydrofurane and dried in air over 2 days. Finally, we achieved the yellow solid of RT-COF-1 (**Fig.99**).



Fig.99 Macroscopic yellow solid of RT-COF-1.

In order to characterize the RT-COF-1, we performed powder X-ray Diffraction, Scanning Electron Microscopy, IR Spectroscopy, and BET surface analysis. The powder XRD, reported in **Fig.100** displays a good crystallinity for the RT-COF-1 (black line) in comparison with the theoretical curve (red line) validated by a simulation software.

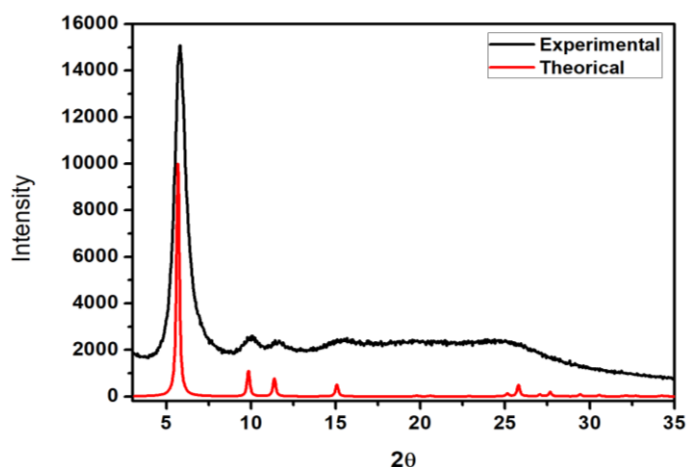


Fig.100 Powder X-Ray Diffraction of RT-COF-1 (experimental curve, black line; theoretical curve, red line).

The most significant changes in IR spectra (**Fig.101**) are the disappearance of N-H stretching bands between 3300-3500 cm^{-1} , related to the TAPB, the decrease of the intensity of C=O stretching band at 1689 cm^{-1} , connected to the BTCA, and the appearance of C=N stretching band at 1623 cm^{-1} , typical for imine bond of the RT-COF-1.

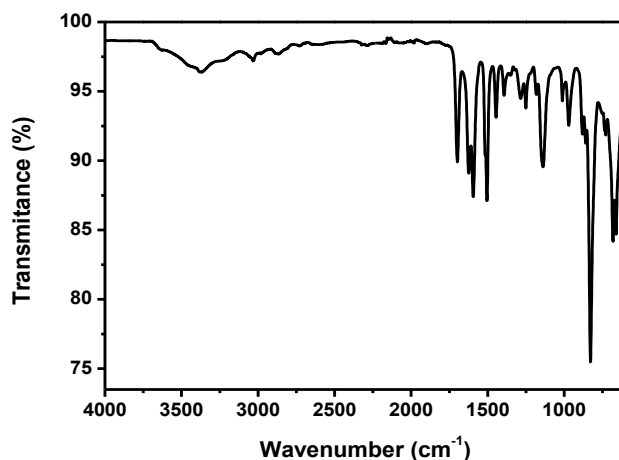


Fig.101 Experimental IR spectrum of RT-COF-1.

Conventional adsorption isotherms were measured using a Micromeritics Tristar 3000 volumetric instrument under continuous adsorption conditions, as shown in **Fig.102**. Brunauer-Emmet-Teller (BET) surface analysis[†] were carried out to determine the total specific surface areas for the N_2 isotherms at 77 K. Prior to measurement, powdered samples were heated at 423 K for 10 h and outgassed to 10^{-6} Torr. The fitting of the data to BET equation gives rise to a specific surface area S_{BET} of $705 \text{ m}^2\text{g}^{-1}$ while the fitting to Langmuir equation gives rise to a specific $S_{Langmuir}$ of $920 \text{ m}^2\text{g}^{-1}$.

[†] see *Appendix* for detailed description about BET surface analysis.

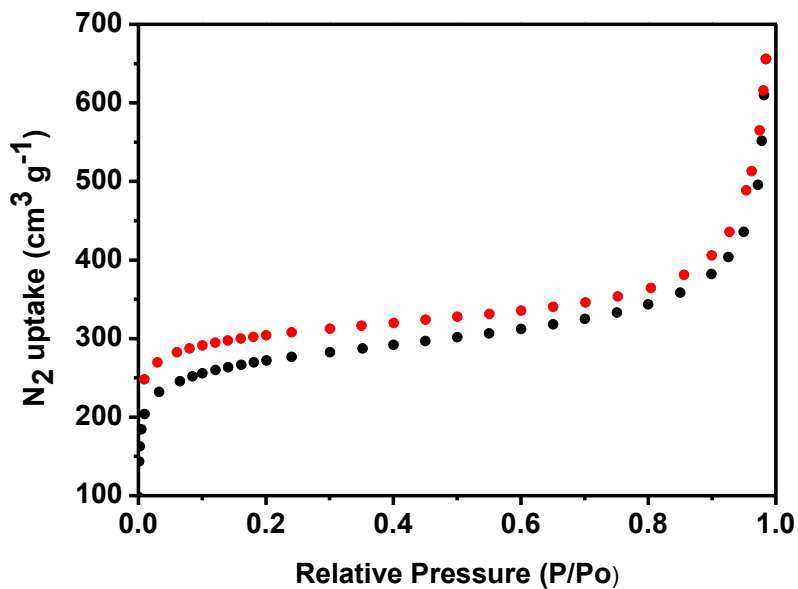
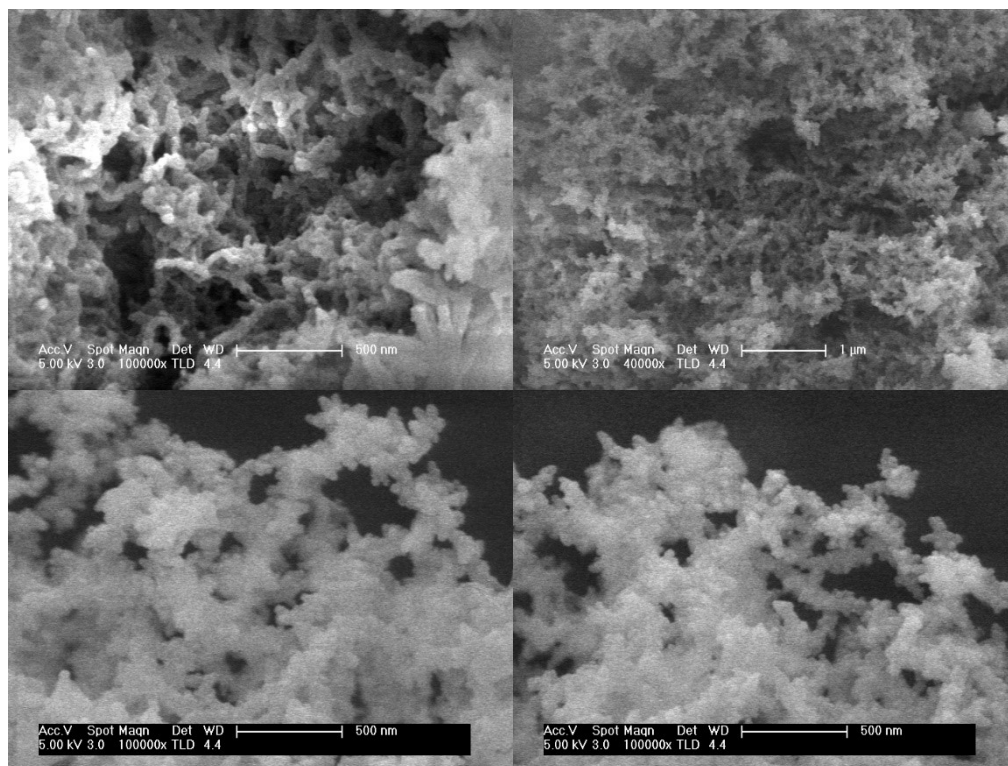


Fig.102 Experimental BET analysis for RT-COF-1 (N₂, 77K): adsorption cycle in black dots and desorption cycle in red dots.

As a result, the large surface area is also confirmed by SEM images (see below in **Figs.103** where we can denote a highly porous structure for the RT-COF-1).



Figs.103 SEM images of RT-COF-1.

Furthermore, we tested the performance of the RT-COF-1 in adsorption of dye pollutants from water. Indeed, dyeing effluent is one of the largest contributors to textile field and such wastewater has a seriously destructive impact on the human health. In this respect, dyes such as malachite green, *MG*, (**Fig.104**, $\lambda_{max} = 616$ nm), have been found to be useful in many industrial applications. Malachite green is highly effective against important protozoal and fungal infections, and aquaculture industries have been using MG extensively as a topical treatment by bath or flush methods. In addition, it is also used as a food coloring agent, food additive, and a medical disinfectant and anthelmintic as well as a dye in silk, wool, jute, and leather cotton, paper and acrylic industries.^[218]

To prevent dyes discharge and contamination, the removal of dyes from aqueous environment various methods have been reported. Among these, the adsorption technique is very attractive because of its high efficiency, simplicity of design, and ease of operation.^[218,219]

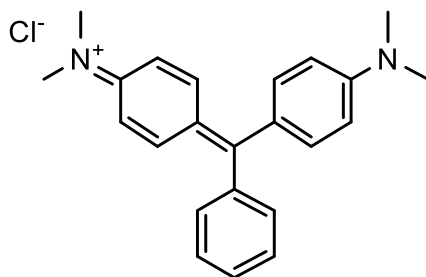


Fig.104 Molecular structures of malachite green, MG.

We carried out the adsorption experiments (**Fig.105**) by preparing three MG water solutions with different initial concentrations (0.05 mg/ml – 0.025 mg/ml – 0.0125 mg/ml). Then, 20 ml of each solution was added with 5 mg di RT-COF-1 (solid) and it was monitored the Uv-Vis absorption at 616 nm vs. time (**Fig.105**). Noteworthy, all the solutions were kept in a thermostatically-controlled water bath at 25 °C throughout the experiment; it was also used a calibration curve to convert the abs values of MG at 616 nm in concentration, expressed as mg/ml.

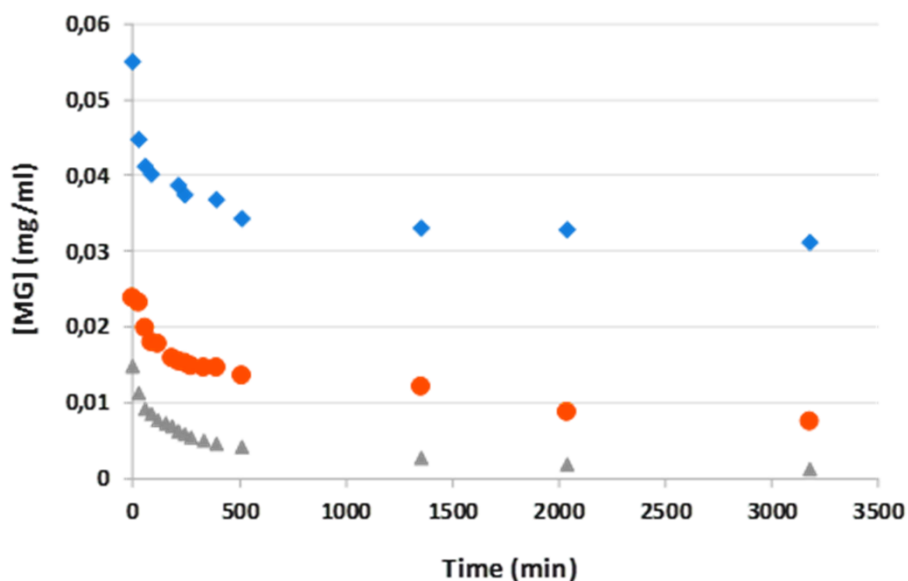


Fig.105 Adsorption curves vs. time for RT-COF-1 (5 mg) in presence of different initial concentration of malachite green (0.05 mg/ml, blue squares; 0.025 mg/ml, orange dots; 0.0125 mg/ml, grey triangles), 25°C.

To quantify the sorption capacity of sorbent for MG sorption, the *Langmuir* equation has been adopted to comment these data. In particular, the *Langmuir Isotherm Model* is valid for monolayer adsorption onto a surface with a finite number of identical sites. It is represented in the following form:^[218]

$$\frac{1}{q_e} = \frac{1}{q_{max}} + \frac{1}{q_{max}b} \frac{1}{c_e}$$

where q_e is the amount of MG adsorbed at equilibrium (in mmol g⁻¹), c_e is the residual concentration of MG at equilibrium (in g L⁻¹), q_{max} is the maximum adsorption at monolayer coverage (in mmol g⁻¹) and b is the Langmuir adsorption equilibrium constant (L mmol⁻¹), reflecting the energy of adsorption.

Without getting too much into the method of calculation, we succeeded in calculating the maximum adsorption q_{max} for the system RT-COF-1/MG equal to **4.94 mg MG / g COF**.

Moreover, another ongoing project is to prepare a single-crystal of the above-mentioned **RT-COF-1** and **COF-LZU1**. This goal is highly interesting because, so far, we don't have any example in literature of single-crystal for *2D* COF

In particular, the **COF-LZU1** was synthesized for the first time from BTCA and *p*-phenylenediamine solvothermal conditions by using 1,4-dioxane as solvent and acetic acid as catalyst.^[220] On the other hand, we tried to reproduce the same synthesis at room temperature as reported in **Fig.106**.

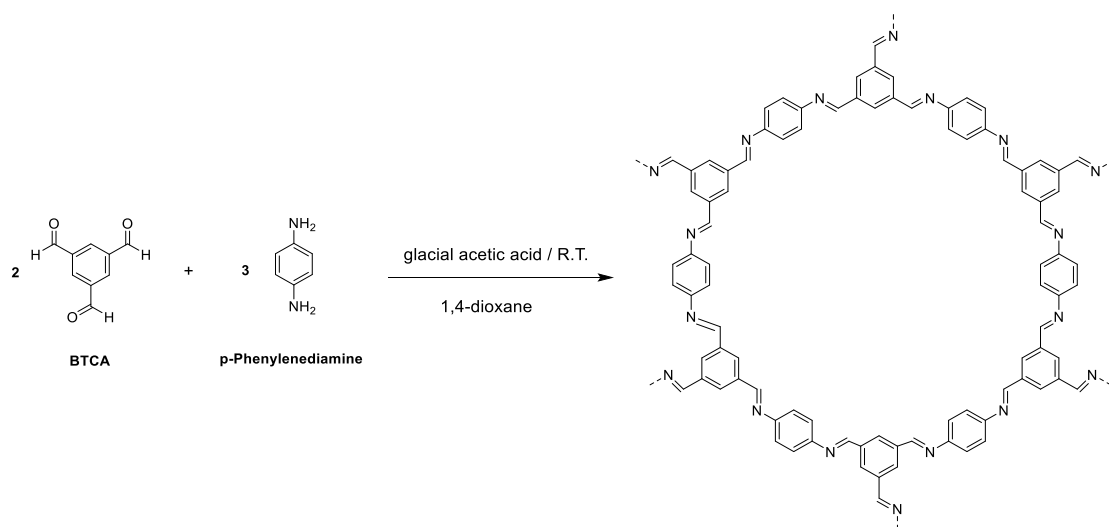


Fig.106 Schematic synthesis of COF-LZU1.

As previously reported, the presence of a large excess of aniline during the imine-condensation acts as a *modulator*, increasing the reversibility of imine-bond. As a consequence, the self-error corrections occur, involving a major crystallization.^[198] Nevertheless, further parameters such as solvents or stoichiometric appear decisive to determine the COFs' crystallinity.

For this reason, in order to synthesize a single-crystal of RT-COF-1, we prepared several vials under inert atmosphere (Ar) as described in **Table 1**.

Notably, every vial was filled up with the same volume of *i*) glacial acid acetic (100 μL), *ii*) BTCA dissolved in 1,4-dioxane (500 μL), *iii*) TAPB dissolved in 1,4-dioxane (500 μL); the added volume of aniline is reported in **Table 1**.

No. Vial	BTCA (mmol)	TAPB (mmol)	aniline(μL)	No. Vial	BTCA (mmol)	TAPB (mmol)	aniline(μL)
1	0.0617	0.0617	200	6	0.031	0.031	200
2	0.0617	0.0617	400	7	0.031	0.031	400
3	0.0617	0.0617	600	8	0.031	0.031	600
4	0.0617	0.0617	800	9	0.031	0.031	800
5	0.0617	0.0617	900	10	0.031	0.031	900
No. Vial	BTCA (mmol)	TAPB (mmol)	aniline(μL)	No. Vial	BTCA (mmol)	TAPB (mmol)	aniline(μL)
11	0.0154	0.0154	200	16	0.0077	0.0077	200
12	0.0154	0.0154	400	17	0.0077	0.0077	400
13	0.0154	0.0154	600	18	0.0077	0.0077	600
14	0.0154	0.0154	800	19	0.0077	0.0077	800
15	0.0154	0.0154	900	20	0.0077	0.0077	900
No. Vial	BTCA (mmol)	TAPB (mmol)	aniline(μL)				
21	0.0039	0.0039	200				
22	0.0039	0.0039	400				
23	0.0039	0.0039	600				
24	0.0039	0.0039	800				
25	0.0039	0.0039	900				

Table 1 Scheme for single crystal of RT-COF-1.

On the contrary, to synthesize a single-crystal of COF-LZU-1, we also prepared several vials under inert atmosphere (Ar) as reported in **Table 2**. Here, every vial was filled up with the same volume of *i*) glacial acid acetic (100 μL), *ii*) BTCA dissolved in 1,4-dioxane (500 μL), *iii*) p-phenylenediamine dissolved in 1,4-dioxane (500 μL); the added volume of aniline is reported in **Table 2**.

No. Vial	BTCA (mmol)	p-phenylenediamine (mmol)	aniline(μL)	No. Vial	BTCA (mmol)	p-phenylenediamine (mmol)	aniline(μL)
1	0.0617	0.0925	200	6	0.031	0.046	200
2	0.0617	0.0925	400	7	0.031	0.046	400
3	0.0617	0.0925	600	8	0.031	0.046	600
4	0.0617	0.0925	800	9	0.031	0.046	800
5	0.0617	0.0925	900	10	0.031	0.046	900

5.3 Results and Discussions

No. Vial	BTCA (mmol)	p-phenylenediamine (mmol)	aniline(μ L)	No. Vial	BTCA (mmol)	p-phenylenediamine (mmol)	aniline(μ L)
11	0.0154	0.023	200	16	0.0077	0.0115	200
12	0.0154	0.023	400	17	0.0077	0.0115	400
13	0.0154	0.023	600	18	0.0077	0.0115	600
14	0.0154	0.023	800	19	0.0077	0.0115	800
15	0.0154	0.023	900	20	0.0077	0.0115	900

No. Vial	BTCA (mmol)	p-phenylenediamine (mmol)	aniline(μ L)
21	0.0039	0.0058	200
22	0.0039	0.0058	400
23	0.0039	0.0058	600
24	0.0039	0.0058	800
25	0.0039	0.0058	900

Table 2 Scheme for single crystal of COF-LZU-1.

The vials tabulated in **Table 1** and **Table 2** were kept at room temperature and in the dark for several days. Indeed, the reactions in presence of a large excess of aniline require up to 40-50 days. This study is ongoing, and for this reason we have not observed appreciable results yet.

5.4

Final Remarks

Herein, I reported my research activity conducted at Universidad Autónoma de Madrid. In particular, I have synthesized two building blocks useful for the formulation of covalent organic frameworks: 1,3,5-tris-(4-aminophenyl)benzene, TAPB and triformylphloroglucinol, TP.

Afterwards, we performed the synthesis of RT-COF-1 by using the condensation between 1,3,5-benzenetricarbaldehyde, BTCA, and TAPB at room temperature (RT), in gel-phase and glacial acetic acid as catalysts and solvent. The XRD and IR analysis were employed to characterize the RT-COF-1. Moreover, SEM showed a high specific surface area which was confirmed to be equal to $705 \text{ m}^2\text{g}^{-1}$ through BET measurements.

Nevertheless, high surface area allows for use in the adsorption of dye pollutants from wastewater. The malachite green, MG, was used to perform adsorption experiments, reaching a maximum adsorption capability to 4.94 mg of MG per gram of RT-COF-1.

Moreover, we are currently investigating the chance to realize a 2D COF single-crystal for RT-COF-1 and COF-LZU1 by optimizing various parameters, among them, the use of aniline as imine-condensation modulator.

6.

Conclusions and Perspectives

In this thesis I summarized the results and findings obtained about porphyrin-based nanostructure examining in depth the two-fold role of noncovalent (*section I*) and covalent (*section II*) interactions in governing the porphyrin self-aggregation.

Herein, I have illustrated the concepts concerning the supramolecular approach to realize porphyrin nanostructures in aqueous solution (*chap.2*). In particular, we performed a fully spectroscopic investigations on the role played by polyelectrolytes to affect the porphyrin self-assembly. We succeeded in modulating the self-aggregation of the ZnTPPS4 when interacts with cationic poly-L-lysine (*chap.3*). Moreover, under acid conditions ($\text{pH} < 1.5$) the demetallation/protonation of ZnTPPS4 occurs, triggering formation of related *J*-aggregates. In particular, long poly-L-lysine chains lead to a more ordered *J*-aggregates compared to short chains.

Moreover, porphyrin non-covalent syntheses based on polypeptide templates show significant restriction due to ungovernable aggregation in terms of stoichiometry and dimensionality. For this reason, we demonstrated that host-guest interactions between porphyrins (as guests) and calix[4]arenes (as hosts) represents a valid strategy to dominate the aggregation phenomena (*chap.4*). The use of ditopic porphyrins (i.e. H₂DPPS3/H₂DPPS2 and CuDPPS3) in combination with ditopic calix[4]arenes (i.e. BC4 and chiral BC4-NH₂) allow to build 1D complexes of modulable chirality. A major complexity is reached thanks to the employment of CuTPPS4 and bis-calix tube: here, the system evolve towards self-assembled 2D structure.

Nevertheless, the control of an important electronic property, the *chirality*, is further achieved in 2D *mixed*-complexes MnTPPS4/CuTPPS4-BC4-NH2 by means of the addition of chiral calix[4]arenes to pre-formed 5:4 (multi-porph : biscalix) complexes.

Towards 2D/3D nanostructures is subject of the last chapter of *section I*: the tritopic calix TC4 permits to build CuTPPS4-TC4 complexes with an unique 3D radial shape. Most striking, the use of chiral C4 as “*stoppers*” lead to a considerable chirality in the entire complex.

Finally, we demonstrated how the supramolecular forces are able to govern the porphyrin aggregation (switching from 1D to 2D and 3D) and their electronic properties.

In the second section, I illustrated the synthetic approach to achieve a Covalent Organic Framework. We explored a new gel-synthesis to obtain a porous and crystalline RT-COF-1. We carried out a complete characterization and in addition, RT-COF-1 was successfully employed in removing of dye pollutants from water. Another ongoing project about COF single-crystal evidences how the parameter tuning is able to influence the final properties of the COF. Overall, these studies address the matter of covalent synthesis and related aspects.

In conclusion, a clear comprehension of the phenomena underlying the supramolecular and covalent approach paves the way to develop a combined strategy. In perspective, a combined approach may lead to generate complex nanostructure both in liquid and solid state, with control of dimensionality, crystallinity and feature for practical applications.

References

- [1] G. M. Whitesides, J. P. Mathias, C. T. Seto, *Science (80-.)*. **1991**, *254*, 1312–1319.
- [2] M. Bawendi, *Annu. Rev. Phys. Chem.* **1990**, *41*, 477–496.
- [3] A. Biswas, I. S. Bayer, A. S. Biris, T. Wang, E. Dervishi, F. Faupel, *Adv. Colloid Interface Sci.* **2012**, *170*, 2–27.
- [4] A. J. Blake, N. R. Champness, P. Hubberstey, W. S. Li, M. A. Withersby, M. Schröder, *Coord. Chem. Rev.* **1999**, *183*, 117–138.
- [5] S. Zhang, *Nat. Biotechnol.* **2003**, *21*, 1171–1178.
- [6] K. Baek, I. Hwang, I. Roy, D. Shetty, K. Kim, *Acc. Chem. Res.* **2015**, *48*, 2221–2229.
- [7] J.-M. Lehn, *Supramolecular Chemistry*, Vch, Weinheim Germany, **1995**.
- [8] J. -M Lehn, *Angew. Chemie Int. Ed. English* **1988**, *27*, 89–112.
- [9] C. J. Medforth, Z. Wang, K. E. Martin, Y. Song, J. L. Jacobsen, J. A. Shelnutt, *Chem. Commun.* **2009**, 7261–7277.
- [10] C. M. Drain, A. Varotto, I. Radivojevic, *Chem. Rev.* **2009**, *109*, 1630–1658.
- [11] I. Goldberg, *CrystEngComm* **2008**, *10*, 637–645.
- [12] P. D. Frischmann, K. Mahata, F. Würthner, *Chem. Soc. Rev.* **2013**, *42*, 1847–1870.
- [13] D. Monti, S. Nardis, M. Stefanelli, R. Paolesse, C. Di Natale, A. D’Amico, *J. Sensors* **2009**, *2009*, 1–10.
- [14] L. Zhao, M. Liu, S. Li, A. Li, H. An, H. Ye, Y. Zhang, *J. Mater. Chem. C* **2015**, *3*, 3650–3658.
- [15] L. Zhang, M. Liu, *J. Phys. Chem. B* **2009**, *113*, 14015–14020.
- [16] A. D’Urso, M. E. Fragalà, R. Purrello, *Chem. Commun.* **2012**, *48*, 8165.
- [17] J. Z. Zhang, Z. lin Wang, J. Liu, S. Chen, G. yu Liu, *Self-Assembled*

-
- Nanostructures*, Springer Science & Business Media, **2003**.
- [18] A. D'Urso, N. Marino, M. Gaeta, M. S. Rizzo, D. A. Cristaldi, M. E. Fragalà, S. Pappalardo, G. Gattuso, A. Notti, M. F. Parisi, et al., *New J. Chem.* **2017**, *41*, 8078–8083.
- [19] R. Purrello, E. Bellacchio, S. Gurrieri, R. Lauceri, A. Raudino, L. M. Scolaro, A. M. Santoro, *J. Phys. Chem. B* **1998**, *102*, 8852–8857.
- [20] M. Gaeta, I. Pietro Oliveri, M. E. Fragalà, S. Failla, A. D'Urso, S. Di Bella, R. Purrello, *Chem. Commun.* **2016**, *52*, 8518–8521.
- [21] S. J. Rowan, S. J. Cantrill, G. R. L. Cousins, J. K. M. Sanders, J. F. Stoddart, *Angew. Chemie Int. Ed.* **2002**, *41*, 898–952.
- [22] A. Ravve, *Principles of Polymer Chemistry*, Springer Science & Business Media, **2013**.
- [23] L. Garzón-Tovar, C. Avci-Camur, D. Rodríguez-San-Miguel, I. Imaz, F. Zamora, D. MasPOCH, *Chem. Commun.* **2017**, *53*, 11372–11375.
- [24] J. L. Segura, M. J. Mancheño, F. Zamora, *Chem. Soc. Rev.* **2016**, *45*, 5635–5671.
- [25] P. Albacete, J. I. Martínez, X. Li, A. López-Moreno, S. Mena-Hernando, A. E. Platero-Prats, C. Montoro, K. P. Loh, E. M. Pérez, F. Zamora, *J. Am. Chem. Soc.* **2018**, DOI 10.1021/jacs.8b07450.
- [26] J. Romero, D. Rodríguez-San-Miguel, A. Ribera, R. Mas-Ballesté, T. F. Otero, I. Manet, F. Licio, G. Abellán, F. Zamora, E. Coronado, *J. Mater. Chem. A* **2017**, *5*, 4343–4351.
- [27] C. Montoro, D. Rodríguez-San-Miguel, E. Polo, R. Escudero-Cid, M. L. Ruiz-González, J. A. R. Navarro, P. Ocón, F. Zamora, *J. Am. Chem. Soc.* **2017**, *139*, 10079–10086.
- [28] M. Gaeta, R. Randazzo, D. A. Cristaldi, A. D'Urso, R. Purrello, M. E. Fragalà, *J. Porphyr. Phthalocyanines* **2017**, *21*, 426–430.
- [29] M. Gaeta, D. Raciti, R. Randazzo, C. M. A. Gangemi, A. Raudino, A.

-
- D'Urso, M. E. Fragalà, R. Purrello, *Angew. Chemie - Int. Ed.* **2018**, *57*, 10656–10660.
- [30] A. Delapeñarui Gómez, D. Rodríguez-San-Miguel, K. C. Stylianou, M. Cavallini, D. Gentili, F. Liscio, S. Milita, O. M. Roscioni, M. L. Ruiz-González, C. Carbonell, et al., *Chem. - A Eur. J.* **2015**, *21*, 10666–10670.
- [31] D. Rodriguez-San-Miguel, P. Amo-Ochoa, F. Zamora, *Chem. Commun.* **2016**, *52*, 4113–4127.
- [32] E. D. Sloan Jr., C. A. Koh, C. A. Koh, *Clathrate Hydrates of Natural Gases*, CRC Press, **2007**.
- [33] C. A. Koh, E. D. Sloan, A. K. Sum, D. T. Wu, *Annu. Rev. Chem. Biomol. Eng.* **2011**, *2*, 237–257.
- [34] K. C. Hester, P. G. Brewer, *Ann. Rev. Mar. Sci.* **2009**, *1*, 303–327.
- [35] D. E. Koshland, *Angew. Chemie Int. Ed.* **1994**, *33*, 2375–2378.
- [36] J.-P. Behr, *The Lock-and-Key Principle, The State of the Art--100 Years On (Tom 17 Perspectives in Supramolecular Chemistry)*, John Wiley & Sons, **2008**.
- [37] A. Eschenmoser, *Angew. Chemie Int. Ed. English* **1995**, *33*, 2363.
- [38] L. Jean-Marie, *Angew. Chemie Int. Ed. English* **1990**, *29*, 1304–1319.
- [39] J. W. Steed, J. L. Atwood, *Supramolecular Chemistry*, John Wiley & Sons, **2013**.
- [40] J. W. Steed, D. R. Turner, K. Wallace, *Core Concepts in Supramolecular Chemistry and Nanochemistry*, John Wiley & Sons, **2007**.
- [41] A. I. Day, R. J. Blanch, A. P. Arnold, S. Lorenzo, G. R. Lewis, I. Dance, *Angew. Chemie - Int. Ed.* **2002**, *41*, 275–277.
- [42] P. J. Cragg, *A Practical Guide to Supramolecular Chemistry*, Wiley Online Library, **2005**.
- [43] L. F. Lindoy, I. M. Atkinson, J. F. Stoddart, *Self-Assembly in Supramolecular Systems*, Royal Society Of Chemistry, **2000**.

-
- [44] R. Paolesse, D. Monti, S. Nardis, C. Di Natale, in *Handb. Porphyr. Sci. (Volume 12) With Appl. to Chem. Physics, Mater. Sci. Eng. Biol. Med.*, World Scientific, **2011**, pp. 121–225.
- [45] C. Di Natale, D. Monti, R. Paolesse, *Mater. Today* **2010**, *13*, 46–52.
- [46] G. De Luca, G. Pollicino, A. Romeo, L. M. Scolaro, *Chem. Mater.* **2006**, *18*, 2005–2007.
- [47] F. G. Gulino, R. Lauceri, L. Frish, T. Evan-Salem, Y. Cohen, R. De Zorzi, S. Geremia, L. Di Costanzo, L. Randaccio, D. Sciotto, et al., *Chem. - A Eur. J.* **2006**, *12*, 2722–2729.
- [48] J.-M. Lehn, *Eur. Rev.* **2009**, *17*, 263–280.
- [49] J. D. Badjić, A. Nelson, S. J. Cantrill, W. B. Turnbull, J. F. Stoddart, *Acc. Chem. Res.* **2005**, *38*, 723–732.
- [50] A. Whitty, *Nat. Chem. Biol.* **2008**, *4*, 435–439.
- [51] R. W. Taylor, R. Ara Begum, V. W. Day, K. Bowman-James, *Supramol. Chem.* **2012**, DOI 10.1002/9780470661345.smc007.
- [52] D. J. Cram, *Angew. Chemie Int. Ed. English* **1986**, *25*, 1039–1057.
- [53] A. R. Peacocke, J. N. H. Skerrett, *Trans. Faraday Soc.* **1956**, *52*, 261–279.
- [54] J. D. McGhee, P. H. von Hippel, *J. Mol. Biol.* **1974**, *86*, 469–489.
- [55] R. Lauceri, M. De Napoli, A. Mammana, S. Nardis, A. Romeo, R. Purrello, *Synth. Met.* **2004**, *147*, 49–55.
- [56] M. De Napoli, S. Nardis, R. Paolesse, M. G. H. Vicente, R. Lauceri, R. Purrello, *J. Am. Chem. Soc.* **2004**, *126*, 5934–5935.
- [57] C. Escudero, A. D’Urso, R. Lauceri, C. Bonaccorso, D. Sciotto, S. Di Bella, Z. El-Hachemi, J. Crusats, J. M. Ribó, R. Purrello, *J. Porphyr. Phthalocyanines* **2010**, *14*, 708–712.
- [58] C. M. A. Gangemi, R. Randazzo, M. E. Fragalà, G. A. Tomaselli, F. P. Ballistreri, A. Pappalardo, R. M. Toscano, G. Trusso Sfrazzetto, R. Purrello, A. D’Urso, *New J. Chem.* **2015**, *39*, 6722–6725.

-
- [59] D. J. Vandijken, J. M. Beierle, M. C. A. Stuart, W. Szymański, W. R. Browne, B. L. Feringa, *Angew. Chemie - Int. Ed.* **2014**, *53*, 5073–5077.
- [60] R. B. Prince, J. S. Moore, L. Brunsveld, E. W. Meijer, *Chem. Eur. J.* **2001**, *7*, 4150–4154.
- [61] M. M. Green, M. P. Reidy, R. J. Johnson, G. Darling, D. J. O’Leary, G. Willson, *J. Am. Chem. Soc.* **1989**, *111*, 6452–6454.
- [62] M. M. J. Smulders, A. P. H. J. Schenning, E. W. Meijer, *J. Am. Chem. Soc.* **2008**, *130*, 606–611.
- [63] A. Abrishamkar, D. Rodríguez-San-Miguel, J. A. Rodríguez Navarro, R. Rodríguez-Trujillo, D. B. Amabilino, R. Mas-Ballesté, F. Zamora, A. J. deMello, J. Puigmarti-Luis, *J. Vis. Exp.* **2017**, *2017*, DOI 10.3791/56020.
- [64] C. D. Gutsche, *Calixarenes Revisited*, The Royal Society Of Chemistry, **1998**.
- [65] D. W. Dixon, *Q. Rev. Biol.* **2004**, *75*, 45–46.
- [66] A. Goldoni, *At. Mol. Supramol. Stud.* **2002**, *2002*, 64–65.
- [67] M. Biesaga, K. Pyrzyńska, M. Trojanowicz, *Talanta* **2000**, *51*, 209–224.
- [68] S. Hiroto, Y. Miyake, H. Shinokubo, *Chem. Rev.* **2017**, *117*, 2910–3043.
- [69] V. I. Minkin, M. N. Glukhovtsev, B. Y. Simkin, *Aromaticity and Antiaromaticity*, J. Wiley & Sons, **1994**.
- [70] K. M. Smith, *Porphyrins and Metalloporphyrins: A New Edition Based upon the Original Volume by J.E. Falk*, Elsevier Science & Technology, **1975**.
- [71] A. Harriman, J.-P. Sauvage, *Chem. Soc. Rev.* **1996**, *25*, 41–48.
- [72] G. Bottari, O. Trukhina, M. Ince, T. Torres, *Coord. Chem. Rev.* **2012**, *256*, 2453–2477.
- [73] M. G. Walter, A. B. Rudine, C. C. Wamser, *J. Porphyr. Phthalocyanines* **2010**, *14*, 759–792.
- [74] M. V. Martinez-Diaz, G. de la Torre, T. Torres, *Chem. Commun.* **2010**, *46*,

- 7090–7108.
- [75] H. Imahori, S. Fukuzumi, *Adv. Funct. Mater.* **2004**, *14*, 525–536.
- [76] R. Bonnett, *Chem. Soc. Rev.* **1995**, *24*, 19–33.
- [77] E. D. Sternberg, D. Dolphin, C. Brückner, *Tetrahedron* **1998**, *54*, 4151–4202.
- [78] D. E. Dolmans, D. Fukumura, R. K. Jain, *Nat. Rev. cancer* **2003**, *3*, 380.
- [79] C. Di Natale, D. Salimbeni, R. Paolesse, A. Macagnano, A. D’Amico, *Sensors Actuators B Chem.* **2000**, *65*, 220–226.
- [80] D. J. Dobson, S. Saini, *Anal. Chem.* **1997**, *69*, 3532–3538.
- [81] J. M. M. Rodrigues, A. S. F. Farinha, P. V. Muteto, S. M. Woranovicz-Barreira, F. A. A. Paz, M. G. Neves, J. A. S. Cavaleiro, A. C. Tomé, M. T. S. R. Gomes, J. L. Sessler, *Chem. Commun.* **2014**, *50*, 1359–1361.
- [82] R. Purrello, S. Gurrieri, R. Lauceri, *Coord. Chem. Rev.* **1999**, *190*, 683–706.
- [83] H. Eichhorn, *J. Porphyr. Phthalocyanines* **2000**, *4*, 88–102.
- [84] K. S. Suslick, N. A. Rakow, M. E. Kosal, J. Chou, *J. Porphyr. Phthalocyanines* **2000**, *4*, 407–413.
- [85] D. T. Gryko, C. Clausen, K. M. Roth, N. Dontha, D. F. Bocian, W. G. Kuhr, J. S. Lindsey, *J. Org. Chem.* **2000**, *65*, 7345–7355.
- [86] C. M. Carcel, J. K. Laha, R. S. Loewe, P. Thamyongkit, K.-H. Schweikart, V. Misra, D. F. Bocian, J. S. Lindsey, *J. Org. Chem.* **2004**, *69*, 6739–6750.
- [87] M. O. Senge, M. Fazekas, E. G. A. Notaras, W. J. Blau, M. Zawadzka, O. B. Locos, E. M. Ni Mhuircheartaigh, *Adv. Mater.* **2007**, *19*, 2737–2774.
- [88] L. Wang, Y. Chen, J. Jiang, *Nanoscale* **2014**, *6*, 1871–1878.
- [89] M. Calvete, G. Y. Yang, M. Hanack, *Synth. Met.* **2004**, *141*, 231–243.
- [90] A. Cnossen, C. Roche, H. L. Anderson, *Chem. Commun.* **2017**, *53*, 10410–10413.
- [91] H. L. Anderson, *Chem. Commun.* **1999**, 2323–2330.

-
- [92] C. M. Drain, J. D. Batteas, G. W. Flynn, T. Milic, N. Chi, D. G. Yablon, H. Sommers, *Proc. Natl. Acad. Sci.* **2002**, *99*, 6498–6502.
- [93] E. B. Fleischer, A. M. Shachter, *Inorg. Chem.* **1991**, *30*, 3763–3769.
- [94] K. Kinjo, T. Hirao, S. Kihara, Y. Katsumoto, T. Haino, *Angew. Chemie* **2015**, *127*, 15043–15047.
- [95] A. S. R. Koti, N. Periasamy, *Chem. Mater.* **2003**, *15*, 369–371.
- [96] G. De Luca, A. Romeo, V. Villari, N. Micali, I. Foltran, E. Foresti, I. G. Lesci, N. Roveri, T. Zuccheri, L. M. Scolaro, *J. Am. Chem. Soc.* **2009**, *131*, 6920–6921.
- [97] J. A. Wytko, R. Ruppert, C. Jeandon, J. Weiss, *Chem. Commun.* **2018**, *54*, 1550–1558.
- [98] M. da GH Vicente, K. M Smith, *Curr. Org. Synth.* **2014**, *11*, 3–28.
- [99] J. Karolczak, D. Kowalska, A. Lukaszewicz, A. Maciejewski, *J. Phys. Chem. A* **2004**, *108*, 4570–4575.
- [100] M. Senge, A. Ryan, K. Letchford, S. MacGowan, T. Mielke, *Symmetry (Basel)*. **2014**, *6*, 781–843.
- [101] J.-L. Soret, *Comptes rendus l'Académie des Sci.* **1883**, *97*, 1269–1270.
- [102] M. Gouterman, *J. Mol. Spectrosc.* **1961**, *6*, 138–163.
- [103] M. Gouterman, G. H. Wagnière, L. C. Snyder, *J. Mol. Spectrosc.* **1963**, *11*, 108–127.
- [104] C. Lecomte, M.-M. Rohmer, M. Benard, *Porphyr. Handb.* **2000**, *7*, 39–78.
- [105] D. Marsh, L. Mink, *J. Chem. Educ.* **1996**, *73*, 1188.
- [106] M. Prushan, *Synthesis (Stuttg)*. **2005**.
- [107] J.-L. Chambron, V. Heitz, J.-P. Sauvage, in *Porphyr. Handb.* (Eds.: K.M. Kadish, K.M. Smith, R. Guilard), Academic Press, **2000**, pp. 1–42.
- [108] P. Jordan, P. Fromme, H. T. Witt, O. Klukas, W. Saenger, N. Krauß, *Nature* **2001**, *411*, 909.
- [109] S. Bahatyrova, R. N. Frese, C. A. Siebert, J. D. Olsen, K. O. van der Werf,

-
- R. van Grondelle, R. A. Niederman, P. A. Bullough, C. Otto, C. N. Hunter, *Nature* **2004**, *430*, 1058.
- [110] G. M. McDermott, S. M. Prince, A. A. Freer, A. M. Hawthornthwaite-Lawless, M. Z. Papiz, R. J. Cogdell, N. W. Isaacs, *Nature* **1995**, *374*, 517.
- [111] A. Zouni, H.-T. Witt, J. Kern, P. Fromme, N. Krauss, W. Saenger, P. Orth, *Nature* **2001**, *409*, 739.
- [112] J. R. Postgate, *Biochem. J.* **1954**, *58*, ix–ix.
- [113] R. Haser, M. Pierrot, M. Frey, F. Payan, J. P. Astier, M. Bruschi, J. Le Gall, *Nature* **1979**, *282*, 806.
- [114] E. Iengo, E. Zangrando, E. Alessio, *Eur. J. Inorg. Chem.* **2003**, *2003*, 2371–2384.
- [115] A. K. Burrell, D. L. Officer, P. G. Plieger, D. C. W. Reid, *Chem. Rev.* **2001**, *101*, 2751–2796.
- [116] J. A. A. W. Elemans, R. Van Hameren, R. J. M. Nolte, A. E. Rowan, *Adv. Mater.* **2006**, *18*, 1251–1266.
- [117] D. Philp, J. F. Stoddart, *Angew. Chemie Int. Ed. English* **1996**, *35*, 1154–1196.
- [118] N. C. Maiti, S. Mazumdar, N. Periasamy, *J. Phys. Chem. B* **1998**, *102*, 1528–1538.
- [119] R. Purrello, L. Monsu' Scolaro, E. Bellacchio, S. Gurrieri, A. Romeo, *Inorg. Chem.* **1998**, *37*, 3647–3648.
- [120] O. Ohno, Y. Kaizu, H. Kobayashi, *J. Chem. Phys.* **1993**, *99*, 4128–4139.
- [121] E. E. Jelley, *Nature* **1936**, *138*, 1009–1010.
- [122] N. J. Hestand, F. C. Spano, *Acc. Chem. Res.* **2017**, *50*, 341–350.
- [123] A. S. Davydov, *Sov. Phys. Uspekhi* **1964**, *7*, 145.
- [124] M. Kasha, H. R. Rawls, M. A. El-Bayoumi, *Pure Appl. Chem.* **1965**, *11*, 371–392.
- [125] D. L. Dexter, *J. Chem. Phys.* **1953**, *21*, 836–850.

-
- [126] B. Ranjbar, P. Gill, *Chem. Biol. Drug Des.* **2009**, *74*, 101–120.
- [127] N. Berova, L. Di Bari, G. Pescitelli, *Chem. Soc. Rev.* **2007**, *36*, 914–931.
- [128] D. Akins, H. Zhu, C. Guo, *J. Phys. Chem.* **1994**, *98*, 3612–3618.
- [129] J. Taneja, N. Periasamy, *Chem. Phys. Lett.* **2003**, *375*, 171–176.
- [130] N. Micali, V. Villari, M. A. Castriciano, A. Romeo, L. M. Scolaro, *J. Phys. Chem. B* **2006**, *110*, 8289–8295.
- [131] A. Romeo, M. A. Castriciano, R. Zagami, G. Pollicino, L. Monsù Scolaro, R. F. Pasternack, *Chem. Sci.* **2017**, *8*, 961–967.
- [132] S. Allenmark, *Chirality* **2003**, *15*, 409–422.
- [133] G. A. Ascoli, E. Domenici, C. Bertucci, *Chirality* **2006**, *18*, 667–679.
- [134] B. Nordén, T. Kurucsev, *J. Mol. Recognit.* **1994**, *7*, 141–155.
- [135] M. Simonyi, Z. Bikádi, F. Zsila, J. Deli, *Chirality* **2003**, *15*, 680–698.
- [136] J. M. Ribó, J. Crusats, F. Sagués, J. Claret, R. Rubires, *Science (80-.)*. **2001**, *292*, 2063–2066.
- [137] H. Lambers, F. S. Chapin, T. L. Pons, in *Plant Physiol. Ecol.* (Eds.: H. Lambers, F.S. Chapin, T.L. Pons), Springer New York, New York, NY, **2008**, pp. 11–99.
- [138] R. F. Pasternack, P. R. Huber, P. Boyd, G. Engasser, L. Francesconi, E. Gibbs, P. Fasella, G. C. Venturo, L. D. Hinds, *J. Am. Chem. Soc.* **1972**, *94*, 4511–4517.
- [139] P. Pančoška, M. Urbanova, B. N. Korvatovsky, V. Z. Paschenko, K. Vacek, *Chem. Phys. Lett.* **1987**, *139*, 49–54.
- [140] P. Pančoška, M. Urbanová, L. Bednárová, K. Vacek, V. Z. Paschenko, S. Vasiliev, P. Maloň, M. Král, *Chem. Phys.* **1990**, *147*, 401–413.
- [141] R. F. Pasternack, A. Giannetto, P. Pagano, E. J. Gibbs, *J. Am. Chem. Soc.* **1991**, *113*, 7799–7800.
- [142] R. F. Pasternack, E. J. Gibbs, *J. Inorg. Organomet. Polym.* **1993**, *3*, 77–88.

-
- [143] E. Bellacchio, R. Lauceri, S. Gurrieri, L. M. Scolaro, A. Romeo, R. Purrello, *J. Am. Chem. Soc.* **1998**, *120*, 12353–12354.
- [144] H. Onouchi, T. Miyagawa, K. Morino, E. Yashima, *Angew. Chemie Int. Ed.* **2006**, *45*, 2381–2384.
- [145] D. Schlettwein, N. I. Jaeger, T. Oekermann, *Porphyr. Handb.* **2003**, 247–283.
- [146] R. Wang, R. Qu, C. Jing, Y. Zhai, Y. An, L. Shi, *RSC Adv.* **2017**, *7*, 10100–10107.
- [147] Z. Chai, L. Ma, Y. Wang, X. Ren, M. Gao, *J. Macromol. Sci. Part A Pure Appl. Chem.* **2016**, *53*, 270–275.
- [148] O. Kokhan, N. Ponomarenko, P. R. Pokkuluri, M. Schiffer, D. M. Tiede, *Biochemistry* **2014**, *53*, 5070–5079.
- [149] J. K. Choi, A. D’Urso, M. Balaz, *J. Inorg. Biochem.* **2013**, *127*, 1–6.
- [150] R. Lauceri, T. Campagna, A. Raudino, R. Purrello, *Inorganica Chim. Acta* **2001**, *317*, 282–289.
- [151] X. Wang, L. Zhao, R. Ma, Y. An, L. Shi, *Chem. Commun.* **2010**, *46*, 6560–6562.
- [152] J. G. Nørby, P. Ottolenghi, J. Jensen, *Anal. Biochem.* **1980**, *102*, 318–320.
- [153] R. F. Pasternack, E. J. Gibbs, J. J. Villafranca, *Biochemistry* **1983**, *22*, 2406–2414.
- [154] C. M. Drain, J.-M. Lehn, *J. Chem. Soc. Chem. Commun.* **1994**, 2313–2315.
- [155] K. Kano, *Colloid Polym. Sci.* **2008**, *286*, 79–84.
- [156] D. J. Cram, H. Steinberg, *J. Am. Chem. Soc.* **1951**, *73*, 5691–5704.
- [157] IUPAC-IUB Comm. on Biochem. Nomencl, *J. Org. Chem.* **2007**, *35*, 2849–2867.
- [158] A. Zinke, E. Ziegler, *Berichte der Dtsch. Chem. Gesellschaft (A B Ser.)* **1944**, *77*, 264–272.

-
- [159] J. W. Cornforth, P. D. Hart, G. A. Nicholls, R. J. W. Rees, J. A. Stock, *Br. J. Pharmacol. Chemother.* **1955**, *10*, 73–86.
- [160] L. C. Groenen, J. D. van Loon, W. Verboom, D. N. Reinhoudt, S. Harkema, A. Casnati, R. Ungaro, A. Pochini, F. Ugozzoll, *J. Am. Chem. Soc.* **1991**, *113*, 2385–2392.
- [161] D.-S. Guo, Y. Liu, *Acc. Chem. Res.* **2014**, *47*, 1925–1934.
- [162] D. S. Guo, K. Chen, H. Q. Zhang, Y. Liu, *Chem. - An Asian J.* **2009**, *4*, 436–445.
- [163] R. De Zorzi, N. Guidolin, L. Randaccio, R. Purrello, S. Geremia, *J. Am. Chem. Soc.* **2009**, *131*, 2487–2489.
- [164] D. S. Guo, K. Wang, Y. Liu, *J. Incl. Phenom. Macrocycl. Chem.* **2008**, *62*, 1–21.
- [165] F. Perret, A. N. Lazar, A. W. Coleman, *Chem. Commun.* **2006**, 2425–2438.
- [166] S. J. Dalgarno, J. L. Atwood, C. L. Raston, *Chem. Commun.* **2006**, 4567–4574.
- [167] J. L. Atwood, L. J. Barbour, M. J. Hardie, C. L. Raston, *Coord. Chem. Rev.* **2001**, *222*, 3–32.
- [168] L. Di Costanzo, R. Purrello, R. Lauceri, F. G. Gulino, V. Pavone, S. Geremia, D. Sciotto, L. Randaccio, *Angew. Chemie - Int. Ed.* **2001**, *40*, 4245–4247.
- [169] G. Moschetto, R. Lauceri, F. G. Gulino, D. Sciotto, R. Purrello, *J. Am. Chem. Soc.* **2002**, *124*, 14536–14537.
- [170] A. D’Urso, D. A. Cristaldi, M. E. Fragalà, G. Gattuso, A. Pappalardo, V. Villari, N. Micali, S. Pappalardo, M. F. Parisi, R. Purrello, *Chem. Eur. J.* **2010**, *16*, 10439–10446.
- [171] A. D’Urso, P. F. Nicotra, G. Centonze, M. E. Fragalà, G. Gattuso, A. Notti, A. Pappalardo, S. Pappalardo, M. F. Parisi, R. Purrello, *Chem. Commun.* **2012**, *48*, 4046–4048.

-
- [172] O. Herrmann, S. H. Mehdi, A. Corsini, *Can. J. Chem.* **1978**, *56*, 1084–1087.
- [173] K. Puchnin, D. Cheshkov, P. Zaikin, I. Vatsouro, V. Kovalev, *New J. Chem.* **2013**, *37*, 416–424.
- [174] V. Böhmer, C. Musigmann, A. Shivanyuk, J.-F. Desreux, B. Lambert, L. Delmau, J.-F. Dozol, M. A. Garcia Carrera, A. Arduini, A. Pochini, et al., *Chem. - A Eur. J.* **2000**, *6*, 2135–2144.
- [175] G. Arena, A. Contino, E. Longo, G. Spoto, A. Arduini, A. Pochini, A. Secchi, C. Massera, F. Ugozzoli, *New J. Chem.* **2004**, *28*, 56.
- [176] P. Schmitt, P. D. Beer, M. G. B. Drew, P. D. Sheen, *Angew. Chemie (International Ed. English)* **1997**, *36*, 1840–1842.
- [177] G. Horvat, V. Stilinović, T. Hrenar, B. Kaitner, L. Frkanec, V. Tomišić, *Inorg. Chem.* **2012**, *51*, 6264–6278.
- [178] S. E. Matthews, P. Schmitt, V. Felix, M. G. B. Drew, P. D. Beer, *J. Am. Chem. Soc.* **2002**, *124*, 1341–1353.
- [179] R. Randazzo, A. Mammana, A. D’Urso, R. Lauceri, R. Purrello, *Angew. Chemie - Int. Ed.* **2008**, *47*, 9879–9882.
- [180] D. Seebach, *Angew. Chemie Int. Ed. English* **1990**, *29*, 1320–1367.
- [181] M. Li, Y. Li, H. Zhang, S. Wang, Y. Ao, Z. Cui, *J. Mater. Chem. C* **2017**, *5*, 4111–4122.
- [182] K. Wang, H. Wu, Y. Meng, Z. Wei, *Small* **2013**, *10*, 14–31.
- [183] Y. Zhu, Y. Zhang, B. Yao, Y. Wang, Z. Zhang, H. Zhan, B. Zhang, Z. Xie, Y. Wang, Y. Cheng, *Macromolecules* **2016**, *49*, 4373–4377.
- [184] P. J. Waller, F. Gándara, O. M. Yaghi, *Acc. Chem. Res.* **2015**, *48*, 3053–3063.
- [185] R. Dawson, A. I. Cooper, D. J. Adams, *Prog. Polym. Sci.* **2012**, *37*, 530–563.
- [186] M. Design, D. Group, A. Arbor, O. M. Yaghi, M. O’keeffe, N. W. Ockwig,

-
- H. K. Chae, M. Eddaoudi, J. Kim, *Nature* **2003**, *423*, 705.
- [187] H. C. Zhou, J. R. Long, O. M. Yaghi, *Chem. Rev.* **2012**, *112*, 673–674.
- [188] H. Furukawa, K. E. Cordova, M. O’Keeffe, O. M. Yaghi, *Science (80-.)*. **2013**, *341*, 1230444–1230444.
- [189] V. Bon, I. Senkovska, S. Kaskel, in *Nanoporous Mater. Gas Storage. Green Energy Technol.* (Ed.: R.-R.F. Kaneko K.), Springer, Singapore, **2019**, pp. 137–172.
- [190] R. S. Patil, A. M. Drachnik, H. Kumari, C. L. Barnes, C. A. Deakynne, J. L. Atwood, *Cryst. Growth Des.* **2015**, *15*, 2781–2786.
- [191] R. S. Patil, D. Banerjee, C. Zhang, P. K. Thallapally, J. L. Atwood, *Angew. Chemie - Int. Ed.* **2016**, *55*, 4523–4526.
- [192] J. Tian, L. Chen, D.-W. Zhang, Y. Liu, Z.-T. Li, *Chem. Commun.* **2016**, *52*, 6351–6362.
- [193] S.-Y. Ding, W. Wang, *Chem. Soc. Rev.* **2013**, *42*, 548–568.
- [194] M. S. Lohse, T. Bein, *Adv. Funct. Mater.* **2018**, *28*, 1705553.
- [195] A. P. Cote, A. I. Benin, N. W. Ockwig, M. O’keeffe, A. J. Matzger, O. M. Yaghi, *Science (80-.)*. **2005**, *310*, 1166–1170.
- [196] D. Rodríguez-San-Miguel, A. Yazdi, V. Guillerm, J. Pérez-Carvajal, V. Puentes, D. Maspoch, F. Zamora, *Chem. - A Eur. J.* **2017**, *23*, 8623–8627.
- [197] D. Rodríguez-San-Miguel, A. Abrishamkar, J. A. R. Navarro, R. Rodríguez-Trujillo, D. B. Amabilino, R. Mas-Ballesté, F. Zamora, J. Puigmartí-Luis, *Chem. Commun.* **2016**, *52*, 9212–9215.
- [198] T. Ma, E. A. Kapustin, S. X. Yin, L. Liang, Z. Zhou, J. Niu, L.-H. Li, Y. Wang, J. Su, J. Li, *Science (80-.)*. **2018**, *361*, 48–52.
- [199] J. Lee, O. K. Farha, J. Roberts, K. A. Scheidt, S. T. Nguyen, J. T. Hupp, *Chem. Soc. Rev.* **2009**, *38*, 1450–1459.
- [200] L. E. Kreno, K. Leong, O. K. Farha, M. Allendorf, R. P. Van Duyne, J. T. Hupp, *Chem. Rev.* **2011**, *112*, 1105–1125.

-
- [201] J.-R. Li, J. Sculley, H.-C. Zhou, *Chem. Rev.* **2011**, *112*, 869–932.
- [202] B. F. Hoskins, R. Robson, *J. Am. Chem. Soc.* **1990**, *112*, 1546–1554.
- [203] S. Kitagawa, M. Munakata, T. Tanimura, *Chem. Lett.* **1991**, *20*, 623–626.
- [204] O. M. Yaghi, G. Li, T. L. Groy, *J. Chem. Soc. Dalton Trans.* **1995**, 727–732.
- [205] O. M. Yaghi, H. Li, C. Davis, D. Richardson, T. L. Groy, *Acc. Chem. Res.* **1998**, *31*, 474–484.
- [206] Nathaniel L. Rosi, Juergen Eckert, Mohamed Eddaoudi, David T. Vodak, M. O’Keeffe, J. Kim, O. M. Yaghi, *Science (80-.)*. **2003**, *300*, 1127–1129.
- [207] S. S. Kaye, A. Dailly, O. M. Yaghi, J. R. Long, *J. Am. Chem. Soc.* **2007**, *129*, 14176–14177.
- [208] D. J. Collins, H.-C. Zhou, *J. Mater. Chem.* **2007**, *17*, 3154–3160.
- [209] J.-R. Li, Y. Ma, M. C. McCarthy, J. Sculley, J. Yu, H.-K. Jeong, P. B. Balbuena, H.-C. Zhou, *Coord. Chem. Rev.* **2011**, *255*, 1791–1823.
- [210] J.-R. Li, R. J. Kuppler, H.-C. Zhou, *Chem. Soc. Rev.* **2009**, *38*, 1477–1504.
- [211] W. Yang, A. Greenaway, X. Lin, R. Matsuda, A. J. Blake, C. Wilson, W. Lewis, P. Hubberstey, S. Kitagawa, N. R. Champness, et al., *J. Am. Chem. Soc.* **2010**, *132*, 14457–14469.
- [212] J. Lü, C. Perez-Krap, M. Suyetin, N. H. Alsmail, Y. Yan, S. Yang, W. Lewis, E. Bichoutskaia, C. C. Tang, A. J. Blake, et al., *J. Am. Chem. Soc.* **2014**, *136*, 12828–12831.
- [213] J. Tian, H. Wang, D. W. Zhang, Y. Liu, Z. T. Li, *Natl. Sci. Rev.* **2017**, *4*, 426–436.
- [214] K.-D. Zhang, K.-D. Zhang, J. Tian, J. Tian, D. Hanifi, D. Hanifi, Y. Zhang, Y. Zhang, A. C.-H. Sue, A. C.-H. Sue, et al., *J. Am. Chem. Soc.* **2013**, *135*, 17913–17918.
- [215] J. Tian, T.-Y. Zhou, S.-C. Zhang, S. Aloni, M. V. Altoe, S.-H. Xie, H. Wang, D.-W. Zhang, X. Zhao, Y. Liu, *Nat. Commun.* **2014**, *5*, 5574.
- [216] T. Y. Zhou, Q. Y. Qi, Q. L. Zhao, J. Fu, Y. Liu, Z. Ma, X. Zhao, *Polym.*

- Chem.* **2015**, *6*, 3018–3023.
- [217] L. Zhang, Y. Jia, H. Wang, D. W. Zhang, Q. Zhang, Y. Liu, Z. T. Li, *Polym. Chem.* **2016**, *7*, 1861–1865.
- [218] H. Tang, W. Zhou, L. Zhang, *J. Hazard. Mater.* **2012**, *209–210*, 218–225.
- [219] A. Mellah, S. P. S. Fernandes, R. Rodríguez, J. Otero, J. Paz, J. Cruces, D. D. Medina, H. Djamila, B. Espiña, L. M. Salonen, *Chem. - A Eur. J.* **2018**, DOI 10.1002/chem.201801649.
- [220] S. Y. Ding, J. Gao, Q. Wang, Y. Zhang, W. G. Song, C. Y. Su, W. Wang, *J. Am. Chem. Soc.* **2011**, *133*, 19816–19822.

Appendix

Instrumental techniques' overview

UV-Vis Spectroscopy

UV-vis spectrophotometry is primarily a quantitative analytical technique concerned with the absorption of near-ultraviolet (180–390 nm) or visible (390–780 nm) radiation by chemical species in solution or in the gas phase. The near-ultraviolet and the visible regions of the electromagnetic spectrum provide energy that gives rise to electronic transitions. Because of the superimposition of vibrational and rotational transitions, the UV-vis spectra of analytes in solution show little fine structure.

In general, organic compounds absorb energy in the near-ultraviolet region due to $\sigma \rightarrow \sigma^*$, $n \rightarrow \sigma^*$, $n \rightarrow \pi^*$ and $\pi \rightarrow \pi^*$ transitions. Most transitions of interest involve the promotion of n or π electrons to the π^* excited state and therefore favors molecules with delocalized π electrons (i.e. aromatic and conjugated species). The part of the molecule that absorbs energy is known as a chromophore. The wavelength of maximum absorption of a chemical species can be altered by the nature of the substituent(s) on the aromatic ring or the conjugated system. Substituents containing lone pairs of electrons, e.g. $-\text{OH}$, $-\text{NH}_2$, generally result in a longer wavelength of maximum absorption and a higher molar absorptivity. Such groups are also known as *auxochromes*. Moreover, some inorganic compounds can be detected in the visible region by their inherent absorption of radiation. For example, the transition metal ions and their aquo-complexes are often colored and present a reasonable molar absorptivity due to the electronic transitions involving the 3d and 4d orbitals.

Under controlled experimental conditions, the amount of radiation absorbed is directly related to the concentration of the analyte in solution, and

this relationship is known as Beer-Lambert's law. This latter relationship is described by the equation:

$$A = \epsilon b c$$

where A is the absorbance of the solution (no units), ϵ is the molar absorptivity ($\text{L mol}^{-1}\text{cm}^{-1}$), b is the path length of radiation through the absorbing medium (cm); and c is the concentration (mol L^{-1}).

However, the Beer-Lambert's law shows some limitations, known as *deviations*. Among them, the law is not applicable at high analyte concentrations ($> 0.01 \text{ mol L}^{-1}$) due to interactions between analyte molecules. There are also limitations to its applicability due to instrumental and chemical deviations:

Instrumental deviations- The electromagnetic radiation impinging on the sample is polychromatic rather than monochromatic (unless a laser light source is used) and this can lead to negative deviations from Beer-Lambert's law at higher analyte concentrations and to a loss of sensitivity because the averaged ϵ value is lower than the theoretical one. Stray radiation is another source of deviation and this extraneous external radiation results from scattering, reflection and refraction effects from mirrors, lenses, filters and other optical components. In addition, radiation losses can occur due to reflection or refraction at the environment/cuvette/sample interfaces and concentration gradients inside the sample solution which establish transient mirrors and lenses.

Chemical deviations- Changes in absorbance due to changes in the chemical environment of the sample, e.g. pH. Absorbance of a solution can also be influenced by acid-base equilibria, redox reactions and complexation reactions. With all equilibria, there is one wavelength, known as the *isosbestic point*, where the absorbances of both species are equal because they have the same ϵ value. The isosbestic point can be used as a reference wavelength for kinetic studies and to verify the wavelength accuracy of a spectrophotometer. It can also be used as the reference wavelength in dual wavelength

spectrophotometry because the transmittance at this wavelength is not affected by the development of any chemical reaction.

The nature of the solvent and refractive index changes can also cause positive deviations, and this should be checked as part of the measurement protocol for the blank. There may also be positive interferences due to absorption by other components of the sample matrix and/or excess reagents, which would require separation prior to detection, masking by the addition of an appropriate reagent, minimizing by sample dilution and/or lowering the reagent concentration.

Last, but not least, the presence of potential interfering species which react with the main reagent to yield similar colored species or cause a lowering of the effective reagent concentration should always be taken into account. Analytical selectivity is a primary consideration for every application.

Moreover, *derivative spectrophotometry* can also be exploited to mathematically process the data after acquisition, thus improving spectral resolution in multi-component systems. In this approach the zero-order absorbance spectrum is derivatised with respect to wavelength to give first order ($dA/d\lambda$) or higher order plots of the rate of change of absorbance against absorbance. The main attractions of this approach are the enhancement of any differences between (similar) spectra and the reduction of the effect of any broadband matrix interferences.

The basic instrumentation consists of a radiation source, a wavelength-selection device, a sample compartment, a detector and an output device . For visible radiation, a tungsten filament is the most common source and for near-ultraviolet radiation a deuterium lamp is usually used. For better resolution, a grating monochromator is used as the wavelength-selection device, which can also be

used for scanning the wavelength range of interest. The sample compartment is usually a cuvette with a 1.0 cm square cross-section made of quartz (for the near-ultraviolet region), glass or plastic (for the visible region). For detection, a photomultiplier tube is the most common device; phototubes and, increasingly, photodiodes and diode arrays, are also used.

The two most common optical configurations for UV-vis spectrophotometers are single-beam and double-beam. Single beam instruments are usually cheaper and involve simple optics whereas double beam instruments are more convenient for spectral scanning. Other advantages of the double beam configuration include the ability to compensate for *i)* stray light, *ii)* fluctuations in the intensity of the source radiation and detector response and *iii)* the presence of solid particles in the sample solution.

An alternative optical configuration is used in diode array spectrophotometry, wherein polychromatic light from the source passes through the sample cuvette and is then dispersed by a grating onto a linear diode array detector. The advantages are speed, negligible stray light effects due to the *reverse* optical configuration, wavelength setting reproducibility due to the absence of moving optical components and simultaneous multi-wavelength data acquisition. This feature lends itself to post-acquisition digital data processing techniques such as dual wavelength spectrophotometry, derivative spectrophotometry and multi-variate calibration.

Fluorescence Spectroscopy

Fluorescence spectroscopy is an emission phenomenon where an energy transition from a higher to a lower state is accompanied by radiation. Only molecules in their excited forms are able to emit fluorescence; thus, they have to be brought into a state of higher energy prior to the emission phenomenon.

For a better comprehension of the phenomenon, we need to observe the following diagram in **Fig.107** also called *Jablonski's diagram*.

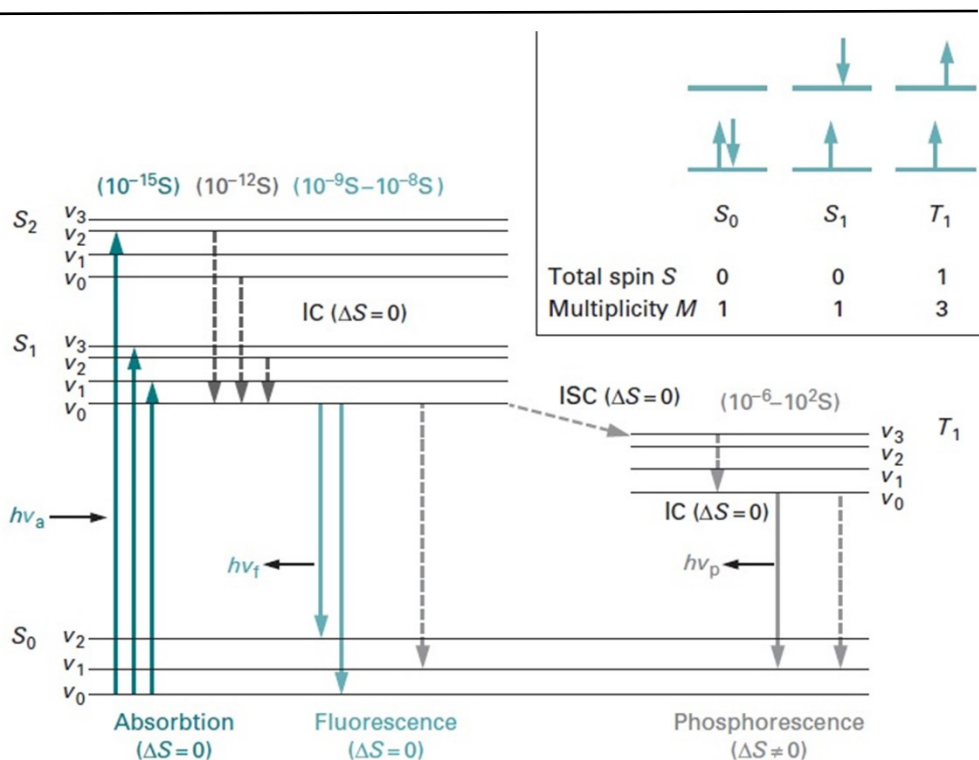


Fig 107 Jablonski's Diagram- In the diagram are shown: the electronic ground state (S_0), two excited singlet states (S_1 , S_2) and a triplet state (T_1). Vibrational level (V) are only illustrated exemplarily. Solid vertical lines indicate radiative transitions, dotted-lines show non-radiative transitions (i.e. Internal Conversion, IC). The inset shows the relationship between electron configurations, total spin number S and multiplicity M .

In these diagrams, energy transitions are indicated by vertical lines. Not all transitions are possible: allowed transitions are defined by the selection rules of quantum mechanics.

A molecule in its electronic and vibrational ground state (S_1V_0) can absorb photons matching the energy difference of its various discrete states. The required photon energy has to be higher than that required to reach the vibrational ground state of the first electronic excited state (S_1V_0). The excess energy is absorbed as vibrational energy ($V > 0$), and quickly dissipated as heat by collision with solvent molecules. The molecule, thus, returns to the vibrational ground state of the first electronic excited state (S_1V_0). These relaxation processes are non-radiating transitions from one energetic state to another with lower energy and are called internal conversion (IC). From the lowest level of the first electronic excited state, the molecule returns to the ground state (S_0) either by emitting light (*fluorescence*) or by a non-radiative transition.

Upon radiative transition, the molecule can end up in any of the vibrational states of the electronic ground state (as per quantum mechanical rules). If the vibrational levels of the ground state overlap with those of the electronic excited state, the molecule will not emit fluorescence, but rather revert to the ground state by non-radiative internal conversion. This is the most common way for excitation energy to be dissipated and is why fluorescent molecules are rather rare. Most molecules are flexible and thus have very high vibrational levels in the ground state. Indeed, most fluorescent molecules possess fairly rigid aromatic rings or ring systems. The fluorescent group in a molecule is called a *fluorophore*.

Since radiative energy is lost in fluorescence as compared to the absorption, the fluorescent light is always at a longer wavelength than the exciting light (namely, *Stokes shift*). The emitted radiation appears as band spectrum, because there are many closely related wavelength values dependent on the vibrational and rotational energy levels attained. However, the fluorescence spectrum of a

molecule is independent of the wavelength of the exciting radiation and has a mirror image relationship with the absorption spectrum. In addition, the probability of the transition from the electronic excited to the ground state is proportional to the intensity of the emitted light.

In this context, an associated phenomenon is the *phosphorescence* due to the transition from a triplet state (T_1) to the electronic singlet ground state (S_0). The molecule gets into the triplet state from an electronic excited singlet state (S_1) by a process called intersystem crossing (ISC). Noteworthy, the transition from singlet state to triplet state is quantum-mechanically not allowed (i.e. happens with very low probability) and thus only in certain molecules where the electronic structure is favorable, such as heavy atoms. The rate constants for phosphorescence are much longer, as a consequence, phosphorescence occurs with a long delay and persists even when the exciting energy is no longer applied.

The fluorescence properties of a molecule are determined by properties of the molecule itself (internal factors), as well as the environment (external factors). The fluorescence intensity emitted by a molecule is dependent on the lifetime of the excited state. The transition from the excited to the ground state can be treated like a decay process of first order, i.e. the number of molecules in the excited state decreases exponentially with time.

In analogy to kinetics, the exponential coefficient K_r is called rate constant and is the reciprocal of the lifetime: $\tau = K_r^{-1}$. If a population of fluorophores is excited, the lifetime is the time it takes to reduce the number of fluorescence emitting molecules to $1/e$ or 36.8% of the original population N_0 (i.e. N_0/e).

However, the effective lifetime τ of excited molecules differs from the fluorescence lifetime τ_r as other processes (e.g. internal conversion, quenching, fluorescence resonance energy transfer, reactions of the excited state, intersystem crossing etc.) can affect the number of molecules in the excited state.

The ratio between photons emitted and photons absorbed by a fluorophore is called *quantum yield* Φ . The quantum yield is a dimensionless quantity, and most importantly, the only absolute measure of fluorescence for a molecule. Measuring the quantum yield is a difficult process and requires comparison with a fluorophore of known quantum yield. Most commonly, the fluorescence emissions of two or more related samples are compared and their relative differences analyzed.

Fluorescence spectroscopy works most accurately at very low concentrations of emitting fluorophores. UV/Vis spectroscopy, in contrast, is less accurate at such low concentrations. One major factor adding to the high sensitivity of fluorescence applications is the spectral selectivity. Due to the Stokes shift, the wavelength of the emitted light is different from that of the exciting light. Another feature makes use of the fact that fluorescence is emitted in all directions. By placing the detector perpendicular to the excitation pathway, the background of the incident beam is reduced.

In a typical spectrofluorimeter two monochromators are used, one for tuning the wavelength of the exciting beam and a second one for analysis of the fluorescence emission. Due to the emitted light always having a lower energy than the exciting light, the wavelength of the excitation monochromator is set at a lower wavelength than the emission monochromator. The better fluorescence spectrometers in laboratories have a photon-counting detector yielding very high sensitivity. Temperature control is required for accurate work as the emission intensity of a fluorophore is dependent on the temperature of the solution. The optical geometries with 90° arrangement are commonly used. Pre- and post-filter effects can arise owing to absorption of light prior to reaching the fluorophore and the reduction of emitted radiation. These phenomena are also called inner filter effects and are more evident in solutions with high concentrations.

Resonance Light Scattering Spectroscopy

Resonance light scattering (RLS) spectroscopy on supramolecular assemblies of chromophores is a sensitive and selective method to extract size and shape information. Generally, light scattering experiments employ wavelengths away from absorption bands. On the contrary, wavelengths within the absorption band can be extremely informative if the absorption is not too great, and the aggregate is of sufficient size.

The RLS effect is observed as increased scattering intensity at wavelengths very near to the absorption of a molecular aggregated. The effect can be enhanced by several orders of magnitude when strong electronic coupling exists among the chromophores. In addition, the wavelength dependence of this technique allows for selective observation of aggregates, even in multicomponent systems that include a large fraction of monomers or other aggregates.

In general, two processes occur when light passes through a solution of aggregates. If the solvent itself is non-absorbing, thus energy is removed from the incident light through absorption and scattering by the aggregates.

The light scattering component is a consequence of differences in polarizability between the aggregates and the solvent. The incident electromagnetic wave induces an oscillating dipole in the assembly, which radiates light in all directions.

The ratio of the rate of energy absorption from the incident beam to the intensity of the incident beam is called the *absorption cross section*. Whereas, the ratio of the rate of energy scattering out of the incident beam (in all directions) to the intensity of the incident beam is called the *scattering cross section*. If the induced dipole can be considered ideal (usually a valid assumption if the size of the aggregate is small compared to the wavelength of the light in the solvent) both cross sections are related to the polarizability α of the aggregates. In

particular, the polarizability can be considered as the sum of its real part α_r (related to light-scattering phenomena) and of its imaginary part α_i (related to absorption processes).

Thus, the absorption at a certain wavelength band by a solution of aggregates leads to a maximum in the imaginary part of the polarizability α_i , so that α_r also behaves anomalously, resulting in an increased scattering.

Under normal conditions this increased scattering is difficult or impossible to detect because of the increased absorption and the weakness of the enhanced scattering effect. However, when this effect is investigated for aggregates of chromophores, the enhanced RLS scattering can be enormous.

The absorption depends on the first power of the polarizability, which in turn depends linearly on the volume of the aggregate. Although a solution with a fixed concentration of monomers will not exhibit changes in absorbance, the aggregation process could lead to larger volume triggering an enhanced scattering. of the assemblies the scattering. As a result, RLS is extremely sensitive to even low concentrations of extended aggregates.

Final, it is worth mentioning that in many cases RLS experiments can be conducted with conventional equipment, for instance by using an ordinary double-monochromator fluorimeter in synchronous scan.

Circular Dichroism Spectroscopy

Circular dichroism spectroscopy, or simply CD, is strictly allied to chirality, because it is a manifestation of diastereomer discrimination. CD may be regarded as one of the most powerful techniques for stereochemical analysis: it is sensitive to the absolute configuration as well as to conformational features, which are often completely obscured in the ordinary absorption spectrum.

The CD spectroscopy is based on the fact that the *plane-polarized light* wave can be obtained as a superposition of a *left circularly polarized light* and a *right circularly polarized light*, whose amplitude and wavelength are identical, see the schematic **Fig.108** below.

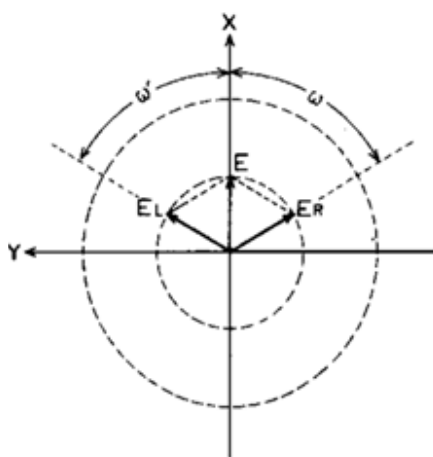


Fig 108 The superposition between the electric field vector's left circularly polarized light E_L , with the electric field vector's right circularly polarized light E_R results in a plane-polarized electric field E

Any chiral non-racemic sample adsorbs left circularly polarized light to a different extent than right circularly polarized light: this phenomenon is called Circular Dichroism. In other words, CD is the difference:

$$CD = A^l - A^r$$

where A^l and A^r are the absorptions of left and right circularly polarized light, respectively. The definition of the equation immediately tells us that CD can be measured only in correspondence to absorption bands; a dichroic peak is also called a Cotton effect, on account of the discoverer of the phenomenon. Moreover, it is easy to show that for each absorption band, the CD of two enantiomers are always exactly opposite.

As illustrated in **Fig.109**, the superposition of the two components is no longer a linearly polarized wave when CD occurs. The resulting electric field vector does not oscillate along a straight line, but it rotates along an ellipsoid path. In other terms, such light wave is called an *elliptically polarized light*.

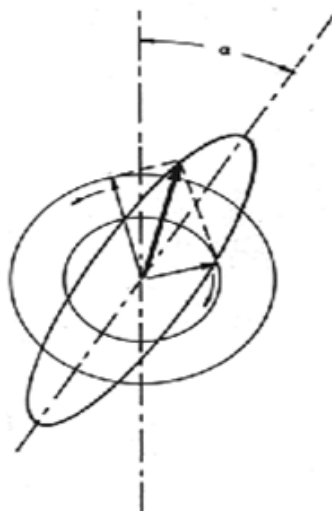


Fig 109 Illustration of the elliptically polarized light

For this reasons, the output of CD instruments is usually measured as ellipticity θ (in mdeg), related to CD through θ (mdeg) = 33000 CD.

The basic instrumentation for CD measurement is the conventional spectropolarimeter. In the most common setup, there is a device between the

monochromator and the sample compartment, called photoelastic modulator (PEM), which alternatively furnishes left and right circularly polarized light .

It is based on a piezoelectric quartz crystal typically oscillating with a frequency in the 50 kHz range: during each cycle the light polarization changes, while the intensity remains constant. After passing through a chiral non-racemic sample, because the two circularly polarized light components become absorbed to a different extent, the light reaching the detector is time-modulated with the same frequency as the PEM. Phase-locked amplification of this signal can provide simultaneously absorbance, and circular dichroism

Theoretically, a baseline correction should not be required for CD, since the baseline is expected to be 0. In real life, on the contrary, it is strongly recommended that any CD spectrum is corrected by baseline subtraction obtained from a measurement ideally of the racemic compound at the same concentration and in the same cell; as a common alternative, a blank of the same solvent provides acceptable results.

Infrared Spectroscopy

Infrared (IR) spectroscopy is an analytic method based on the absorption of IR radiation by vibrational excitation of lattices, surface groups, molecules, etc. in each physical condition. The absorptions are always associated with a change in the dipole moment of the molecule/material. Consequently, vibrational and/or rotational modes of molecules, lattices, surface groups, etc. not involving a change in the dipole moment do not absorb IR radiation and are not visible in the IR spectrum; they are IR inactive.

Except for some noble gases and homonuclear diatomic molecules like H₂, O₂, N₂, etc., IR spectroscopy enables the qualitative and quantitative analysis of most organic as well as many inorganic compounds.

Since the vibrational energy levels are unique to each molecule, the IR spectra provide a “fingerprint” of a particular molecule. The frequencies of these molecular vibrations depend on the masses of the atoms, their geometric arrangement, and the strength of their chemical bonds. The spectra provide, as well, information on molecular structure, dynamics, and environment.

Two different approaches are used for the interpretation of vibrational spectroscopy and elucidation of molecular structure:

- 1) use of group theory with mathematical calculations of the forms and frequencies of the molecular vibrations;
- 2) use of empirical characteristic frequencies for chemical functional groups.

Many empirical group frequencies have been explained and refined using the mathematical theoretical approach. In general, many identification problems are solved using the empirical approach. Certain functional groups show characteristic vibrations in which only the atoms in that particular group are displaced. Since these vibrations are mechanically independent from the rest of

the molecule, these group vibrations will have a characteristic frequency, which remains relatively unchanged regardless of what molecule the group is in. Typically, group frequency analysis is used to reveal the presence and absence of various functional groups in the molecule, thereby helping to elucidate the molecular structure.

IR spectrometers generally consist of four main functional elements:

- an IR radiation source like a traditional thermal emitter (Si carbide rod, Nernst-stick);
- a dispersion and/or modulation element such as a traditional prism or grating monochromator, and more recently an interferometer;
- a sample including its holder/sampling cell and supporting elements;
- an IR detector, e.g. a pyroelectric or semiconducting element or a differential gas-pressure sensor (i.e. bolometer).

In case of a traditional dispersive spectrometer, the four elements are arranged in the same sequence as listed above. A transmission spectrum, for example, is recorded by the registration of the detector signal during a sequential wavelength sweep by turning the dispersive element. The absorption is calculated by dividing the transmission signal with the sample by the signal of the empty arrangement as reference. As a result, the spectral instrument characteristic is automatically eliminated. In some cases, the incident signal is modulated in order to eliminate the influence of stray light and/or background.

Today, the traditional dispersive IR spectrometers have been almost entirely displaced by FTIR spectrometers. In this new generation of spectrometers, the incident IR beam is modulated by passing through an interferometer (e.g. a Michelson type) with an oscillating mirror and the IR detector registers it after passing through the sample. The conversion of this time-

dependent signal into a wavenumber-dependent IR spectrum is done by Fourier-transform (FT).

In contrast to the time-consuming sequential registration with dispersive systems, the FT principle provides the so-called multiplex advantage: each forward and/or backward scan of the moving interferometer mirror can be used to record a complete spectrum. The resolution depends on the travel length of the mirror while the Signal-Noise ratio depends on the square root of the number of scans as well as on the sensor characteristics.

Nevertheless, the spectral range is limited by the spectral characteristics of the IR source, the beam-splitter and the detector. Furthermore, the transparency and reflectivity of windows and mirrors as well as disturbing ubiquitous gases (mostly water vapour and carbon dioxide) in the light path have to be considered.

Nuclear Magnetic Resonance Spectroscopy

Nuclear Magnetic Resonance (NMR) spectroscopy is an analytical chemistry technique used in quality control and research for determining the content and purity of a sample as well as its molecular structure. For instance, NMR can quantitatively analyze mixtures containing known compounds. In the case of unknown compounds, NMR can either be used to match against spectral libraries or to deduce the basic structure directly.

Once the basic structure is known, NMR can be used to determine molecular conformation in solution as well as studying physical properties at the molecular level such as conformational exchange, phase changes, solubility, and diffusion. In order to achieve the desired results, a variety of NMR techniques are available.

The principle behind NMR is that many nuclei have spin and all nuclei are electrically charged. Nevertheless, in many atoms (such as ^{12}C) these spins are paired against each other, such that the nucleus of the atom has no overall spin. However, in some atoms (such as ^1H and ^{13}C) the nucleus does possess an overall spin. The rules for determining the net spin of a nucleus are as follows:

- 1) if the number of neutrons and the number of protons are both even, then the nucleus has no spin, i.e. NMR inactive;
- 2) if the number of neutrons plus the number of protons is odd, then the nucleus has a half-integer spin (i.e. $1/2$, $3/2$, $5/2$);
- 3) if the number of neutrons and the number of protons are both odd, then the nucleus has an integer spin (i.e. 1, 2, 3).

A nucleus with spin $1/2$ will have 2 possible orientations. In the absence of an external magnetic field, these orientations are of equal energy. If a magnetic field is applied, then the energy levels split; each level is characterized by a magnetic quantum number.

When the nucleus is in a magnetic field, the initial populations of the energy levels are determined by thermodynamics, as described by the Boltzmann distribution. This is very important, and it means that the lower energy level will contain slightly more nuclei than the higher level. It is possible to excite these nuclei into the higher level with electromagnetic radiation. The frequency of radiation needed is determined by the difference in energy between the energy levels. This energy corresponds to radio frequencies and when the spin returns to its base level, energy is emitted at the same frequency. The signal that matches this transfer is measured in many ways and processed in order to yield an NMR spectrum for the nucleus concerned.

The magnetic field at the nucleus is not equal to the applied magnetic field; electrons around the nucleus shield it from the applied field. The difference between the applied magnetic field and the field at the nucleus is termed *nuclear shielding*, which is in turn dependent on the chemical environment. As a result, information about the nucleus' chemical environment can be derived from its resonant frequency (i.e. *chemical shift*). The chemical shift is measured relative to a reference compound and for ^1H NMR, the reference is usually tetramethylsilane, $\text{Si}(\text{CH}_3)_4$.

Moreover, the effective magnetic field is affected by the orientation of neighboring nuclei. This effect is known as *spin-spin coupling* which can cause splitting of the signal for each type of nucleus into two or more lines. The size of the splitting (define as *coupling constant*, J) is independent of the magnetic field and is therefore measured as an absolute frequency (usually in *Hertz*). In addition, the number of splittings indicates the number of chemically bonded nuclei in the vicinity of the observed nucleus.

Mass Spectrometry

Mass spectrometry (MS) is a mainstream chemical analysis technique in the twenty-first century. It has contributed to numerous discoveries in chemistry, physics and biochemistry. Hundreds of research laboratories scattered all over the world use MS every day to investigate fundamental phenomena on the molecular level. MS is also widely used by industry—especially in drug discovery, quality control and food safety protocols. In some cases, mass spectrometers are indispensable and irreplaceable by any other metrological tools.

The uniqueness of MS is due to the fact that it enables direct identification of molecules based on the mass-to-charge ratios as well as fragmentation patterns. The charged species (ions) are produced in the ion source and then transported in gas-phase.

The gas-phase ions subsequently are transferred into the mass analyzer which sorts the ions—in space or time—according to the mass-to-charge ratios (m/z). The separated ions are detected by an ion detector in the space or time domain. Electric signals, produced by the ion detector, are subsequently processed to produce mass spectra.

In fact, mass spectra can be viewed as histograms, which provide information on the number of ions at different m/z values. The detected ions may correspond to the original molecules, their fragments or other species formed during the ionization process. MS enables direct identification of molecules based on the mass-to-charge ratio as well as fragmentation patterns. Thus, it fulfils the role of a qualitative and quantitative analytical technique with high selectivity.

BET Surface Area Analysis

Measuring surface area and porosity of powders is difficult. There are few techniques available and none of those are straightforward. The choice for surface area measurement generally comes down to a technique known as BET. The measurement of porosity and surface area by BET is a relatively simple measurement to carry out; however, the mathematics and physics behind BET is a little more sophisticated.

BET is the initials of the three scientists who developed the mathematics required for the measurement to work. Brunauer, Emmett, and Teller found a way to calculate the specific surface area of a sample including the pore size distribution from gas adsorption (see ref. *J. Am. Chem. Soc.* **1938**, *60*, 309-319, for detailed description of BET theory).

The volume of gas (usually nitrogen) adsorbed to the surface of the particles is measured at the boiling point of nitrogen (77 K). At this temperature the nitrogen gas is below the critical temperature and so condenses on the surface of the particles. It is assumed that the gas condenses onto the surface in a monolayer and so, because we know the size of the gas atom/molecule, the amount of adsorbed (condensed) gas is correlated to the total surface area of the particles including pores at the surface (inaccessible pores are not detected). It is this correlation calculation, volume absorbed to surface area, that BET theory gives us.

Adsorption is the adhesion of atoms, ions, or molecules from a gas, liquid, or dissolved solid to a surface. There are generally accepted to be six adsorption isotherms (**Fig.110**). The BET method is applicable only to adsorption isotherms of type II (disperse, nonporous or macroporous solids) and type IV (mesoporous solids, pore diameter between 2 nm and 50 nm).

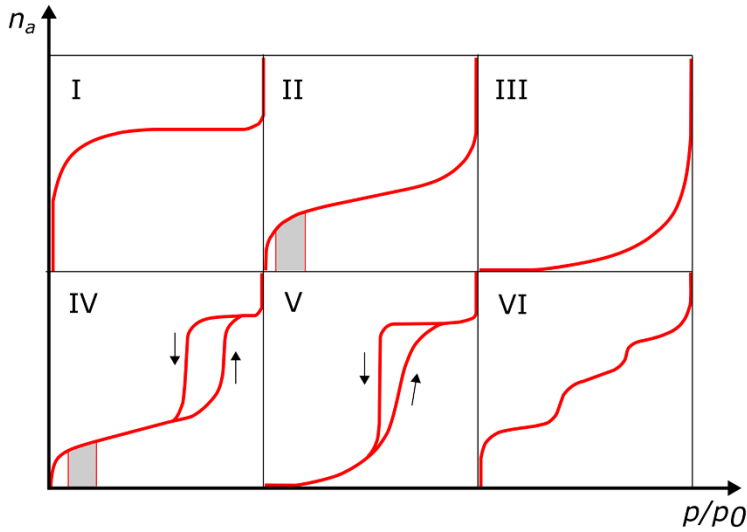


Fig 110 IUPAC classification of adsorption isotherms. The typical BET range is indicated in types II and IV by the shaded areas). n_a =quantity of adsorbed gas, p/p_0 is the relative pressure

As the gas is pumped into the sample tube, the gas covers the external and the accessible internal pore surfaces of a solid. In BET theory, gas covers the sample with a monolayer of adsorbate. The amount of gas used in creating the monolayer can be calculated from the adsorption isotherm using the BET equation (see below). Notably, gas is physically adsorbed by weak bonds at the surface of the solid (*van der Waals forces*) and can be desorbed by a decrease in pressure at the same temperature.

The BET (see below) equation can be used to calculate the surface area of a sample. the measured inputs to this equation are *i*) the equilibrium (p) and the saturation (p_0) pressure of adsorbates at the temperature of adsorption; *ii*) the adsorbed gas quantity (n_a).

$$\frac{1}{n_a[(p_0/p) - 1]} = \frac{c - 1}{n_m c} \left(\frac{p}{p_0}\right) + \frac{1}{n_m c}$$

where p and p_0 are the equilibrium and the saturation pressure of adsorbates at the temperature of adsorption, n_a is the adsorbed gas quantity, n_m is the monolayer adsorbed gas quantity and c is the BET constant.

The BET equation represents an adsorption isotherm and can be plotted as a straight line with $\frac{1}{n_a[(p_0/p)-1]}$ on the y-axis and $\left(\frac{p}{p_0}\right)$ on the x-axis resulting in a *BET plot*. The relationship is assumed to be linear only in the range of $0.05 < \frac{p}{p_0} < 0.35$.

The value of the slope A and the y-intercept I of the BET plot are used to calculate the monolayer adsorbed gas quantity n_m and the BET constant c , according to the following equations:

$$n_m = \frac{1}{A + I}$$

$$c = 1 + \frac{A}{I}$$

Finally, the total surface area S_{total} and the specific surface area S_{BET} are given by the equations:

$$S_{total} = \frac{n_m N s}{V}$$

$$S_{BET} = \frac{S_{total}}{a}$$

where n_m is the monolayer adsorbed gas quantity, N is Avogadro's number, s the adsorption cross section of the adsorbing species, V is the molar volume of the adsorbate gas, and a is the mass of the solid sample or adsorbent.

A BET surface analysis is described by the following main steps.

- 1) *Degas*: prior to the determination of an adsorption isotherm over the BET region the sample must be degassed, while avoiding irreversible changes to the surface. This is generally done either using a vacuum system or by flushing the sample with a gas (e.g. N₂) often at elevated temperature. The temperature used depends on the stability of the sample. A temperature of 110°C is quoted for nitrogen isotherms where the sample is stable to this

temperature. Once cool the sample must be reweighed to take into account any mass loss during degassing.

- 2) *Evacuate*: the sample and reference tubes are evacuated. The reference tube will be treated in the same way as the sample tube throughout the measurement.
- 3) *Volume*: at this stage most BET methodologies will carry out a dead-volume measurement using an inert gas such as He. This result is used to correct the quantity of adsorbate adsorbed. It is important that the sample and reference tube have similar dead volumes. A glass rod or glass beads are often used to reduce dead volume and to give the two tubes similar dead volumes.
- 4) *Evacuate*: the dead-volume gas is then removed by vacuum.
- 5) *Adsorption*: the adsorbate gas is admitted to the two tubes either in doses or as a slow continuous flow. Adsorption of the gas on to the sample occurs, and the pressure in the confined volume continues to fall until the adsorbate and the adsorptive are in equilibrium. The amount of adsorbate at the equilibrium pressure is the difference between the amount of gas admitted and the amount of adsorptive remaining in the gas phase. To calculate this, pressure, temperatures, and dead-volume of the system is required. The reference tube pressure is also used as a reference. This step gives the adsorption isotherm over a selected range of p/p_0 .
- 6) *Desorption*: for the calculation of certain parameters a desorption step is also required, and a vacuum is applied in the reverse of step 5. This will give the “*desorption isotherm*”.

Normally, the determination of specific surface area requires at least 3 measurements of adsorbed gas quantity (n_a) each at different values of p/p_0 .

X-Ray Diffraction

X-ray diffraction is a common technique for the study of crystal structures and atomic spacing. It is based on elastic scattering of x-ray photons by atoms in a periodic lattice. The scattered monochromatic x-rays that are in phase give constructive interference, according to Bragg's law:

$$n\lambda = 2d \sin \theta$$

where n is an integer called the order of reflection, λ is the wavelength of x-rays, d is the characteristic spacing between the crystal planes of a given specimen and θ is the angle between the incident beam and the normal to the reflecting lattice plane.

This law relates the wavelength of electromagnetic radiation to the diffraction angle and the lattice spacing in a crystalline sample. These diffracted X-rays are then detected, processed, and counted. By scanning the sample through a range of 2θ angles, all possible diffraction directions of the lattice should be attained due to the random orientation of the powdered material. Conversion of the diffraction peaks to d-spacings allows identification of the compound because each compound has a set of unique d-spacings. Typically, this is achieved by comparison of d-spacings with standard reference patterns or *Powder Diffraction File* (PDF) database.

This file is released and annually updated by the *International Centre for Diffraction Data* (ICDD). It contains line patterns of more than 60,000 different crystallographic phases. In practice, for any unknown sample, the appearance of three most intense characteristic lines from the standard PDF line pattern is a sufficiently convincing evidence of the existence of a crystalline phase in either a homogeneous substance or even in a multicomponent mixture.

Clear diffraction peaks are only observed when the sample possesses adequate long-range order. Diffraction lines from perfect crystals are very

narrow. For crystallite sizes below 100 nm, line broadening occurs due to incomplete destructive interference in scattering directions where the x-rays are out of phase. The Scherrer equation relates crystal size to line width:

$$\langle L \rangle = \frac{K\lambda}{\beta \cos \theta}$$

where $\langle L \rangle$ is a measure of the dimension of a particle in the direction perpendicular to the reflecting plane, λ is the x-ray wavelength, β is the peak width, θ is the angle between the beam and the normal on the reflection plane, and K is a constant which is often taken as unity.

X-ray line broadening provides a quick, but not always reliable estimate of the particle size.

X-ray diffractometers consist of three basic elements: an X-ray tube, a sample holder, and an X-ray detector. X-rays are generated in a cathode ray tube by heating a filament to produce electrons, accelerating the electrons toward a target by applying a voltage, and bombarding the target material with electrons. When electrons have sufficient energy to dislodge inner shell electrons of the target material, characteristic X-ray spectra are produced. These spectra consist of several components, the most common being K_α and K_β . However, filtering by foils or crystal monochromators is required to produce monochromatic X-rays needed for diffraction.

Copper is the most common target material for single-crystal diffraction, with CuK_α radiation = 1.5418 angstrom. These X-rays are collimated and directed onto the sample. As the sample and detector are rotated, the intensity of the reflected X-rays is recorded. When the geometry of the incident X-rays impinging the sample satisfies Bragg's law, constructive interference occurs and a peak in intensity appears. A detector records and processes this X-ray signal and converts the signal to a count rate, which is then output to a device such as a printer or computer monitor.

The geometry of an X-ray diffractometer is such that the sample rotates in the path of the collimated X-ray beam at an angle θ while the X-ray detector is mounted on an arm to collect the diffracted X-rays and rotates at an angle of 2θ . The instrument used to maintain the angle and rotate the sample is termed a goniometer. For typical powder patterns, data are collected at 2θ from 5° to 70° , angles that are preset in the X-ray scan.

Electron Scanning Microscopy

Scanning electron microscopy (SEM) images of surfaces have great resolution and depth of field, with a three-dimensional quality that offers a visual perspective familiar to most users.

SEM functions by focusing and rastering a relatively high-energy electron beam (typically, 5–100 keV) on a specimen that is under vacuum. Low-energy secondary electrons (1–20 eV) are emitted from each spot where the focused electron beam makes an impact. The intensity of the secondary electron emission is a function of the atomic composition of the sample and the geometry of the features under observation.

The image of the surface is spatially reconstructed on a phosphor screen (or *CCD* detector) from the intensity of the secondary electron emission at each point. Because of the shallow penetration depth of low-energy electrons produced by the primary electron beam, only the secondary electrons generated near the surface can escape and be detected. For this reason, SEM is a surface analysis method.

Nonconductive materials observed in the SEM are typically coated with a thin, electrically grounded layer of metal to minimize negative charge accumulation from the electron beam. However, this metal layer is always thick enough ($>200 \text{ \AA}$) so that the electrons emitted from the sample beneath cannot penetrate.

SEM, in spite of these limitations, is an important corroborative method to use in conjunction with other surface analysis methods. Surface roughness and texture can have a profound influence on data from ESCA, SIMS, and contact angle determinations. Therefore, SEM provides important information in the interpretation of data from these methods.

The primary electron beam also stimulates the emission of X-rays. These X-rays are used to identify elements with the technique called energy-dispersive X-ray analysis (EDXA). The high-energy primary electron beam penetrates deeply into a specimen (a micron or more). The X-rays produced from the interaction of these electrons with atoms deep in the bulk of the specimen can penetrate through the material and be detected. Therefore, EDXA is not a surface analysis method, and the primary use of SEM is to image surface topography.

Curriculum Vitae

Massimiliano Gaeta was born on May 11th, 1989 in Siracusa (Italy).

He attained his BSc in Industrial Chemistry (110/110 cum laude) at University of Catania (Italy) in 2012 with a final work concerning the *controlled self-assembly of porphyrin-calixarenes complexes*.



In the same university he obtained his MSc in Materials Chemistry with full marks (110/110 cum laude) in 2014 discussing an experimental work about *chiral memory in porphyrin heteroaggregates*.

After his master's degree, he won a scholarship grant (11 months) financed by National Research Council (CNR-ISMN) and he moved to University of Messina (Italy) to work in a project related to *membrane functionalization with porphyrins for fuel cell applications*, supervisor Dr. Maria Angela Castriciano.

In 2016, he came back to University of Catania to start his PhD course in Chemical Sciences where he worked in the LSSC lab *-Laboratory of Spectroscopy of Complex Systems-* under the supervision of Prof. Roberto Purrello. He spent part of his PhD course (6 months) at Universidad Autònoma de Madrid (Madrid, Spain), under the supervision of Prof. Félix Zamora, to acquire skills about covalent self-assembly and covalent organic frameworks.

The main scientific interests are focused on supramolecular chemistry with particular attention to porphyrin self-assembly in water and their chiral properties. Other important interests concern the supramolecular functionalization of materials for technological applications (energy, environment, catalysis, new nanomaterials).

During the PhD course he presented the results of his research activity, giving both oral and poster contributions, at several conferences. He won the Best Poster Prize at “Congresso Congiunto delle Sezioni Sicilia e Calabria 2019” organized by Italian Chemical Society (SCI) in Palermo (Italy).

Massimiliano Gaeta is author or co-author of several articles, published in international refereed scientific journals. He is a member of Italian Chemical Society (SCI) as well as Board member of its local section (SCI-Sezione Sicilia). Detailed description of his research activities is reported in the following paragraph “List of publications and proceedings”.

List of Publications and Proceedings

- Publications

1. *Long-Range Chiral Induction by a Fully Non-Covalent Approach in Supramolecular Porphyrin-Calixarene Assemblies*

Gaeta M., Sortino G., Randazzo R., Pisagatti I., Notti A., Fragalà M.E., Parisi M.F., D'Urso A., Purrello R.

Chemical Communications, **2019**, *in submission*

2. *Synthesis and characterization of 5-mono-(4-carboxyphenyl-spermine)10,15,20-Tri-phenyl porphyrin*

Gangemi C.M.A., Randazzo R., **Gaeta M.**, Fortuna C.G., Fragalà M.E., Purrello R., D'Urso A.
Journal of Porphyrins and Phthalocyanines, **2019**, *submitted*

3. *Polyethersulfone mats functionalized with porphyrin for removal of p-NA from aqueous solution*

Gangemi C.M.A., Iudici M., Spitaleri L., Randazzo R., **Gaeta M.**, D'Urso A., Gulino A., Purrello R., Fragalà M.E.

Molecules, **2019**, 24, 3344

4. *Chiral Recognition of L- and D- Amino Acid by Porphyrin Supramolecular Aggregates*

Randazzo R., **Gaeta M.**, Gangemi C.M.A., Fragalà M.E., Purrello R., D'Urso A.

Molecules, **2019**, 24, 84.

DOI: 10.3390/molecules24010084

5. *Chirality enhancement of porphyrin supramolecular assembly driven by template pre-organization effect*

Gaeta M., Raciti D., Randazzo R., Gangemi C.M.A., Raudino A., D'Urso A., Fragalà M.E., Purrello R.

Angewandte Chemie-International Edition, **2018**, 57, pp. 10656-10660.

DOI: 10.1002/anie.201806192

6. *Interaction of spermine derivative porphyrin with DNA*

Gangemi C.M.A., D'Agostino B., Randazzo R., **Gaeta M.**, Fragalà M.E., Purrello R., D'Urso A.

Journal of Porphyrins and Phthalocyanines, **2018**, 22, pp. 581-587.

DOI: 10.1142/S1088424618500645

7. *Porphyrim/sPEEK Membranes with Improved Conductivity and Durability for PEFC Technology*

Carbone A., **Gaeta M.**, Romeo A., Portale G., Pedicini R., Gatto I., Castriciano M.A.
ACS Applied Energy Materials, **2018**, 1, pp. 1664-1673.
DOI: 10.1021/acsaem.8b00126

8. *ZnTPPS demetalation: Role of polyelectrolytes on aggregation after protonation in acid*

Gaeta, M., Randazzo, R., Cristaldi, D.A., D'Urso, A., Purrello, R., Fragalà, M.E.
Journal of Porphyrins and Phthalocyanines, **2017**, 21, pp. 426-430.
DOI: 10.1142/S1088424617500432

9. *Porphyrim stacks as an efficient molecular glue to induce chirality in hetero-component calixarene-porphyrin assemblies*

D'Urso, A., Marino, N., **Gaeta, M.**, Rizzo, M.S., Cristaldi, D.A., Fragalà, M.E., Pappalardo, S., Gattuso, G., Notti, A., Parisi, M.F., Pisagatti, I., Purrello, R.
New Journal of Chemistry, **2017**, 41 (16), pp. 8078-8083.
DOI: 10.1039/c7nj00890b

10. *Spectroscopic characterization of water soluble phosphonato corrole: The effect of H-bounds on the self-assembled species*

Randazzo, R., Savoldelli, A., Cristaldi, D.A., Cunsolo, A., **Gaeta, M.**, Fragalà, M.E., Nardis, S., D'Urso, A., Paolesse, R., Purrello, R.
Journal of Porphyrins and Phthalocyanines, **2016**, 20, pp. 1272-1276.
DOI: 10.1142/S1088424616501066

11. *Chirality of self-assembled achiral porphyrins induced by chiral Zn(II) Schiff-base complexes and maintained after spontaneous dissociation of the templates: A new case of chiral memory*

Gaeta, M., Oliveri, I.P., Fragalà, M.E., Failla, S., D'Urso, A., Di Bella, S., Purrello, R.
Chemical Communications, **2016**, 52, pp. 8518-8521.
DOI: 10.1039/c6cc04018g

12. *Vortexes tune the chirality of graphene oxide and its non-covalent hosts*

Di Mauro, A., Randazzo, R., Spanò, S.F., Compagnini, G., **Gaeta, M.**, D'Urso, L., Paolesse, R., Pomarico, G., Di Natale, C., Villari, V., Micali, N., Fragalà, M.E., D'Urso, A., Purrello, R.
Chemical Communications, **2016**, 52, pp. 13094-13096.
DOI: 10.1039/c6cc05177d

Proceedings – oral communications

1. *Interaction of supramolecular Porphyrin-Calix[4]arene complexes with polyglutamic acid in water*

Società Chimica Italiana - Convegno Nazionale della Divisione di Chimica dei Sistemi Biologici, Siena, 11-13 September 2019, Italy

Massimiliano Gaeta, Rosalba Randazzo, Chiara Maria Antonietta Gangemi, Maria Elena Fragalà, Alessandro D'Urso and Roberto Purrello

2. *Chiral aggregation of ZnTPPS on polylysine: chain length effects*

MEYCS 2018, Rimini, 19-21 November 2018, Italy

Massimiliano Gaeta, Domenica Raciti, Rosalba Randazzo, Chiara Maria Antonietta Gangemi, Antonio Raudino, Alessandro D'Urso, Maria Elena Fragalà, and Roberto Purrello

3. *Chiral porphyrin nanostructures via self-assembly: a fully non-covalent approach*

Società Chimica Italiana – Congresso Congiunto delle Sezioni Sicilia e Calabria, Catania, 9-10 February 2018, Italy

Massimiliano Gaeta, Rosalba Randazzo, Chiara Maria Antonietta Gangemi, Maria Elena Fragalà, Alessandro D'Urso and Roberto Purrello

4. *ZnTPPS demetallation: role of polyelectrolytes on aggregation after protonation in acid*

XXVI Congresso Nazionale della Società Chimica Italiana, Paestum (SA), 10-14 September 2017, Italy

Massimiliano Gaeta, Rosalba Randazzo, Domenico Andrea Cristaldi, Alessandro D'Urso, Roberto Purrello and Maria Elena Fragalà.

5. *Exploiting the spontaneous dissociation of chiral Zn(II) Schiff-base complexes to memorize chirality in self-assembled achiral porphyrins*

Società Chimica Italiana - Workshop delle Sezioni Sicilia e Calabria, Messina, 9-10 February 2017, Italy

Massimiliano Gaeta, Ivan Pietro Oliveri, Maria Elena Fragalà, Salvatore Failla, Alessandro D'Urso, Santo Di Bella, Roberto Purrello

6. *Chirality of self-assembled achiral porphyrins induced by chiral Zn(II) Schiff-base complexes and maintained after spontaneous dissociation of the templates: a new case of chiral memory*

ChirItaly, Catania, 3-5 September 2016, Italy

Massimiliano Gaeta, Ivan Pietro Oliveri, Maria Elena Fragalà, Salvatore Failla, Alessandro D'Urso, Santo Di Bella, Roberto Purrello

Proceedings – posters

1. *Chain length-switching: a supramolecular strategy to drive porphyrin aggregation (Best poster prize award)*

Società Chimica Italiana – Congresso Congiunto delle Sezioni Sicilia e Calabria, Palermo, 1-2 March 2019, Italy

Massimiliano Gaeta, Rosalba Randazzo, Chiara Maria Antonietta Gangemi, Maria Elena Fragalà, Alessandro D'Urso, Roberto Purrello

2. *Polylysine wrapping effect on demetallation-aggregation pathway of ZnTPPS*

MYCS 2017, Milano Marittima (RA), 13-15 November 2017, Italy

Massimiliano Gaeta, Rosalba Randazzo, Chiara Maria Antonietta Gangemi, Alessandro D'Urso, Roberto Purrello, and Maria Elena Fragalà

3. *Chirality of self-assembled achiral porphyrins induced by chiral Zn(II) Schiff-base complexes and maintained after spontaneous dissociation of the templates: a new case of chiral memory*

ChirItaly, Catania, 3-5 September 2016, Italy

Massimiliano Gaeta, Ivan Pietro Oliveri, Maria Elena Fragalà, Salvatore Failla, Alessandro D'Urso, Santo Di Bella, Roberto Purrello

4. *Spectroscopic investigations on TPPS@sPEEK in solution and in polymeric membrane*

XII Congresso Nazionale di Chimica Supramolecolare, Giardini Naxos (ME), 27-30 September 2015, Italy

Massimiliano Gaeta, Alessandra Carbone, Ada Saccà, Rolando Pedicini, Irene Gatto, Andrea Romeo, Luigi Monsù Scolaro, Maria Angela Castriciano

Acknowledgements

First of all, I would like to express my profound gratitude to my supervisor Prof. Roberto Purrello for his motivation and immense knowledge and for giving me the chance of doing my PhD in his research group.

Sincere appreciation to my *boss* Prof. Alessandro D'Urso. His guidance helped me in all the time of research and writing of this thesis. I could not have imagined having a better advisor for my PhD studies.

Very genuine thanks to my best labmate Dr. Rosalba Randazzo for having shared with me stressing laboratory session and the efforts of a research activity. Also the simplest gesture helped me to cheer up my day.

Many thanks also goes to all LSSC group, Prof. Maria Elena Fragalà, Dr. Chiara Gangemi, Dr Alessandra Cunsolo, Dr. Andrea Cristaldi.

I want to acknowledge Prof. Félix Zamora (Universidad Autònoma de Madrid) and his research group for providing me the excellent opportunity to join their research projects as visiting PhD student and for giving me access to the laboratories and research facilities. They also gave me an indispensable training without whom this dissertation could never have written.

I thank my PhD coordinator, Prof. Salvatore Sortino for having guaranteed a high scientific level of the PhD course and Prof. Örjan Hansson (University of Gothenburg, Sweden) for his mid-term thesis review. A special mention goes to Ms. Sabrina Tosto for being always available to make our bureaucratic issues simpler.

Real gratefulness to my thesis reviewers: Prof. Roberto Paolesse (University of Rome Tor Vergata, Italy) and Prof. Luigi Monsù Scolaro (University of Messina, Italy) for improving my dissertation with their comments and suggestions.

I thank all my friends and colleagues with particular mention to XXXII cycle, Viviana Caruso, Marcello Condorelli, Lorena Cucci, Serena Lazzaro, Rossella Migliore, Domenica Raciti.

I want to thank my flatmates, Vittorio Casella, Manuela Di Mauro, Astro and Irene Caruso for having shared with me relaxing and funny moments, but also for the numerous movings.

I am so grateful to my lovely family: my parents and my parents in law for supporting me.

Last but not least, a huge gratitude to my exceptional life partner Alessia Distefano. You encouraged me to start this PhD. You have been showing great patience to hold up my very stressful work periods connected to my crazy world of being *researcher*. Your immense love helps me to overcome all difficulties every day.

page left blank intentionally